



Nagoya Institute of Technology

**Optimization of graphene growth and its
functionalization by chemical vapor deposition**

化学気相合成法でのグラフェン成長の最適化
と機能化

By

PAPON Rémi

A thesis submitted to Department of Frontier Materials of Nagoya Institute of
Technology in partial fulfillment of the requirements for the degree of Doctor of
Philosophy (PhD)

March 2017

“Beautiful is what we see, more beautiful is what we know, most beautiful, by far, is what we don’t”

Nicolas STENO (01/01/1638-25/11/1686)

Danish scientist

Abbreviations

1, 2 and 3D	1, 2, 3 Dimensional
AES	Auger Electron Spectroscopy
AFM	Atomic Force Microscopy
AP	Atmospheric Pressure
Ar	Argon
CNT	Carbon Nano tubes
Cu	Copper
CuNi	Copper Nickel
CVD	Chemical Vapor Deposition
DoE	Design of Experiments
FCC	Face-centered cubic
FE-SEM	Field-Emission Scanning Electron Microscopy
FET	Field Effect Transistor
FWHM	Full Width at Half Maximum
H₂	Dihydrogen
IPA	IsoPropyl Alcohol
ITO	Indium Tin Oxide
LP	Low Pressure
min	minute(s)
Ni	Nickel
N-doped	Nitrogen Doped
PMMA	Poly(methyl)methacrylate
sccm	standard cubic centimeters per minute
SEM	Scanning Electron Microscopy
TEM	Transmission Electron Microscopy
XPS	X-ray Photoelectron Spectroscopy

Acknowledgements

First, I would like to express my heartfelt gratitude and thankfulness to my academic supervisor, **Professor Masaki TANEMURA** (種村眞幸), for accepting me in his laboratory as an exchange student and then as a PhD student. His constant encouragement, support and guidance throughout the last three years were the core of our relationship. Most notably, his research of the unexpected was the source of inspiration for the following work.

I would like to thank **Associate Professor Golap KALITA** for his help during the last three years. His knowledge in material science helped me to explore new subjects in the field and helped me write manuscripts for articles and conferences. He encouraged me to pursue research *ad nauseam*, and pushed me to overcome my limits.

I am very grateful to **Professor Tetsuo SOGA** for his critical comments of the following dissertation, which allowed for corrections and improvements.

I would like to thank my Japanese **Professor Jean-Luc RIGAL** for his Japanese lectures and for introducing me to the Nagoya Institute of Technology during my last year of engineering school, which allowed me to enter the world of research. The help and support of **Mrs Zahia TURPIN**, head of international relations at the École Nationale Supérieure de Chimie de Lille (ENSCL), and of **Professor Christel PIERLOT** were an essential part of my venue to Japan and through my PhD.

A special thanks to my senior **Dr. Subash SHARMA** who introduced me to his work on graphene growth during my exchange with the Nagoya Institute of Technology and for his availability and advice. I want to express my sincerest thanks to my colleagues **Dr. Amutha THANGARAJA**, **Dr. Zurita ZULKIFLI**, **Dr. Yazid YAAKOB**, **Dr. Muhammed Emre AYHAN**, **Dr. Sachin Maruti SHINDE**, **Mr. Mohamad Saufi Bin ROSMI**, **Mr. Riteshukumar Ratnes VISHWAKARMA**, **Mr. Kamal Prasad SHARMA**, **Mrs. Mona Ibrahim Araby IBRAHIM** and **Mr. Rakesh Dayaram MAHYAVANSHI** for their pleasant and valuable help. I would like to commend all of the laboratory members: **Mr. Nikhil KUMAR**, **Mr. Kyoichiro NAKAMURA**, **Mr. Koki TANIYAMA**, **Mr. Yuji WAKAMATSU**, **Mr. Koki WATANABE**, **Mr. Syunji ADACHI**, **Mr. Yukihiro OGAWA**, **Mr. Kento OYAMADA**, **Mr. Kenta TAKEUCHI**, **Mr. Taiki OGAWA**, **Mr. Hiroki OGURA**, **Mr. Kazunari TAKAHASHI** and **Mr. Yoshiya MATSUNO** for their help, assistance and cooperation during my research.

I acknowledge my indebtedness to the Japanese company **NGK** (日本ガイシ) for providing me with a monthly scholarship during my PhD program. Without which it would have been impossible for me to complete this work.

I am very grateful to my parents, **Etienne PAPON** and **Catharine DE WITTE-PAPON**, who encouraged me throughout the PhD process on the other side of the planet, in a country far from

their culture and often their understanding. My brother **Pierre PAPON** deserves a thank you for showing me how dramatically life could be different inside the same family.

I am also very grateful to my friends, **Rémi BOUGUET**, **Anne-Julie VERBEKEN**, **LI Shuang** (李爽) and **Karri FLINKMAN** who were my pillars of support during my long experiments and my struggles encountered along the way. Their humour, understanding and presence helped me more than I could have imagined. I would also like to thank **Cédric BURON**, for his help in the use of LaTeX software and the layout, as well as **Anne-Julie VERBEKEN** and **Angela NGUYEN** for their support and the proofreading in this work.

I would like to express my sincerest gratitude to **OZAWA Toshiya** (小澤敏也) for his endless help in making my life in Japan easier and our long discussions about Japan and its lifestyle, both in English and Japanese.

Finally, I would like to thank people I met in my daily life, whose names escape me, who helped me with some difficulties. Even our minute conversations allowed me to discover important realizations about myself, life and the world.

Abstract

Graphene is one of the hottest materials in nanotechnology due to its particular properties. In order to realize its practical applications, high quality graphene with large domain size to reduce the sheet resistance as well as its band gap engineering should be achieved. In this thesis, these subjects are tackled with graphene synthesized by chemical vapor deposition (CVD) methods on transition metal substrates with several solid precursors.

Chapter 1 describes the motivation and the purpose of the synthesis of graphene along with the structure of graphene and the following properties, the different synthesis methods used in the fabrication of graphene, the transfer techniques, the characterizations and current states of the art about graphene research.

Chapter 2 provides details about the CVD method, particularly its specific parameters and the used precursors and substrates. The mechanisms on Cu, Ni and CuNi substrates are explained, as well as the design of experiments model with its calculations and optimization process.

Chapter 3 explores the effects of 6 parameters inside the CVD system through two designs of experiments. 2^{5-2} matrixes are used for the study of the parameters with interactions. If the growth temperature has an important effect on the size of crystals, the mass of the carbon source reaches an optimum. The growth time and the pyrolysis rate of the carbon source precursor are the main factor where variations could dramatically change the size of crystals.

Chapter 4 discusses the effect of the pyrolysis rate of the carbon source precursor on the synthesis of graphene on Cu substrate. The continuous carbon supply forms well-defined edges while an abrupt stop of this supply let appear unsaturated edges and nanoribbons at the growth front of the crystals. Monolayer crystals are observed at a low pyrolysis rate of 1.5°C/min, confirmed by Raman spectroscopy. A high pyrolysis rate of 3°C/min generates a small adlayer on the top of the flakes. The graphene crystals grow and finally merge together in a continuous film for a long duration.

Chapter 5 focuses on the functionalization of graphene by the incorporation of nitrogen atoms in the graphitic network. The high carbon and nitrogen solubilities in Ni and the controllability of the synthesis on Cu led to the use of CuNi binary alloy where nitrogen-doped bilayer graphene was synthesized. The use of melamine as the sole precursor of both C and N atoms allowed the carbon network to contain 5.8 at % of nitrogen, as confirmed by X-ray photoelectron spectroscopy (XPS).

Chapter 6 investigates the anisotropic etching of graphene by H₂ after the synthesis of graphene flakes and films with camphor. This reverse reaction of graphene growth forms holes in the continuous graphene film, along with symmetric directions of the graphene lattice. With longer duration, nanoribbons with non-uniformed width are created between larger domains. The fabrication of a

Y-shaped nanoribbons is also observed.

Chapter 7 summarizes this work and explores future prospects.

Table of Contents

Abbreviations	v
Acknowledgements	vii
Abstract	ix
Table of Contents	xi
List of Figures	xv
List of Tables	xvii
List of Equations	xix
1 Introduction	1
1.1 Background about graphene	1
1.2 Properties of graphene	2
1.2.1 Electrical and electronical properties	2
1.2.2 Mechanical properties	2
1.2.3 Thermal properties	3
1.2.4 Chemical properties	3
1.2.5 Optical properties	3
1.3 Graphene synthesis methods	3
1.3.1 Exfoliation of graphene by micro mechanical cleavage of HOPG	3
1.3.2 Thermal decomposition of SiC	4
1.3.3 Reduction of graphene oxide	4
1.3.4 Atmospheric pressure chemical vapor deposition	4
1.3.5 Low pressure chemical vapor deposition	4
1.4 Graphene transfer	5
1.4.1 Wet method	6
1.4.2 Bubbling transfer	6
1.4.3 Transfer to mesh	7
1.5 Characterization of graphene	7
1.5.1 Optical microscopy	7
1.5.2 Raman spectroscopy	8
1.5.3 Field emission scanning electron microscopy	8
1.5.4 Transmission electron microscopy	9
1.5.5 X-ray photoelectron spectroscopy	9
1.5.6 Atomic force microscopy	9
1.5.7 Auger electron spectroscopy	9
1.6 Large graphene crystals	10

1.7	Band gap in graphene	10
1.8	Motivation and research objective of the work	11
1.9	Outline of the thesis	12
2	Experimental part	13
2.1	Chemical vapor deposition method	13
2.1.1	Temperature	13
2.1.2	Gases	13
2.2	Precursors	14
2.2.1	Camphor	14
2.2.2	Waste polymer	14
2.2.3	Melamine	15
2.3	Substrates	15
2.3.1	Transition metals	15
2.3.2	Ni	16
2.3.3	Cu	16
2.3.3.1	Principle	16
2.3.3.2	Different pyrolysis rates	18
2.3.4	CuNi alloy	19
2.4	Design of experiments	19
2.4.1	Principle of design of experiments	19
2.4.2	Notation	20
2.4.3	Generators	20
2.4.4	Matrices of effects	21
2.4.5	Matrices of experiments	22
2.4.6	Calculations	23
2.4.7	Optimization	23
3	Optimization of CVD parameters for graphene synthesis through design of experiments	27
3.1	Introduction	27
3.2	Experimental part	27
3.3	Choice of parameters	28
3.4	Results of the designs of experiments	29
3.5	Interactions	31
3.6	Optimization and confirmation	33
3.7	Conclusion	36
4	Controlling single and few-layer graphene crystal growth in a solid carbon source based chemical vapor deposition	37
4.1	Introduction	37
4.2	Experimental part	37
4.3	Results and discussion	38
4.3.1	Low pyrolysis rate	38
4.3.2	High pyrolysis rate	40
4.3.3	Model	41
4.4	Conclusion	42
5	CuNi binary alloy catalyst for growth of nitrogen-substituted graphene by low pressure chemical vapor deposition	43

5.1	Introduction	43
5.2	Experimental part	44
5.3	Results and discussion	44
	5.3.1 Scanning Electron Microscopy and Raman spectroscopy	44
	5.3.2 Optical microscope and Raman mapping	45
	5.3.3 XPS, TEM and AFM analysis	46
5.4	Conclusion	47
6	Formation of graphene nanoribbons and Y-shaped structures by hydrogen induced anisotropic etching	49
6.1	Introduction	49
6.2	Experimental part	49
6.3	Synthesis of graphene flakes	50
6.4	Etching process	50
6.5	Formation of particular structures	52
6.6	Conclusion	54
7	Conclusion	57
7.1	Summary	57
7.2	Future prospects	58
	Bibliography	59
A	List of achievements	79
A.1	Publications in international journals	79
A.2	Conference presentations	80

List of Figures

1.1	APCVD systems with (a) one furnace (b) two furnaces.	5
1.2	LPCVD systems with (a) one furnace (b) two furnaces.	5
1.3	Steps for graphene film transfer along with the wet method.	6
1.4	Steps for graphene film transfer along with the bubbling method.	7
2.1	Camphor molecule	14
2.2	Polyethylene polymer.	15
2.3	Polystyrene polymer.	15
2.4	Melamine molecule.	15
2.5	Adsorption, dehydrogenation and growth of graphene on Ni substrate with different carbon species.	17
2.6	Adsorption, dehydrogenation and growth of graphene on Cu substrate with different carbon species.	18
2.7	Temperature profile of a solid carbon source pyrolysed with a selected pyrolysis rate.	18
3.1	(a) APCVD system, (b) Temperature profiles on growth furnace (blue curve) and carbon source furnace (red curve), the indicated times are just an example.	28
3.2	Interaction X_{124} , where the most favorable parameters are $-X_{12}$ and $+X_{14}$	31
3.3	Interaction X_{134} , where the most favorable parameters are $-X_{13}$ and $+X_{14}$	32
3.4	Interaction X_{223} , where the most favorable parameters are $-X_{22}$ and $-X_{23}$	32
3.5	Interaction X_{235} , where the most favorable parameters are $-X_{23}$ and $X_{25} = 0$	32
3.6	Optimization through contour curves from the mathematical model.	34
3.7	Graphene domains obtained with the best parameters in the two designs of experiments on unelectropolished Cu foil.	35
3.8	Synthesis on an electropolished Cu foil with optimized parameters determined by designs of experiments (a) microscope image of 130 μm crystal (b) Raman spectra of the graphene crystals to study the crystalline nature, layer and defects. Raman spectra at eight randomly selected points show high crystalline structure.	35
4.1	Optical microscope image of single layer graphene crystals on Cu foil (b) Raman spectra taken at four different points of the graphene.	38
4.2	Optical microscope images of graphene crystals with (a) and (b) micrometer length ribbons at the crystals edges (c) saturated growth edge of a graphene crystal.	39
4.3	SEM images of (a) individual hexagonal graphene crystals (b) and (c) growing and merging graphene crystals (c) a merged structure to form a continuous film with a pyrolysis temperature increase rate of 1.5°C/min of the waste plastic and continuous supply of carbon adatoms.	39
4.4	Optical microscope images of round-shaped graphene crystals synthesized on Cu foil with (a) lower (1.5°C/min.) and (b) higher (3°C/min) pyrolysis rates of waste plastic.	40

4.5	(a) SEM image of individual graphene crystals with few-layer morphology (b) Raman spectra of a graphene crystal at two different points (position 1 and 2).	40
4.6	SEM image of (a) individual graphene crystals (b) and (c) growing and merging graphene crystals (d) merged graphene crystal structures in a continuous film with a higher pyrolysis temperature increase rate of 3°C/min for the solid carbon source.	41
4.7	Schematic diagram of the graphene growth process on Cu foil in the developed CVD process.	42
5.1	(a) CuNi alloy for growth of substituted N-doped graphene from melamine (b) Representation of N-doped bilayer graphene (N atoms in red).	43
5.2	SEM images of (a) synthesized graphene on a CuNi substrate and (b) transferred graphene on a SiO ₂ /Si substrate (c) and (d) Raman spectrum at positions 1 and 2, respectively.	44
5.3	(a) Optical microscope image of transferred graphene on a SiO ₂ /Si substrate (b) Raman spectrum of the bilayer graphene in (a) image (c) Raman mapping of the transferred sample (d) Raman spectra bilayer and monolayer graphene at locations 1 and 2, respectively, of the mapping image.	45
5.4	XPS analysis (a) Deconvoluted N1s peak and (b) C1s peak (c) AFM analysis and thickness profile (X and Y axis in nm) (d) TEM image of a bilayer graphene (inset shows the Fast Fourier Transform pattern).	46
6.1	(a and b) Optical microscope images of graphene crystals grown from solid camphor precursor by APCVD process (c) Raman spectrum of the synthesized graphene on Cu foil.	50
6.2	Optical microscope images (a and b) of the etched graphene sample by annealing at 1000°C in an Ar : H ₂ gas mixture (c) etched graphene crystal with formation of a well-defined hexagonal hole (d) Raman spectra of the etched graphene and partially oxidized Cu surface.	51
6.3	(a) FE-SEM image corresponding to back scattered electrons (BSE) providing compositional contrast. SiO ₂ nanoparticles were observed as bright contrasts inside the holes of graphene crystals and etched areas (b) FE-SEM analysis (c) and (d) elementary mapping for carbon and oxygen (e) selective AES analysis of the etched graphene structure on Cu foil.	52
6.4	FE-SEM images of (a) etched graphene sample, showing various structures with pronounced edges. FE-SEM images of (b and c) graphene edges with 60° and 120°, indicating etching along symmetric directions of the graphene lattice.	53
6.5	FE-SEM images of (a) an ordered etched hexagonal hole as well as ribbon like graphene structure (b) formation of Y-shaped graphene ribbons structure with edge etching (three ribbons form 120° to each other) (c and d) nanoribbon structure with the etching process on Cu foil. The nanoribbon is formed with interconnection of two larger graphene domains.	54

List of Tables

2.1	Matrix of effects of Design of Experiments 1.	22
2.2	Matrix of effects of Design of Experiments 2.	22
2.3	Matrix of experiments of Design of Experiments 1.	22
2.4	Matrix of experiments of Design of Experiments 2.	23
2.5	Calculated responses for the optimization of the mathematical model through Equations (2.6) and (2.7).	25
3.1	Parameters of Design of Experiments 1 (DoE1).	29
3.2	Parameters of Design of Experiments 2 (DoE2).	29
3.3	The 16 responses Y_{ka} , with $k = \{1, 2\}$, $a \in [1; 8]$, $a \in \mathbb{N}$, from experiments. . . .	30
3.4	Calculated l_{ki} and l_{kij} coefficients through Equations (2.1) and (2.2), as presented in Section 2.4.6.	30
3.5	Optimized answers calculated from Equations (2.6) and (2.7), as presented in Section 2.4.7, for each growth time and increasing rate.	33


List of Equations

2.1	Calculation of l_{ki}	23
2.2	Calculation of l_{kij}	23
2.3	Example calculation of l_{11}	23
2.4	Mathematical model of Design of Experiments 1	23
2.5	Mathematical model of Design of Experiments 2	24
2.6	Mathematical model of Design of Experiments 1 for optimization	24
2.7	Mathematical model of Design of Experiments 2 for optimization	24

Chapter 1

Introduction

1.1 Background about graphene

The past decade has seen an increase in published articles in the field of graphene, particularly due to its exceptionally promising properties. The high conductivity of graphene associated with its transparency and flexibility makes it the perfect candidate for future electronics in solar cells, watches and flexible screens. Today, the indium tin oxide (ITO) is widely used in touch screens and solar cells can be hindered by the limited available quantity of indium in the Earth's crust, its price, limited recycling [1–4], and the brittle nature of such devices [5–7]. The developments in the fabrication of transistors, diode and electrodes with graphene could pave the way to a new era in electronics [8–15].

Graphite was first used during the Neolithic age, 4th millennium B.C, in southeastern Europe, in a ceramic paint for decorating pottery [16]. A deposit of graphite was discovered in a mine near Borrowdale in Cumbria, England, in the 16th century where local people used it freely for marking sheep [17]. A few decades later, graphite was used as a refractory material for military purposes in the English navy [18]. Until German chemist Abraham Gottlob Werner coined the term *graphite* in 1789 from the ancient greek *graphein* (to write) and *ite* from latin -ita and greek -ites (connected with or belonging to), especially used in the case of gems and stones, graphite was known as black lead or plumbago due to its use in pencils [19, 20]. In 1859, when an abundance of graphite from Ceylon (now known as Sri Lanka) arrived in Britain, Professor Brodie from the University of Oxford attempted to measure the molecular weight of the graphite [21]. The determined C : H : O ratio was 61.04 : 1.85 : 37.11. Since the material was found to disperse in pure or alkaline water, but not in acidic media, Brodie termed the material “graphic acid”. That was the very first sample of graphite oxide prepared experimentally [22]. In 1994, the International Union of Pure and Applied Chemistry (IUPAC), in its Nomenclature and terminology of graphite intercalation compounds, recommended the use of the words *graphene* for a single carbon layer due to the used suffix -ene for fused polycyclic aromatic hydrocarbons, even when the root of the name is of trivial origin (e.g. naphthalene, anthracene, coronene, etc.), and graphite for stacked layers of graphene [23]. A single carbon layer of the graphitic structure can be considered as the final member of this series and so this 2D material can be considered the raw material of allotrope fullerenes (0 dimension), carbon nanotubes (1 dimension) and graphite (3 dimension) [24]. As

such, 2D graphene rolled up in the plane is a carbon nanotube, and multilayer graphene with weak interlayer tunneling is graphite.

Despite the fact that Peierls and Landau showed that 2D materials were thermodynamically unstable and could not exist [25–27], Wallace calculated the band structure of graphite from graphene structural model [28]. In recent years, carbon nanotubes and graphene have become widely discussed topics in various academic fields, especially in physics and material sciences [29, 30] due to its particular properties. These properties come from its unique structural arrangement.

The carbon atoms contain 6 electrons which occupy the shell as follow $(1s)^2(2s)^2(2p)^2$. Due to a small energy difference between the 2s and the 2p states, both are excited together in the presence of an external perturbation, such as another atom, which results in a mixed state formed out of one s-orbital and three p-orbitals, namely p_x , p_y and p_z , being produced. In the case of graphene, one s-orbital is combined with two p-orbitals, namely p_x and p_y , hence the term of sp^2 hybridization [24]. These three hybridized orbitals contribute to a planar assembly with a characteristic angle of 120° between hybrid orbitals forming a covalent bond of 1.42 \AA [31], for a lattice constant of 2.46 \AA [32], which gives a honeycomb structure. The remaining p_z orbital is perpendicular to the sp^2 hybrid orbitals and can bind covalently with neighbouring carbon atoms to form a π bond which creates the Van der Waals forces between graphene layers [33]. Due to the p_z orbital's single electron, the π band is only half-filled [34].

1.2 Properties of graphene

As seen previously, each carbon atom contributes one electron to the π bond and because this electron can occupy either a spin-up or a spin-down state, the valence band is filled while the conduction band is completely empty. The Dirac points, D and D', are defined as the points where the valence and conduction bands meet. They are also, in the case of graphene, the points named K and K' in the first Brillouin zone [11, 31]. The Fermi level, according to the band theory depicts a hypothetical energy level of an electron such that at thermodynamic equilibrium the energy level would have a 50% probability of being occupied at any given time, lies where the valence and the conduction bands meet [35]. These bands meet at the Dirac points and thus graphene is considered a zero-gap semiconductor [11, 28], or semimetal, which leads to high conductivity in graphene.

1.2.1 Electrical and electronic properties

Hence, an electronic mobility of $200,000 \text{ cm}^2\text{V}^{-1}\text{S}^{-1}$ can be reached at room temperature if extrinsic scattering in graphene is eliminated[36–38]. Du et al [39] reported low-temperature mobility approaching $200,000 \text{ cm}^2\text{V}^{-1}\text{S}^{-1}$ for carrier densities below $5 \times 10^9 \text{ cm}^{-2}$ in suspended graphene samples.

1.2.2 Mechanical properties

Graphene is one of the hardest and strongest known materials, it is harder than diamond and stronger (between 10 and 300 times) than steel [40]. Graphene has a very high Young's modulus

1.0 TPa with a high ultimate tensile strength of 130 GPa [40]. This robustness could be used to reinforce other materials [41] or to produce composite materials with graphene [42].

1.2.3 Thermal properties

The experimental thermal conductivity of bulk graphite has been measured as $2000 \text{ Wm}^{-1}\text{K}^{-1}$ [43]. Comparing thermal conductivities of bulk graphite and graphene, Nika et al [44] found that its thermal conductivity depends on flake size and width of the graphene sheet; thermal conductivity ranges from $3000\text{-}5000 \text{ Wm}^{-1}\text{K}^{-1}$, which is consistent with others reports [45]. The upper limit of graphene thermal conductivity has been calculated to be $6600 \text{ Wm}^{-1}\text{K}^{-1}$ [46].

1.2.4 Chemical properties

While graphite is known as one of the most chemically inert materials, graphene, due to its honeycomb structure and its composition of only carbon atoms, possesses an imperfect chemical inertness [47]. Bunch et al [48] found that a monolayer graphene membrane is impermeable to standard gases, including helium. Graphene can also be used as a protective coating that inhibits corrosion of underlying metals [49]. Furthermore, graphene nanoribbons were covalently functionalized by nitrogen species through high-power electrical joule heating in ammonia gas, leading to n-type electronic doping consistent with theory [50].

1.2.5 Optical properties

The impressive optical properties of graphene include its high transmittance of 97.7% of visible light [51]. This property makes graphene a suitable material for fabrication of transparent and flexible electrodes [52], touch screens [8], photodetectors [53] and solar cells [54].

1.3 Graphene synthesis methods

Synthesis of graphene can be summarized in two approaches: bottom-up and top-down. The bottom-up approach focuses on the assembly of graphene layers from atoms and molecules as building blocks, such as epitaxial methods or nanoribbons assemblies. The extraction processes of graphene layers from graphite, such as exfoliation, constitute the top-down approach.

1.3.1 Exfoliation of graphene by micro mechanical cleavage of HOPG

In 2004, Novoselov et al exfoliated graphene from small areas of highly-oriented pyrolytic graphite, where up to $10 \mu\text{m}$ multilayer graphene domains could be prepared [55]. This method allows for the preparation of high quality graphene flakes [56–58]. However, the lack of scalability and control of the size of graphene domains paved the way for other techniques [31].

1.3.2 Thermal decomposition of SiC

The annealing of SiC at 1000°C-1350°C leads to the desorption of Si on the top layers and the epitaxial growth of graphene layers. The kinetics of graphene formation as well as the properties and structure of the synthesized graphene are highly dependent on the gas used (or vacuum), temperature and type of SiC used [31, 59–63]. For example, h-SiC (0001) shows a possible control over the number of layers, which could lead to a uniform coverage of SiC substrate [64, 65]. Various thicknesses were observed on the SiC substrates, particularly due to the high temperatures in which the substrates were exposed [66]. Nanotubes could also be synthesized on the SiC surface [67]. Furthermore, graphene grown on semi-insulating SiC substrate can be used in situ without transferring to other insulating substrate and can be used in applications.

1.3.3 Reduction of graphene oxide

The layers of graphite can be exfoliated through oxidation of graphite [31], in which three major methods, developed by Brodie [21], Staudenmaier [68] and Hummers [69] are mainly used. The obtained graphite oxide is highly hydrophilic and can form stable aqueous colloids to facilitate the assembly of macroscopic structures by simple and cheap solution processes, although it is an inexpensive material [70]. The graphite oxide shows increased interlayer space between the graphene layers which facilitates the exfoliation of graphene oxide sheets [71]. Then, reducing agents can be used to reduce the graphene oxide sheets into graphene sheets through washing processes [22]. The reduction also has a healing effect in terms of the restoration of the graphitic network of sp^2 bonds which increases the electrical conductivity of graphene [72].

1.3.4 Atmospheric pressure chemical vapor deposition

The atmospheric pressure chemical vapor deposition (APCVD) system consists of horizontal quartz tube with an inner diameter of 45 mm and with a length comprised between 70 cm and 1 m, inserted in one or two split furnace(s), as represented Figure 1.1 (a) and (b), respectively. The furnace with a high temperature, around 1000°C, is where the substrate is placed to grow graphene and is called the growth furnace. The second furnace used to evaporate the precursor, is called the carbon source furnace. In the case of only one furnace, only the growth furnace is used and the precursor is melted by convection to evaporate the precursor on a moving support. The cooling process is of prime importance to obtain high quality graphene on a large area [73]. For cooling, the furnaces are opened at the selected pace in order to cool the substrate at the desired speed [74].

The gases play a major role in CVD systems and their quantities and ratios can alter the results dramatically [75–82]. Methane (CH_4), and other gases or liquids [83, 84] can be used. In this work, only Ar and H_2 gases are used for pre-annealing, annealing, growth and cooling.

1.3.5 Low pressure chemical vapor deposition

Another version of the chemical vapor deposition system is the low pressure chemical vapor deposition (LPCVD), Figure 1.2, where a rotary pump or another system is used continuously throughout the experiment to suck the gases up from the system, allowing for control of the internal

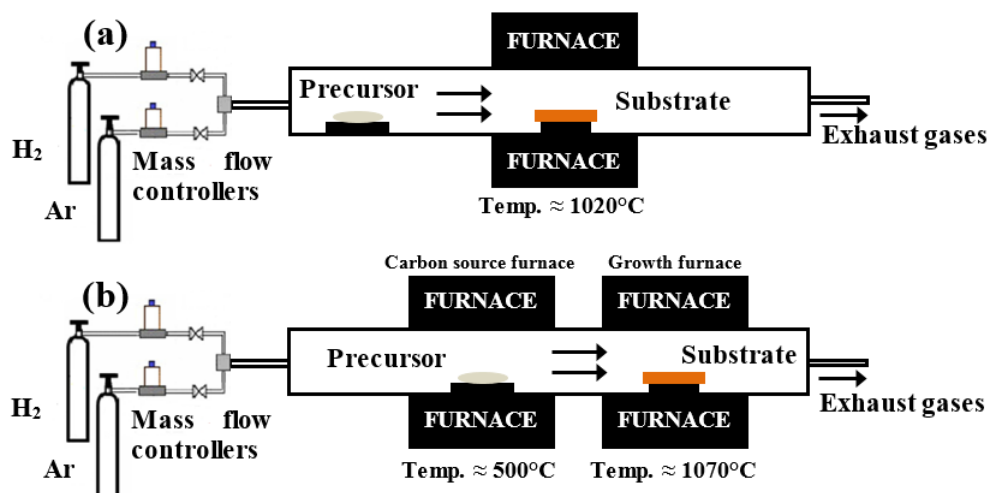


Figure 1.1: APCVD systems with (a) one furnace (b) two furnaces.

pressure until a few Pascals (Pa) [85]. A minimum pressure, called the base pressure, can be reached before the introduction of gases for the experiments [74].

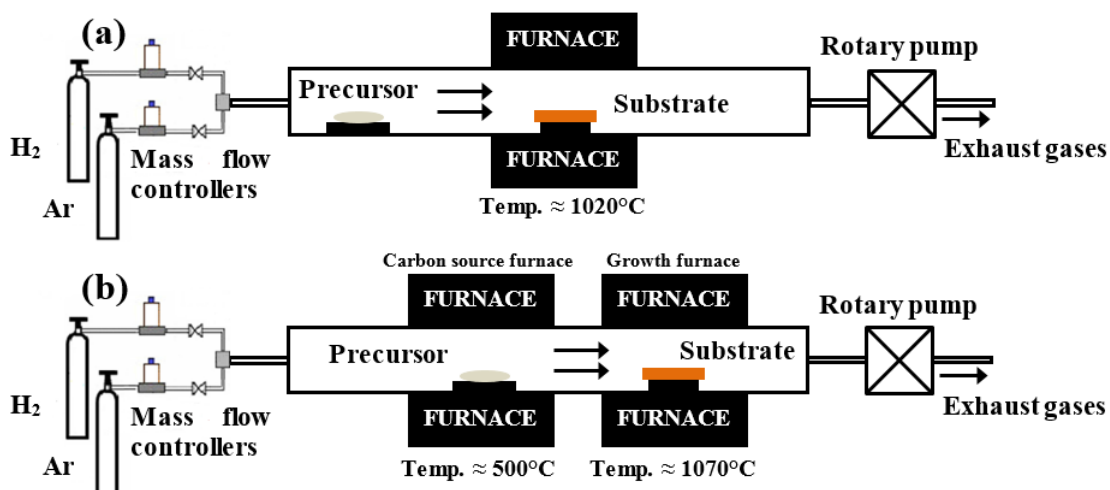


Figure 1.2: LPCVD systems with (a) one furnace (b) two furnaces.

1.4 Graphene transfer

The importance of transfer lies in the ability to remove the graphene from transition metals where it is synthesized to other substrates, for further studies or applications. The transfer of graphene should be handled with great care due to the potential damage caused as a result of the multiple steps involved. The methods presented here involve use of PMMA. However, other techniques exist [86–90].

1.4.1 Wet method

The wet method transfer uses etchants to dissolve the transition metals on which the graphene films are synthesized. The process is described Figure 1.3. A poly(methyl)methacrylate (PMMA) solution, made from a 4.6 g of PMMA in 100 mL of acetone, is spin-coated on the sample for 1 min at 3000 rpm, then dried at 80°C for 10 minutes to strengthen the bonds between the graphene film and the PMMA. For example, a solution of ferric nitrate $\text{Fe}(\text{NO}_3)_3$ (20 g/100 mL) can dissolve copper substrates in a few hours, then the graphene film floating at the surface of the etchant can be dipped in a nitric acid solution and in deionized water 3-4 times to rinse it. The graphene film is then ready to be transferred to another substrate by simple deposition. Subsequently, PMMA is removed first by vapors of acetone, and then the graphene sample on the desired substrate is cleaned in acetone for a few hours. The last step includes a cleaning in isopropyl alcohol (IPA).

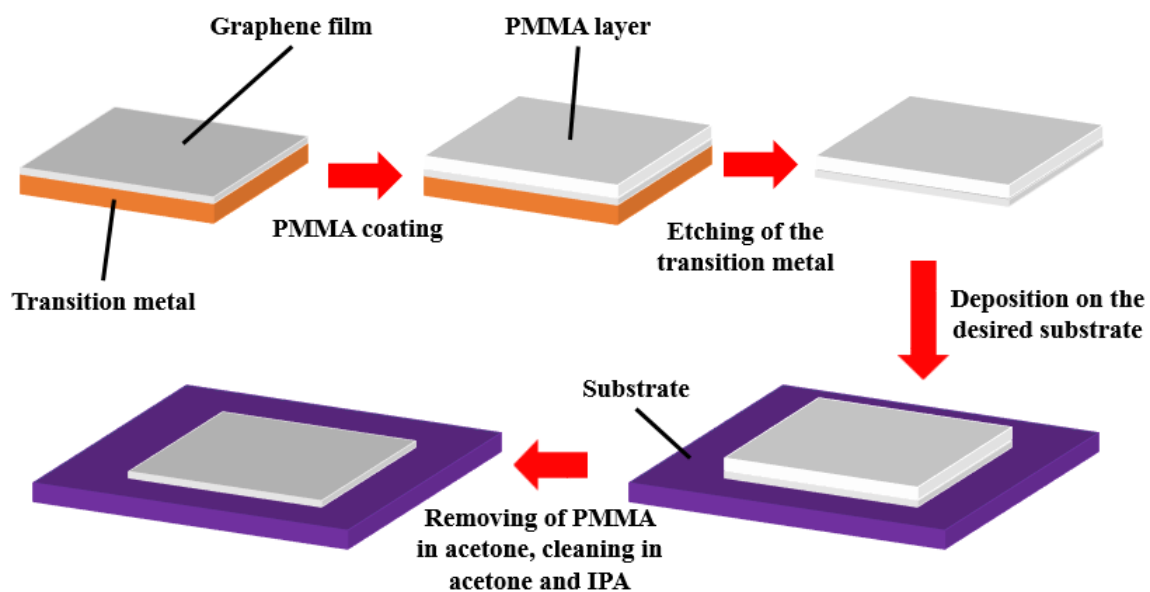


Figure 1.3: Steps for graphene film transfer along with the wet method.

1.4.2 Bubbling transfer

The bubbling transfer method (Figure 1.4) relies on the use of H_2 bubbles created on the transition metals by a difference of potential to separate the graphene film and the metal substrate [91]. The advantage is a smooth separation of the graphene film and the damages made by the etchants can be avoided. A poly(methyl)methacrylate (PMMA) solution, made from a 4.6 g of PMMA in 100 mL of acetone, is spin-coated on the sample for 1 min at 3000 rpm, then dried at 80°C for 10 minutes to strengthen the bonds between the graphene film and the PMMA. The vertical edges can be cut to favour the creation of H_2 bubbles; however, the horizontal edges shouldn't be cut to preserve the integrity of the sample. The PMMA/graphene/substrate sample is inserted in a 1 mol NaOH solution where it is connected to the anode, where the cathode is a plate of platinum (Pt). The potential and current are set to 3 V and 300 mA, respectively, for 2 minutes; the H_2 bubbles created at the surface enable the separation of the PMMA/graphene film and the substrate. The floating film is then cleaned in deionized water a few times before being transferred to the desired substrate by simple deposition. PMMA is removed first by vapors of acetone, then the graphene sample on the desired substrate is cleaned in acetone for a few hours. The last step includes a

cleaning in isopropyl alcohol (IPA).

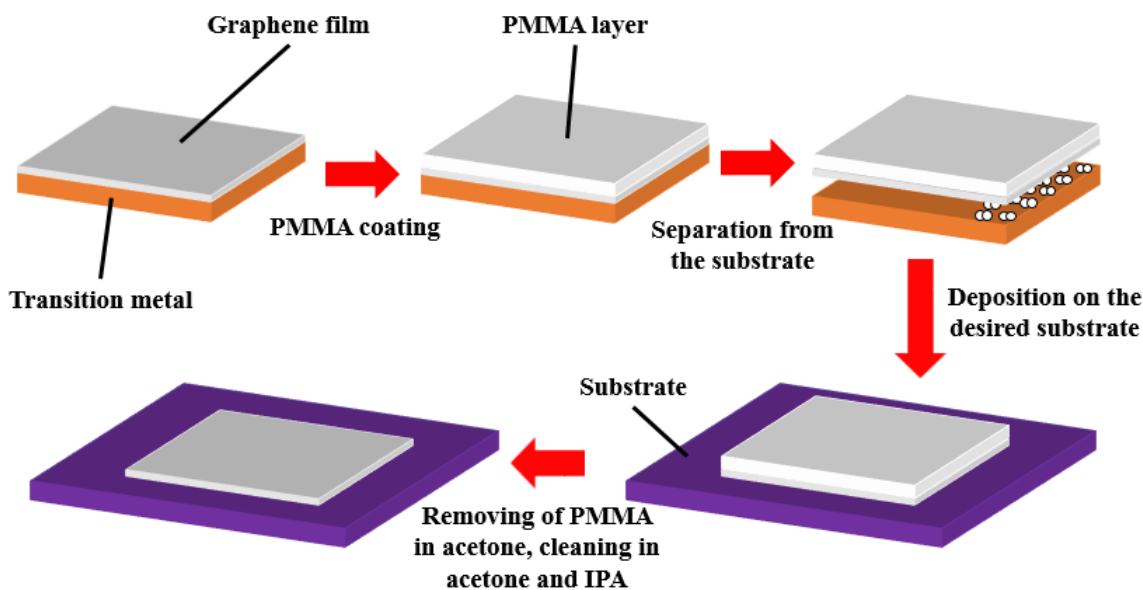


Figure 1.4: Steps for graphene film transfer along with the bubbling method.

1.4.3 Transfer to mesh

Contrary to the two previous methods, the transfer to a mesh substrate is done only for a use in a TEM analysis. A poly(methyl) methacrylate (PMMA) solution, made from a 4.6 g of PMMA in 100 mL of acetone, was coated on the sample in a spin-coater for 1 min at 3000 rpm, then dried at 80°C for 10 minutes to strengthen the bonds between the graphene film and the PMMA. The PMMA/graphene/substrate sample is inserted in a 1 mol NaOH solution where it is connected to the anode, where the cathode is a plate of platinum (Pt). The potential and current are set to 3 V and 300 mA, respectively, for 2 minutes; the H₂ bubbles created at the surface enable the separation of the PMMA/graphene film and the substrate. The floating film is then cleaned in deionized water a few times before being transferred to the mesh. The removal of PMMA is particularly critical since the film should not be broken inside the holes of the mesh. Instead of being cleaned in a hot acetone beaker, hot acetone was slowly dropped on the mesh to remove as much PMMA as possible. The mesh was not cleaned in isopropyl alcohol (IPA) to prevent further damages.

1.5 Characterization of graphene

1.5.1 Optical microscopy

Optical confirmation can be used for the graphene domains synthesized on transition metals, such as copper (Cu), by slight oxidation of the substrate which becomes slightly red. The graphene domains then appear as white to the optical microscope [92]. The exact number of layers is difficult to determine by optical images alone, differences from adjacent layers can easily be resolved. Optical images of this thesis have been obtained with an optical microscope VHX-500 in reflectance mode with a Moticam 2000 2.0 M pixel camera.

1.5.2 Raman spectroscopy

Raman spectroscopy has historically been used to probe structural and electronic characteristics of graphite materials, notably to determine the number of graphene layers by probing the phonon spectrum of graphene [93, 94]. Raman spectroscopy is a relatively easy, non-destructive, non-contacting, and quick measurement method to probe the inelastic scattering of light from a sample surface at room temperature at ambient pressure. The wavelength of the bands is affected by the energy of the laser, and the following wavelengths are given for a laser excitation energy of 532.08 nm, in which a NRS-3300 laser Raman spectrometer was used to take the Raman spectra.

Three important bands are observed in graphitic materials [95–97]. The graphitic peak around 1582 cm^{-1} , called the G band, is caused by in-plane vibration of sp^2 carbon atoms (E_{2g} phonon); the presence of a G band in the Raman spectra indicates that the sample contains sp^2 carbon networks. The signal strength of the D band, located around 1350 cm^{-1} and due to first-order zone boundary phonons, depends strongly on the amount of disorder in the graphitic material [98]; the D band is activated in case of a defect in the network [99, 100]. The third band around 2690 cm^{-1} , called the 2D band as an overtone of the D band, is caused by second-order zone boundary phonons which exhibits a strong frequency dependence on the excitation laser energy and is associated with stacking orders. This 2D band has been used to determine the number of graphene layers [100, 101]. The Full Width at Half-Maximum (FWHM) of 2D bands can be used to determine the number of layers of the considered graphene samples. Monolayer graphene shows a very sharp, symmetric and Lorentzian 2D band. With the increase of number of layers, the 2D band becomes broader, less symmetric and decreases in intensity: the FWHM increases. The FWHM of the 2D band for a monolayer, bilayer and multilayer graphene could typically be 30 cm^{-1} , 50 cm^{-1} and 80 cm^{-1} , respectively.

The intensity ratio I_{2D}/I_G of the 2D and G bands, respectively, is widely used to characterize the number of layers in the synthesized graphene film. A high ratio indicates a monolayer graphene and the lower the ratio, the more layers, with 1 being bilayer graphene and below 1 for multilayer graphene.

1.5.3 Field emission scanning electron microscopy

Field emission scanning electron microscopy (FE-SEM), as its name indicates, is an electron microscopy where a high energy electron beam interacts with the sample; the collected information allows for the reconstruction of the image at the scale of a few nanometers. Different signals are produced, including secondary electrons (SE) and back-scattered electrons (BSE). Back-scattered electrons (BSE) are strongly related to the atomic number and are used to determine the distribution of different chemical elements in the sample. Secondary electrons are emitted from very close to the specimen surface and hence very high-resolution images are produced. Field Emission Scanning electron microscopy (FE-SEM) studies were performed with JEOL JSM-7800F using a lower electron detector (LED), an upper electron detector (UED) and an upper secondary electron detector (USD).

1.5.4 Transmission electron microscopy

Transmission electron microscopy (TEM) is a microscopy technique in which a beam of electrons is transmitted through an ultra-thin specimen, interacting with the specimen as it passes through it (transfer on mesh required, see Section 1.4.3), with the detector collecting the data to form the image. Due to the small Broglie wavelength of the electron, especially compared to phonons, a higher resolution is possible, until the atomic scale. Then, details can be observed with TEM images, such as the number of layers, defects, grain boundaries and twisting of layers. The TEM analysis was performed by JEM-ARM200F with an electron beam energy of 200 kV.

1.5.5 X-ray photoelectron spectroscopy

X-ray Photoelectron Spectroscopy (XPS) is a surface analysis with a typical depth of 5-10 nm, used to determine the quantitative atomic composition, chemical and electronic states of elements in the sample. XPS analyses were performed by the VeraProbe photoelectron spectrometer.

The process works by irradiating a sample with monochromatic X-rays, typically mono-energetic Al $k\alpha$ x-rays, resulting in the emission of photoelectrons from the surface of the sample. An electron energy analyzer is used to measure the kinetic energy of the emitted photoelectrons over a range of electron kinetic energies. The emitted atoms cause peaks to appear in the spectrum from particular characteristic energies of electrons. From the binding energy and intensity of a photoelectron peak, the elemental identity, chemical state, and quantity of a detected element can be determined. For example, nitrogen (N) elements can be detected inside a N-doped graphene, with the known structure of nitrogen atoms and known overall percentage of nitrogen.

1.5.6 Atomic force microscopy

Atomic force microscopy (AFM) is a very-high-resolution type of scanning probe microscopy, designed to measure the topography of a sample, with demonstrated resolution on the order of fractions of a nanometer. AFM analyses were carried out with a JSPM-5200 scanning probe microscope, in tapping mode.

The tip of the cantilever "touches" the sample which gives topographically information about the surface of the sample, in which the repulsion forces push the tip upward. The variations in height of the tip can be measured with a laser beam which reflects on the cantilever; a photodiode can then detect the movement of the beam and consequently the movement of the cantilever and tip. The movement is converted into a change in voltage. Then, an image of the surface can be seen as a reproduction of the variations in voltage. It can be used to see the step edge between graphene and a substrate and thus be able to calculate the thickness of graphene layer(s).

1.5.7 Auger electron spectroscopy

Auger electron spectroscopy (AES) studies were carried out with a JAMP-7800 Auger microscope. The principle is an analysis of the surface with an electron gun. The Auger effect is the so-called phenomenon where an incident electron ejects a core electron and subsequently an electron from

a higher energy level fills the vacancy of the de-excitation with a release of energy. The transition energy could be emitted with a photon or an electron, thus called Auger electron. Due to the kinetic energy of this Auger electron corresponding to the difference between the energy of the initial electronic transition into the vacancy and the ionization energy for the electron shell from which the Auger electron was ejected, which is proper to each atom, it is possible to determine the types of atoms present in the sample.

1.6 Large graphene crystals

Due to the extraordinary properties of graphene for various applications, and its possible widespread use in the future, synthesis of high quality graphene is gaining momentum [8, 36]. Among all techniques presented above, atmospheric and low pressure CVD processes are seen as scalable for large area high quality graphene [102–106]. In the CVD process, the low carbon solubility of Cu substrates have been explored significantly for the growth of monolayer graphene [107–109]. Due to the polycrystalline nature of Cu substrate, the synthesized continuous graphene films are constituted with boundaries between domains [104, 110–115]. The resulting electrical, optical and mechanical properties are then influenced by the crystal size, quality and structure [116]. In order to achieve the predicted theoretical values of physical and electrical properties, it is essential to increase the size of graphene domains, thereby reducing defects and domain boundaries [117, 118]. Synthesis of large size hexagonal graphene crystals have been reported by using the CVD methods [76, 91, 108, 109, 119–124]. In this prospect, many precursors have been used for graphene growth on Cu substrates, such as methane [104, 125, 126], ethylene, liquid and solid precursors [127–130].

The experimental conditions and source materials inside the CVD system can dramatically change the quality of individual graphene crystals and films. For example, the use of a pyrolysis rate of carbon compounds from the solid source can considerably influence graphene growth [120] and it is necessary to control it. Subsequently, the understanding of the graphene growth process in a solid source based CVD process can be significant in controlling growth of single and few-layer graphene.

1.7 Band gap in graphene

The exciting electronic properties of sp^2 hybridized graphene sheets have been the focus of research [56]. The high carrier mobility and conductivity have been used in fabrication of field effect transistors (FET), transparent and flexible devices, as well as sensors [8, 9, 11, 15, 131, 132]. Nevertheless, the lack of band gaps in monolayer graphene hinders its use in the diverse fields of electronics and different approaches have been explored to create a band gap [133, 134]. The applications of a mechanical strain and of a vertical potential in bilayer graphene have been proven effective in creating band gaps [135, 136]. It has been demonstrated that by applying a vertical electric field in bilayer graphene based FET, a band gap of the order of 0.2–0.3 eV can be observed [137].

The modification of graphene structure to open a band gap for nanoelectronics applications have been proposed [138]. The confinement of the charge carriers along one direction in the crystallographic plane can generate a band gap [139, 140]. The development of high quality nanoribbons

is then required to achieve quantum confinement [141, 142]. The width and the crystallographic orientation of the edges determine the properties of the graphene nanoribbons [143]. In nanoribbons with armchair edges, the band gap changes with the width of the ribbons, while zigzag edges have magnetically ordered edge states [144–146]. To obtain graphene nanoribbons and specific nanostructures, diverse top-down and bottom-up processes have been explored, such as synthesis from precise molecules, lithography, unzipping of carbon nanotubes (CNT), plasma etching, metal nanoparticles and induced etching processes [147–159].

Another possibility to open a band gap is to dope graphene sheets by controlling the electron and hole carrier concentrations, and consequently the Fermi-level [160–165]. Kondo et al [166] observed Landau levels of bilayer graphene on N-doped flat graphite surfaces without external magnetic fields. In bilayer N-doped graphene, a $\pi - \pi$ interaction possibly can occur, which affects the interlayer distance and consequently the electronic properties [167].

1.8 Motivation and research objective of the work

Since its rediscovery in 2004, graphene has attracted intense research to attempt to control and modify its exceptional electronics properties. Nevertheless, the presence of defects, impurities, grain boundaries, polycrystalline, structural disorders and wrinkles in graphene sheets have an important effect on its mechanical, thermal, electronic and optical properties. The synthesis of high quality graphene by chemical vapor deposition (CVD), with the desired number of layers and properties, has gain momentum due to its scalability and its possible variations.

The synthesis of graphene on polycrystalline transition metal foils in CVD leads to numerous nucleations on the substrate and to a continuous polycrystalline graphene film where grain boundaries represent a major obstacle for the movements of the electrons. The formation of larger graphene domains has a strong effect on the conductivity of the film. A control of the nucleation is then necessary and can be achieved through the careful control of CVD parameters where small variations could dramatically change the size and shape of the synthesized crystals. The use of design of experiments could explain the influence of some parameters, such as the growth temperature for the formation of graphene. In particular, the pyrolysis rate of the precursor has an effect on the edge termination of the crystals and on the number of layers.

The lack of band gaps in the semimetal graphene hampers its use in electronics where it could replace Si. One bottom-up approach to create a band gap includes the functionalization of graphene layers by doping with foreign atoms, such as N. The inclusion of N atoms in the graphitic network requires control of the precursor as well as of the substrate and its composition, especially due to the different solubilities in the alloy and its mechanisms. Another approach focuses on nanoribbons, where a band gap is observed. Their formation can be observed and controlled to some extent by anisotropic etching of graphene films. The creation of specific structures, such as Y-shaped, could be interesting in future electronics. These electronic properties associated with the bendability of graphene sheets could lead to the use of graphene in wearable and stretchable devices as well as in nanoelectronics and touch screens.

1.9 Outline of the thesis

The following thesis is mostly about the synthesis of graphene inside chemical vapor deposition systems and the formation of specific structures. Synthesis of N-doped graphene is also discussed.

Chapter 1 gives motivation and research objective together with a general introduction about the properties of graphene, the different methods for its synthesis and all techniques used for characterization.

Chapter 2 presents the experimental process in detail with the description of all substrates and precursors used in this thesis.

Chapter 3 details the use of designs of experiments for the optimization of chemical vapor deposition parameters for graphene growth.

Chapter 4 describes the dramatic effect of the pyrolysis rate on the synthesis of monolayer or multilayer graphene.

Chapter 5 discusses the synthesis of nitrogen-doped bilayer graphene on CuNi binary alloy catalyst by low pressure chemical vapor deposition and its importance in opening a band gap.

Chapter 6 reports the formation of graphene nanoribbons and Y-shaped structures by hydrogen induced anisotropic etching.


Chapter 7 summarizes the accomplished research and potential to future prospects.

Chapter 2

Experimental part

2.1 Chemical vapor deposition method

2.1.1 Temperature

 The temperature is one of the main parameters in the CVD system. The heat produced in the CVD system is the main source of energy for the decomposition of carbon precursors and for the activation of the catalyst. Regmi et al [168] demonstrated the effect of temperature on the quality of graphene. Seemingly, this is due to the enhancement of the catalysis of the substrate metal at higher temperatures, which enables quicker carbon construction at the edge of graphene grain. Nevertheless, a temperature too close to the melting point of the substrate will produce excessive defects in the graphene domains [120].

The grain boundaries of the substrate can be seen as defects with an attributed amount of energy. At high temperatures, these grain boundaries migrate to reduce the total amount of energy and the total area of grain boundaries in the sample, which led to the growth of grains [169]. Additionally, annealing at high temperature favors a smoother morphology of the substrate by reducing vacancies, dislocations, stacking faults, and grain boundaries and thus decrease the number of nucleation [170]. Bigger grains and minimization of grain boundaries result in a decrease of nucleations and the growth of uniform graphene.

2.1.2 Gases

Ar is used as a carrier gas. Its constitution of a rare gas makes it inactive with the carbon species involved in the experiments and with the substrate. Nevertheless, possible impurities contained in the gas could have an effect on the growth and shape of graphene crystals [77, 171, 172]. Notably, oxygen has the double effect to reduce the carbon content contained in the Cu foil prior to growth and thus reduces graphene nucleation and accelerate graphene growth [77, 173, 174].

H₂ gas is used to avoid the oxidation and to reduce the metal oxide of the substrate, as well as removing impurities of the substrate while passivating defects and grain boundaries [171]. H₂ has

a dual effect on the synthesis of graphene [81, 175]. One effect is the activation of carbon species such as hydrocarbons and adatoms, which are ready to be chemisorbed for the nucleation, and growth of graphene. The second effect is that H_2 etches the grown graphene [81, 114, 120]. The competition between these two effects lead to the self-limitation of graphene growth on Cu and the etching of graphene can be considered as the reverse reaction of graphene growth. H_2 also plays a role in the sp^3 - sp^2 transition [176].

The ratio of Ar and H_2 can play a major role in the synthesis and in the quality of the synthesized graphene [79, 168, 177–179]. The H_2 pressure influences the number of synthesized graphene layers [180].

2.2 Precursors

For the synthesis of graphene, numerous carbon source precursors have been used, especially gases, such as methane and ethylene, or liquids, such as acetone and methanol [84, 122, 181–188]. However, the C-H bonds have relatively high bond energies in methane (439.3 kJ/mol) and ethylene (464.2 kJ/mol) [189]. Solid precursors have relatively weak C-H bonds, which allows for graphene synthesis at a lower temperature as well as a control of their evaporation [105, 120, 128, 181, 190].

2.2.1 Camphor

Camphor (Figure 2.1) is an abundant, inexpensive, natural hydrocarbon source used in many works for the synthesis of carbon nanotubes (CNT) [191, 192] and graphene [127, 193, 194]. It is a carbon-rich, hydrogen-rich, and oxygen-present molecule with a bi-cyclic cage structure, where its two pentagonal rings are believed to be used as building block for CNT and graphene structures: there is no need to break C-C atomic bonds. The abundance of hydrogen in camphor eliminates the need of additional H_2 gas [192].

The low vapor pressure (27 Pa at 20°C [195]) of camphor allows for decomposition under the heat of the proximate furnace; the control of only the mass of camphor, the vaporization temperature and the flow rate of the carrier gas (such as Ar) could affect its decomposition.

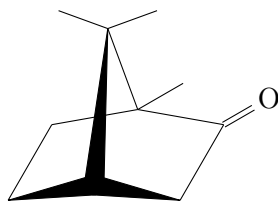


Figure 2.1: Camphor molecule

2.2.2 Waste polymer

The waste polymer precursor is a mixture of polyethylene and polystyrene as explained in [105, 196]. Polyethylene is the simplest polymer chains with ethyl groups as shown Figure 2.2. Polystyrene,

shown Figure 2.3 is polymer with two ethyl group whose one has a phenyl group attached. The relatively weak C-H bond in polystyrene and polyethylene, with bond energies between 292 kJ/mol and 305 kJ/mol [189], which is lower than in other carbon sources such as methane, lead to its use at lower temperatures [120]. This low temperature needed for decomposition as well as its stability due to higher vapor pressure (0.67kPa at 15°C for polystyrene and 8100 kPa at 15°C for polyethylene [195]), makes it a reliable precursor in many experiments [127, 193, 197].

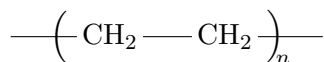


Figure 2.2: Polyethylene polymer.

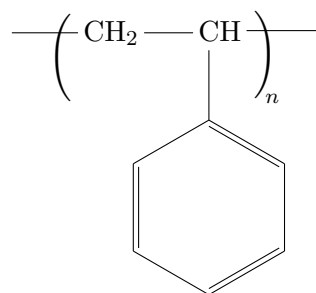


Figure 2.3: Polystyrene polymer.

2.2.3 Melamine

Melamine is an organic chemical compound with a heterocyclic aromatic ring, a 1,3,5-triazine skeleton, and three primary amine groups as shown Figure 2.4. Its sublimating point at 345°C allows for control of its evaporation by controlling the temperature. Its hexagonal ring structure as well as its already incorporated nitrogen atoms makes it a good precursor for the sole source of carbon and nitrogen [198]. It has also been combined with other precursors to obtain the desired graphene [199].

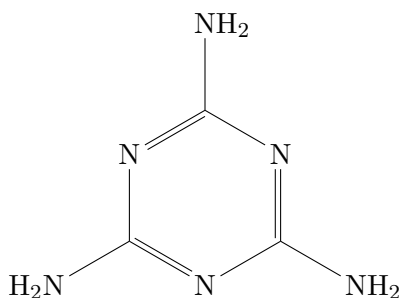


Figure 2.4: Melamine molecule.

2.3 Substrates

2.3.1 Transition metals

Due to the strong C-H bonds in carbon based species (such as in methane, 439.3 kJ mol⁻¹ [189, 200]), the non-catalytic decomposition occurs at very high temperatures (>1200°C). In order to

reduce the temperature of the decomposition of the carbon species and to provide a low energy pathway for hydrocarbon dissociation, transition metal catalysts are used [182, 201]. 3d metals, such as nickel (Ni) and copper (Cu) are favored in comparison to late transition metals for graphene formation [202–204].

As seen previously in Section 1.1, graphene has a honeycomb structure which is a hexagonal lattice. The face-centered cubic (FCC) crystal structures of the metals show different symmetry depending on the surface: (100) is square, (110) is rectangular and (111) is hexagonal. The mismatches of Cu (111) and Ni (111) with graphene lattice are low, 3.7% and 1.2%, respectively [205], which favor the growth of graphene on (111) surfaces [111, 206–210]. The growth of grains is also favored on (111) faces [211], which enable a better morphology on the substrates (see Section 2.1.1)

2.3.2 Ni

The stability and the reactivity of nickel at high temperatures, as well as its high carbon solubility (0.6 weight % at 1326°C [212]), lead to its widespread use. Furthermore, the lattice constant of Ni is 3.52 Å and its first-neighbour distance in the bulk is 2.49 Å [213], which is almost identical to the lattice constant of graphene 2.46 Å [32]. The lattice mismatch is around 1.2%, which facilitates the growth of graphene on Ni surfaces [203].

Presented in Figure 2.5, the decomposition of carbon species starts with H₂ [74, 176] and is followed by the adsorption on the substrate, the dehydrogenation, and after the diffusion not only at the surface [176] but also by the dissolution in the bulk of the metal, due to its high carbon solubility. During the cooling down process, the non-equilibrium process leads to the carbon precipitation on the surface and the formation of graphene [214, 215]. The nucleation sites are then at the grain boundaries, where graphene crystals grow laterally, or at the direct surface precipitation which leads to the development of graphene layers [201, 216, 217]. Hence, it is difficult to obtain uniform graphene films with minimal microstructural defects, such as grain boundaries, due to the multiple nucleations and unpredictable quantity of segregated carbon [218]. However thin Ni film [219] and high cooling rates [88, 220] have been used to achieve monolayer graphene by suppressing the non-equilibrium process.

2.3.3 Cu

2.3.3.1 Principle

Contrary to nickel foils, Cu has a filled 3d shell that results in a low carbon solubility (0.008 weight % at 1084°C [212, 221]) and reduces the tendency for adsorbing hydrocarbons onto the Cu surface. This favors an extensive surface migration of carbon adatoms on the Cu surface and a minimum diffusion into the bulk of Cu [125, 221–223]. The low affinity of C for Cu is also shown in the absence of formation of carbide [215]. The lattice constant of Cu is 3.61 Å and its first-neighbour distance in the bulk is 2.56 Å [213], which is slightly different than the lattice constant of graphene which is 2.46 Å [32]. The lattice mismatch is around 3.7%, larger than of between Ni and graphene (1.2%), which indicates favorable growth on the Cu surfaces [203] but with easier transfer due to the weaker interactions between graphene and Cu substrate [209, 210].

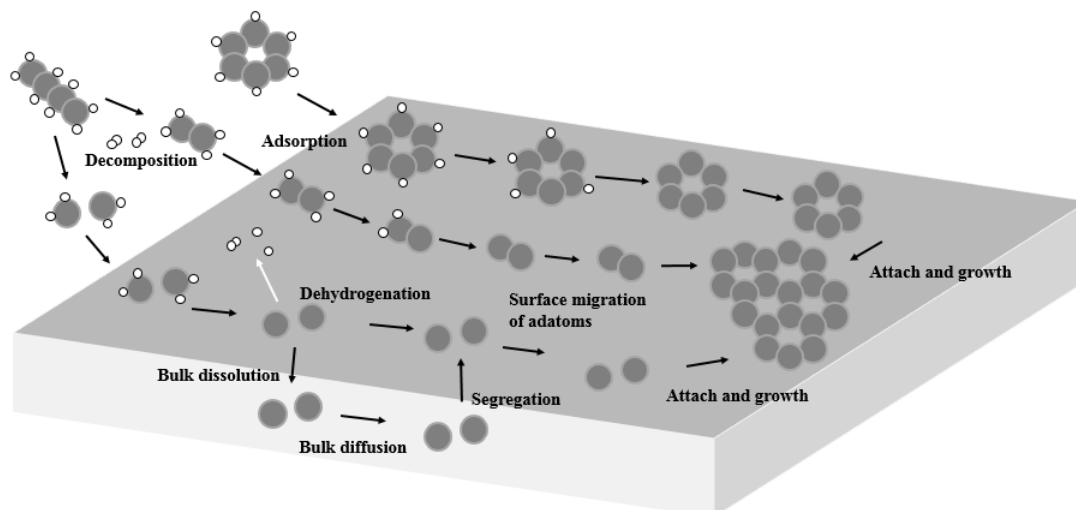


Figure 2.5: Adsorption, dehydrogenation and growth of graphene on Ni substrate with different carbon species.

The carbon source precursor molecules are decomposed with H_2 before being adsorbed by the Cu catalyst where the dehydrogenation of the molecules takes place, followed by the surface migration and the growth [74, 176], as shown Figure 2.6. Wang et al [224] described the different phases of the growth process. The nucleation starts at a carbon adatoms supersaturated point of the substrate [225, 226], typically step-edges or defects due to their stronger bonds [203], where a depletion zone is created at the growth front, with its size depending on the diffusion length of growth species, until all present adatoms are associated in the newly created graphene nucleus. The second phase focuses on the capture of other adatoms, diffused through the diffusion layer and those produced by catalytic decomposition within the diffusion layer, for the growth of the crystal. Growth conditions and substrate grain orientations influence the growth of the graphene crystal [210, 227]. When the diffusion zones of neighbouring crystals start to be close, typically at a distance of $3\ \mu\text{m}$ between the growth fronts, the third phase starts. At the nucleation and at the beginning of the growth cycle, the growth rate is high due to the large amount of adatoms and with the carbon supply. However, this growth rate decreases with the coverage of Cu substrate, during which there is an absence of catalyst to decompose new formed carbon species [214]. The etching, such as with H_2 , is seen as a competitive reaction to the growth and, in the case of fully covered substrate or lack of adatoms [226], this reverse reaction is favored. An equilibrium is then reached between the growth and the etching; this self-limiting process could then allow the formation of monolayer graphene on Cu [125, 201, 228]. However, the formed film is often polycrystalline [110, 112, 223, 229]. The cooling conditions also have a significant effect on the growth of graphene crystals [230, 231].

Due to its low catalytic activity, high temperatures are required for Cu substrates [168]. A higher temperature also has an effect on the quality of graphene [168, 226]. The relatively low melting point of Cu, 1084°C under atmospheric pressure, allows for the synthesis of graphene on melted Cu to suppress the step-edges and defects on the surface and decrease the number of nucleations [113, 179, 232].

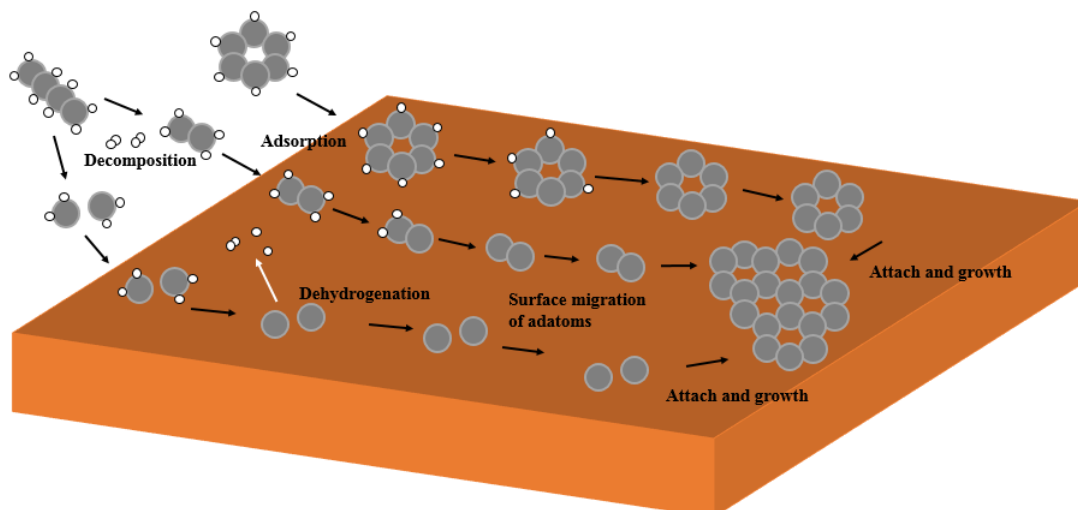


Figure 2.6: Adsorption, dehydrogenation and growth of graphene on Cu substrate with different carbon species.

2.3.3.2 Different pyrolysis rates

In order to grow large graphene crystals, it is necessary to achieve low nucleation density. All possible nucleation centers such as impurities, dislocation, surface irregularities should be reduced to a minimum [102, 227, 233]. Furthermore, due to the dual role of H_2 (see Section 2.1.2), the carbon supply should be controlled to avoid further nucleations and at the same time bring enough adatoms supply to the growing graphene crystals. Wu et al [120] described the mechanism where supersaturation is achieved by rapidly increasing the temperature of the carbon precursor until a nucleation temperature is reached when the polymer decomposes, called nucleation point (Figure 2.7): some activated carbon becomes adatoms and the nucleation occurs on the substrate. These new nucleations formed, the temperature is decreased, typically by 10°C - 15°C , to prevent further nucleations. Then, the growth starts and the temperature is regularly increased by chosen amount of time in order to sustain the need for carbon supply/adatoms; this rate, called pyrolysis rate, can be modified to achieve different graphene structures [196].

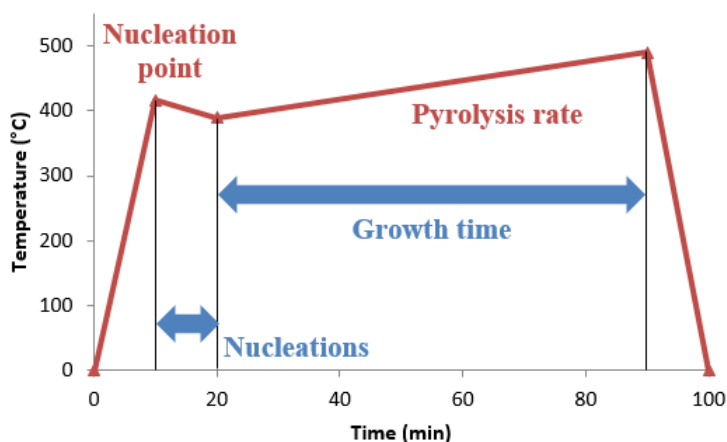


Figure 2.7: Temperature profile of a solid carbon source pyrolysed with a selected pyrolysis rate.

2.3.4 CuNi alloy

The use of Cu foil is wise for the synthesis of monolayer graphene, as shown in Section 2.3.3.1. Ni foil has a mechanism, shown in Section 2.3.2, with precipitation on the metal grains and at the grain boundaries, but the lack of control of this precipitation in Ni and the difficulty to obtain bilayer graphene on Cu lead to the study of alloys for graphene growth. The better solubilities of carbon (C) and nitrogen (N) in Ni than in Cu [205], as well as the better catalytic activity of Ni, makes a CuNi alloy, with a majority of Cu, tunable to obtain the desired number of graphene layers [204, 234, 235].

The CuNi alloy has a FCC structure [236], where impurities such as nitrogen and carbon can occupy octahedral and tetrahedral interstitial sites in this closely packed alloy structure, which increases the overall solubility of carbon and nitrogen [237, 238]. There are greater solubilities of carbon and nitrogen in close-packed structures (FCC and hexagonal), such as in Ni, than in body centered cubic (BCC) structures; nevertheless it is not the case if there is unfavourable atomic size ratio and electronegativity, such as in Cu [239]. Hu et al [240] give nitrogen interstitial formation energies in octahedral and tetrahedral for both Ni and Cu. While in Ni the formation energies in octahedral and tetrahedral are 0.72eV and 1.79eV, respectively, these formation energies are 1.97eV and 2.92eV in Cu, for the same FCC structure. These higher nitrogen interstitial formation energies in Cu than in Ni shows the likely possibility for nitrogen to be more soluble inside Ni than Cu. Furthermore, the solubility of nitrogen in all binary nickel alloys shows an endothermic reaction. Therefore, the nitrogen solubility in these alloys increased with increasing melting temperature [241]. The interstitial formation energy decreases with d-shell filling [240] and so there is a steady decrease in solubility along the period with rising atomic number (where carbon and nitrogen have the same behaviour) for the same structure [239]. The purpose is then to maximize the solubility of nitrogen while keeping the surface reaction of the alloy the same as on pure Cu. The melting point of CuNi alloys varies approximately linearly from 1083°C to 1453°C as the atomic concentration of Ni increases from 0% to 100% [205].

2.4 Design of experiments

2.4.1 Principle of design of experiments

Designs of experiments (DoE) have been used extensively in organic synthesis as well as in other fields [130, 187, 242–244]. The purpose of these designs of experiments is to study the effects of chosen parameters on a selected result with a minimum of experiments and a precision good enough. A large part then relies on the chosen mathematical model. For example, the study of 5 parameters requires $2^5 = 32$ experiments, but due to the aliases between chosen coefficients, it is possible to reduce the number of experiments to $2^3 = 2^{5-2} = 8$ experiments, without greatly reducing the precision of the measurements. It is also possible, in this case, to study the interactions between parameters.

Applied to the synthesis of graphene, the study of different parameters inside the CVD system could lead to a better comprehension of the growth mechanism and to an improvement of graphene domain's size and quality. In Chapter 3, two designs of experiments have been used, with 5 parameters each, as presented in Table 3.1 and Table 3.2, in a 2^{5-2} matrix.

2.4.2 Notation

In this section, as well as in Chapter 3, specific notations will be used for the two designs of experiments. Each parameter will be written as X_{ki} , with $k = \{1, 2\}$, corresponding to design of experiments 1 (DoE1) and design of experiments 2 (DoE2), respectively, and $i = \{1, 2, 3, 4, 5\}$, corresponding to each the parameters in Table 3.1 and Table 3.2. Interactions, between two growth parameters X_{ki} and X_{kj} , are written as X_{kij} . X_{10} and X_{20} are the degrees of freedom of the systems, which are not related to any parameter. l_{ki} and l_{kij} are the corresponding coefficients to the parameters X_{ki} and interactions X_{kij} , respectively. Each parameter has two levels, labelled -1 and +1, with only one value for each level of each parameter. For example, the value of the level -1 of X_{11} is 1050°C while its level +1 is 1070°C (see Table 3.1). By convention, the notation for each level is $-X_{ki}$ and $+X_{ki}$; if a parameter does not have any effect on the response, it is written as $X_{ki} = 0$. The measured response, the size of crystals, is written as Y_{ka} , with $k = \{1, 2\}$, $a \in [1; 8]$, $a \in \mathbb{N}$.

2.4.3 Generators

Generators are the tools used to build a mathematical model by generating the aliases inside the columns. However there are some constraints on the generators, written I_{kz} , $k = \{1, 2\}$, $z = \{1, 2, 3\}$ and how they can be made:

- Generators cannot be the sum of only two parameters (i and j): $I \neq ij$
- Generators cannot be the sum of two interactions. As shown in Section 3.5, interactions such as X_{124} and X_{134} for DoE1, X_{223} and X_{235} for DoE2, $I \neq 23$ for DoE1 and $I \neq 25$ for DoE2.
- Generators cannot be the sum of an interaction and another column. As shown in Section 3.5, interactions such as X_{124} and X_{134} for DoE1, X_{223} and X_{235} for DoE2, $I \neq 24i$ and $I \neq 34i$ for DoE1, $I \neq 23i$ and $I \neq 35i$ for DoE2.

The proposed solutions are as follows:

For DoE1:

- $I_{11} = 1234$
- $I_{12} = 235$
- $I_{13} = 145$

For DoE2:

- $I_{21} = 134$
- $I_{22} = 1235$
- $I_{23} = 245$

The coefficients l_i are the sum of 4 different b_{12345} , b_{ijk1} , b_{ijk} , b_{ij} or b_i coefficients, calculated with the three generators of DoE1 and DoE2 shown above.

For DoE1:

- $l_0 = b_0 + b_{145} + b_{235} + b_{1234}$
- $l_1 = b_1 + b_{45} + b_{234} + b_{1235}$
- $l_2 = b_2 + b_{35} + b_{134} + b_{1245}$
- $l_3 = b_3 + b_{25} + b_{124} + b_{1345}$
- $l_4 = b_4 + b_{15} + b_{123} + b_{2345}$
- $l_5 = b_5 + b_{14} + b_{23} + b_{12345}$
- $l_{24} = b_{24} + b_{13} + b_{125} + b_{345}$
- $l_{34} = b_{34} + b_{12} + b_{135} + b_{245}$

For DoE2:

- $l_0 = b_0 + b_{134} + b_{245} + b_{1235}$
- $l_1 = b_1 + b_{34} + b_{235} + b_{1245}$
- $l_2 = b_2 + b_{45} + b_{135} + b_{1234}$
- $l_3 = b_3 + b_{14} + b_{125} + b_{2345}$
- $l_4 = b_4 + b_{13} + b_{25} + b_{12345}$
- $l_5 = b_5 + b_{24} + b_{123} + b_{1345}$
- $l_{23} = b_{23} + b_{15} + b_{124} + b_{345}$
- $l_{35} = b_{35} + b_{12} + b_{145} + b_{234}$

The coefficients b_{12345} , b_{ijkl} and b_{ijk} are considered to be small before b_{ij} due to the difficulty of having many factors affecting each other. b_{ij} are also considered to be small before b_i , and the chosen interactions (b_{24} and b_{34} for DoE1, b_{23} and b_{35} for DoE2) are supposed to be stronger than other b_{ij} . Furthermore, l_{ki} , $k = \{1, 2\}$, $i = \{1, 2, 3, 4, 5\}$, are the coefficients given by the l_i for DoE1 and DoE2, respectively. The approximation can be written as follows:

For DoE1:

- $l_{10} = l_0 \approx b_0$
- $l_{11} = l_1 \approx b_1$
- $l_{12} = l_2 \approx b_2$
- $l_{13} = l_3 \approx b_3$
- $l_{14} = l_4 \approx b_4$
- $l_{15} = l_5 \approx b_5$
- $l_{124} = l_{24} \approx b_{24}$
- $l_{134} = l_{34} \approx b_{34}$

For DoE2:

- $l_{20} = l_0 \approx b_0$
- $l_{21} = l_1 \approx b_1$
- $l_{22} = l_2 \approx b_2$
- $l_{23} = l_3 \approx b_3$
- $l_{24} = l_4 \approx b_4$
- $l_{25} = l_5 \approx b_5$
- $l_{223} = l_{23} \approx b_{23}$
- $l_{235} = l_{35} \approx b_{35}$

2.4.4 Matrices of effects

Matrices of effects represent the determined levels of the mathematical model inside the designs of experiments. The first four columns are already inserted, the last four are calculated with the generators of each design of experiments. For example, in DoE1, $I_{11} = 1234$, then the fifth column will be calculated by multiplying columns 1, 2 and 3. The results are presented in Tables 2.1 and 2.2.

Experiment	X ₁₀	X ₁₁	X ₁₂	X ₁₃	X ₁₄	X ₁₅	X ₁₂₄	X ₁₃₄
1	1	-1	-1	-1	-1	1	1	1
2	1	1	-1	-1	1	1	-1	-1
3	1	-1	1	-1	1	-1	1	-1
4	1	1	1	-1	-1	-1	-1	1
5	1	-1	-1	1	1	-1	-1	1
6	1	1	-1	1	-1	-1	1	-1
7	1	-1	1	1	-1	1	-1	-1
8	1	1	1	1	1	1	1	1

Table 2.1: Matrix of effects of Design of Experiments 1.

Experiment	X ₂₀	X ₂₁	X ₂₂	X ₂₃	X ₂₄	X ₂₅	X ₂₂₃	X ₂₃₅
1	1	-1	-1	-1	1	-1	1	1
2	1	1	-1	-1	-1	1	1	-1
3	1	-1	1	-1	1	1	-1	-1
4	1	1	1	-1	-1	-1	-1	1
5	1	-1	-1	1	-1	1	-1	1
6	1	1	-1	1	1	-1	-1	-1
7	1	-1	1	1	-1	-1	1	-1
8	1	1	1	1	1	1	1	1

Table 2.2: Matrix of effects of Design of Experiments 2.

2.4.5 Matrices of experiments

Matrices of experiments are used to conduct the experiments with the selected parameters. The levels -1 and +1 in the matrices of effects, Tables 2.1 and 2.2, are replaced by their corresponding parameters from Tables 3.1 and 3.2. Matrices of experiments are presented in Tables 2.3 and 2.4.

Experiment	X ₁₁	X ₁₂	X ₁₃	X ₁₄	X ₁₅
1	1050°C	1.5°C/min	5 mg	67 min	1.5 cm
2	1070°C	1.5°C/min	5 mg	87 min	1.5 cm
3	1050°C	2.0°C/min	5 mg	87 min	1.0 cm
4	1070°C	2.0°C/min	5 mg	67 min	1.0 cm
5	1050°C	1.5°C/min	8 mg	87 min	1.0 cm
6	1070°C	1.5°C/min	8 mg	67 min	1.0 cm
7	1050°C	2.0°C/min	8 mg	67 min	1.5 cm
8	1070°C	2.0°C/min	8 mg	87 min	1.5 cm

Table 2.3: Matrix of experiments of Design of Experiments 1.

Experiment	X ₂₁	X ₂₂	X ₂₃	X ₂₄	X ₂₅
1	30 min	1.2°C/min	90 min	5.0 mg	0.7 cm
2	60 min	1.2°C/min	90 min	3.5 mg	1.0 cm
3	30 min	1.5°C/min	90 min	5.0 mg	1.0 cm
4	60 min	1.5°C/min	90 min	3.5 mg	0.7 cm
5	30 min	1.2°C/min	110 min	3.5 mg	1.0 cm
6	60 min	1.2°C/min	110 min	5.0 mg	0.7 cm
7	30 min	1.5°C/min	110 min	3.5 mg	0.7 cm
8	60 min	1.5°C/min	110 min	5.0 mg	1.0 cm

Table 2.4: Matrix of experiments of Design of Experiments 2.

2.4.6 Calculations

The l_{ki} and l_{kij} coefficients calculated with Equations (2.1) and (2.2), represent the pondered values of the obtained responses Y_{ka} , $k = \{1, 2\}$, $a \in [1; 8]$, $a \in \mathbb{N}$, as shown in Table 3.3. The coefficients C_{ia} and C_{ija} , are from the matrices of effects, Tables 2.1 and 2.2, where i and ij correspond to the column and a to the row, are also required. l_{ki} and l_{kij} coefficients are listed in Table 3.4 and an example is given Equation (2.3) for the coefficient l_{11} .

$$l_{ki} = \frac{1}{8} \times \sum_{a=1}^8 Y_{ka} \times C_{ia} \quad (2.1)$$

$$l_{kij} = \frac{1}{8} \times \sum_{a=1}^8 Y_{ka} \times C_{ija} \quad (2.2)$$

$$l_{11} = \frac{1}{8} \times (30 \times (-1) + 35 \times 1 + 20 \times (-1) + 20 \times 1 + 25 \times (-1) + 30 \times 1 + 15 \times (-1) + 20 \times 1) = 1.875 \quad (2.3)$$

2.4.7 Optimization

The designs of experiments DoE1 and DoE2 have their mathematical models written in Equations (2.4) and (2.5), respectively:

$$Y_1 = l_{10} + l_{11} \times X_{11} + l_{12} \times X_{12} + l_{13} \times X_{13} + l_{14} \times X_{14} + l_{15} \times X_{15} + l_{124} \times X_{12} \times X_{14} + l_{134} \times X_{13} \times X_{14} \quad (2.4)$$

$$Y_2 = l_{20} + l_{21} \times X_{21} + l_{22} \times X_{22} + l_{23} \times X_{23} + l_{24} \times X_{24} + l_{25} \times X_{25} + l_{223} \times X_{22} \times X_{23} + l_{235} \times X_{23} \times X_{25} \quad (2.5)$$

Rewriting the parameters X_{ki} and the interactions X_{kij} in O_{ki} and O_{kij} , respectively, while keeping the l_{ki} and the l_{kij} the same, allows the setting up of the values of some O_{ki} to optimize the response and let only two O_{ki} values vary in order to study their effects on the response. Thus, Equations (2.4) and (2.5) are rewritten as Equations (2.6) and (2.7):

$$Y_1 = l_{10} + l_{11} \times O_{11} + l_{12} \times O_{12} + l_{13} \times O_{13} + l_{14} \times O_{14} + l_{15} \times O_{15} + l_{124} \times O_{12} \times O_{14} + l_{134} \times O_{13} \times O_{14} \quad (2.6)$$

$$Y_2 = l_{20} + l_{21} \times O_{21} + l_{22} \times O_{22} + l_{23} \times O_{23} + l_{24} \times O_{24} + l_{25} \times O_{25} + l_{223} \times O_{22} \times O_{23} + l_{235} \times O_{23} \times O_{25} \quad (2.7)$$

As shown in Table 3.4, the high absolute values of the coefficients of the parameters X_{12} , X_{14} , X_{22} and X_{23} permit these two parameters, growth time and pyrolysis rate, to be used as variables to become O_{12} , O_{14} , O_{22} and O_{23} . Each DoE have 2 levels but their values differ, both in growth time and in pyrolysis rate:

Growth time:

- DoE1 (X_{14}): 67 min and 87 min
- DoE2 (X_{23}): 90 min and 110 min

Pyrolysis rate:

- DoE1 (X_{12}): 1.5°C/min and 2°C/min
- DoE2 (X_{22}): 1.2°C/min and 1.5°C/min

In order to draw a contour curve, it is necessary to have all optimized responses. But some responses cannot be calculated through Equations (2.6) and (2.7) due to the absence of the value of the corresponding levels. For example, in DoE1, it is possible to calculate the optimized responses for 1.5°C/min and 2°C/min with 67 min and 87 min, while the values for 1.2°C/min with 67 min and 87 min are missing and require the proportional calculation of the value of the level 1.2°C/min in DoE1.

In the case of pyrolysis rate of DoE1, O_{12} , the proportionality rule is used with the level -1 of X_{12} , which has the value 1.5°C/min. The value of the level of O_{12} for 1.2°C/min is $(-1) \times 1.2 \div 1.5 = -0.8$. Possible values for O_{12} are then $\{-1, -0.8, 1\}$

In the case of pyrolysis rate of DoE2, O_{22} , the proportionality rule is used with the level 1 of X_{22} , which has the value 1.5°C/min. The value of the level of O_{22} for 2°C/min is $1 \times 2 \div 1.5 = 1.33$. Possible values for O_{22} are then $\{-1, 1, 1.33\}$

Due to the 3 values of O_{12} and O_{22} , combined with the levels of O_{14} and O_{23} , respectively, there is a total of 12 possible responses. These are calculated through Equations (2.6) and (2.7) and are given in Table 2.5. The calculated responses are written Y_{1m} and Y_{2m} , $m = \{b, c, d, e, f, g\}$.

DoE1	$O_{12} = -1$	$O_{12} = -1$	$O_{12} = 1$	$O_{12} = 1$	$O_{12} = -0.8$	$O_{12} = -0.8$
	$O_{14} = -1$	$O_{14} = 1$	$O_{14} = -1$	$O_{14} = 1$	$O_{14} = -1$	$O_{14} = 1$
	$Y_{1b} = 32.5$	$Y_{1c} = 33.75$	$Y_{1d} = 20$	$Y_{1e} = 23.75$	$Y_{1f} = 31.25$	$Y_{1g} = 32.75$
DoE2	$O_{22} = -1$	$O_{22} = -1$	$O_{22} = 1$	$O_{22} = 1$	$O_{22} = 1.33$	$O_{22} = 1.33$
	$O_{23} = -1$	$O_{23} = 1$	$O_{23} = -1$	$O_{23} = 1$	$O_{23} = -1$	$O_{23} = 1$
	$Y_{2b} = 27.5$	$Y_{2c} = 20$	$Y_{2d} = 22.5$	$Y_{2e} = 15$	$Y_{2f} = 21.67$	$Y_{2g} = 14.17$

Table 2.5: Calculated responses for the optimization of the mathematical model through Equations (2.6) and (2.7).

Other O_{ki} values are selected accordingly with results from Table 3.4 and the interactions Figures 3.2 to 3.5, levels that already exist, as optimized parameters:

- Growth temperature: DoE1 shows the important influence of the growth temperature on the size of graphene crystals, while the higher the growth temperature, the bigger the size. Thus, 1070°C was more favorable than 1050°C, which means the optimum level of X_{11} is +1, and so $O_{11} = 1$ is selected.
- Annealing time: In DoE2, a longer annealing time favors bigger graphene crystals. Hence, $O_{21} = 1$ is selected.
- Mass of carbon source: by comparing DoE1 with DoE2, the quantities 8 mg and 3.5 mg are less favorable than 5 mg. 5 mg is then chosen: $O_{13} = -1$, and $O_{24} = 1$.
- Distance from the furnace: in DoE1, the distance from the furnace has a small influence on the results and almost none in DoE2. Thus, in DoE1, $O_{15} = -1$, in DoE2 $O_{25} = 0$.

All the responses used for the optimization are presented in Table 3.5.

Chapter 3

Optimization of CVD parameters for graphene synthesis through design of experiments

3.1 Introduction

Previously, waste plastic polymer has been used for the synthesis of large graphene domains [105], and many studies analyzed the numerous parameters inside the CVD system [74, 245–247]. Their relative importance has not been studied, and to avoid a high amount of experiments, the use of designs of experiments has been proposed. The purpose of this chapter is to establish a clear link between the selected parameters and their effects on the synthesis of large graphene crystals. The independence of these parameters or their conjugation could then be demonstrated, leading to a better comprehension of the growth mechanism of graphene on Cu substrates and its quality.

3.2 Experimental part

An APCVD system with two furnaces was used, as described in Section 1.3.4. Special attention was taken with regards to the distance between the carbon source furnace and the precursor, called D , as shown Figure 3.1 (a). Figure 3.1 (b) shows a schematic representation of the temperature profiles of the growth furnace (blue curve) and carbon source furnace (red curve), with the amount of gases used at each step. The details are explained in Sections 1.3.4 and 2.3.3.2. 100 sccm of H_2 were introduced in the CVD system during the increase of temperature and the annealing, but the mixture of Ar and H_2 (98 sccm : 2.5 sccm) was used for the graphene growth and the cooling down process. The precursor was a waste polymer, as described in Section 2.2.2. Cu foil with a thickness of 20 μm and a purity of 99.98%, from Nilaco Corp., was used as a substrate for graphene synthesis.

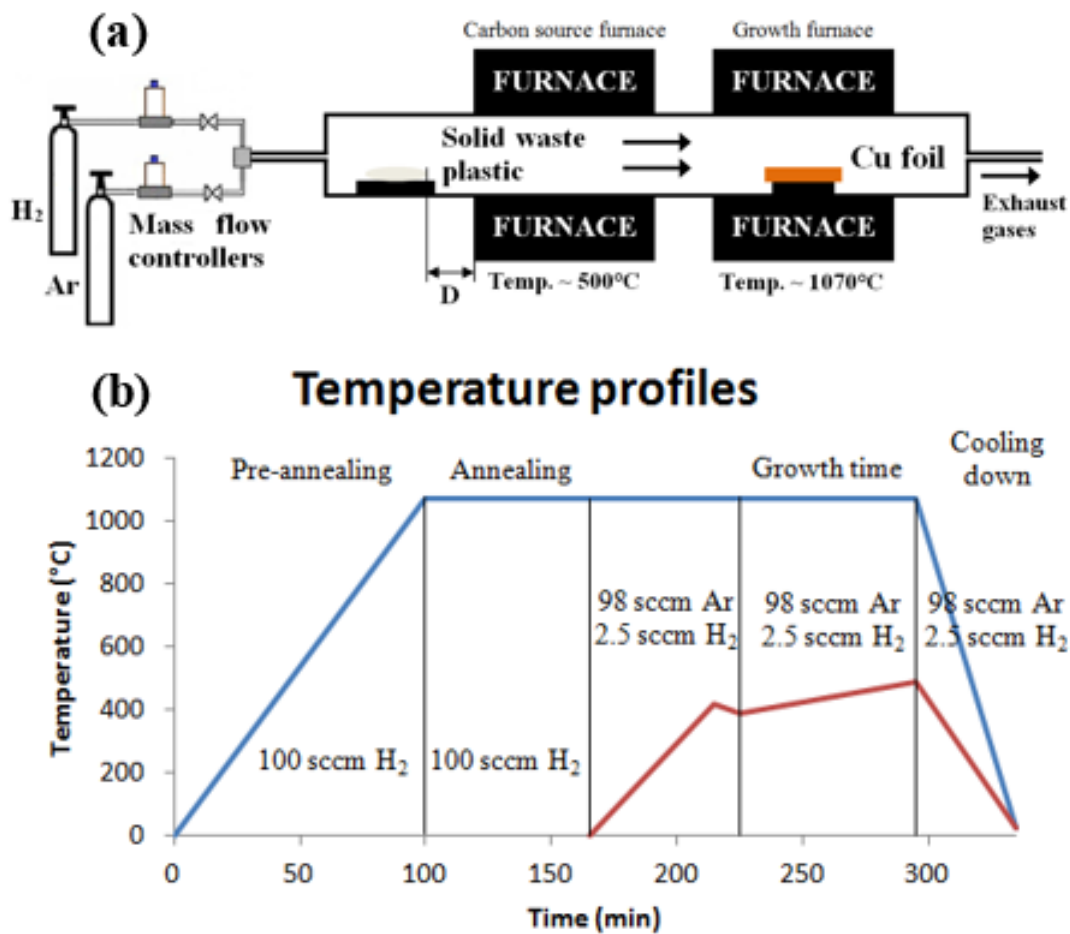


Figure 3.1: (a) APCVD system, (b) Temperature profiles on growth furnace (blue curve) and carbon source furnace (red curve), the indicated times are just an example.

3.3 Choice of parameters

The CVD system has many parameters, most of which were fixed throughout the experiments. Only the parameters judged to be the most important in graphene growth and thus needed to be optimized in the designs of experiments, were selected:

- Growth temperature
- Annealing time
- Mass of carbon source (precursor)
- Pyrolysis rate of the carbon source
- Growth time
- Distance between the carbon source furnace and the carbon source (D)

Due to the melting point of Cu at 1084°C, the growth temperature has an upper limit to avoid liquefaction and excess evaporation of Cu [114]. In the same way, the high partial pressure of Cu

could prevent graphene nucleation and change the reaction conditions. A high temperature still favors graphene growth on Cu substrate and thus the growth temperatures of 1050°C and 1070°C were chosen [227, 235, 248].

Because of the limited study of the growth temperature in the first design of experiments (DoE1), the second design of experiments (DoE2) studies the annealing time as another parameter which is believed to have an effect on the Cu surface, such as on the removal of impurities and the size of Cu grains [82]. The annealing time was kept at 30 min in DoE1, and the growth temperature was kept at 1070° for all experiments in DoE2.

The mass of carbon source, its pyrolysis rate and the distance D are major factors for the control of the combustion of the waste polymer precursor [105, 120, 196]. The growth time is essential to the growth of graphene crystals [105, 249]. These 4 parameters were analyzed with different levels in DoE1 and DoE2 to find the best trend by comparing the influence on the size of graphene crystals.

In order to limit the number of experiments, only 5 parameters (with 4 common ones) were used in each design of experiments, in a 2^{5-2} matrix with two levels. They were arranged as indicated in Tables 3.1 and 3.2.

Growth parameters		Unit	Level -1	Level +1
X ₁₁	Temperature of Cu	°C	1050	1070
X ₁₂	Pyrolysis rate	°C/min	1.5	2
X ₁₃	Mass of carbon source	mg	5	8
X ₁₄	Growth time	min	67	87
X ₁₅	Distance from the furnace (D)	cm	1	1.5

Table 3.1: Parameters of Design of Experiments 1 (DoE1).

Growth parameters		Unit	Level -1	Level +1
X ₂₁	Annealing time	min	30	60
X ₂₂	Pyrolysis rate	°C/min	1.2	1.5
X ₂₃	Growth time	min	90	110
X ₂₄	Mass of carbon source	mg	3.5	5
X ₂₅	Distance from the furnace (D)	cm	0.7	1

Table 3.2: Parameters of Design of Experiments 2 (DoE2).

3.4 Results of the designs of experiments

The 16 experiments were carried out with the selected parameters (see Tables 2.3 and 2.4), and the average sizes of the obtained graphene crystals (in μm), called response, seen by optical microscope after slight oxidation of the Cu surface, are written as Y_{ka} , with $k = \{1, 2\}$, $a \in [1; 8]$, $a \in \mathbb{N}$ and are presented in Table 3.3.

In order to distinguish the most important influences, it is necessary to ponder each coefficient along with the mathematical model. The calculations of the coefficients l_{ki} and l_{kij} are explained in Section 2.4.6, and their values are listed in Table 3.4.

Y_{11}	Y_{12}	Y_{13}	Y_{14}	Y_{15}	Y_{16}	Y_{17}	Y_{18}
30	35	20	20	25	30	15	20
Y_{21}	Y_{22}	Y_{23}	Y_{24}	Y_{25}	Y_{26}	Y_{27}	Y_{28}
25	25	20	20	15	20	10	15

Table 3.3: The 16 responses Y_{ka} , with $k = \{1, 2\}$, $a \in [1; 8]$, $a \in \mathbb{N}$, from experiments.

l_{10}	l_{11}	l_{12}	l_{13}	l_{14}	l_{15}	l_{124}	l_{134}
24.375	1.875	-5.625	-1.875	0.625	0.625	0.625	-0.625
l_{20}	l_{21}	l_{22}	l_{23}	l_{24}	l_{25}	l_{223}	l_{235}
18.75	1.25	-2.5	-3.75	1.25	0	0	0

Table 3.4: Calculated l_{ki} and l_{kij} coefficients through Equations (2.1) and (2.2), as presented in Section 2.4.6.

The coefficients l_{ki} or l_{kij} with the highest absolute values indicate a strong influence of the corresponding parameters on the response, the size of graphene domains. The most influential parameters are then X_{11} , X_{12} , X_{13} , X_{21} , X_{22} , X_{23} and X_{24} and are written in bold characters in Table 3.4. Among these coefficients, there are both negative and positive values. A negative value indicates that the level -1 of the parameter favors the increase of the response Y_{ka} , with $k = \{1, 2\}$, $a \in [1; 8]$, $a \in \mathbb{N}$, while a positive value implies that the level +1 favors the increase of the response. The most favorable parameters are $+X_{11}$, $-X_{12}$, $-X_{13}$, $+X_{21}$, $-X_{22}$, $-X_{23}$ and $+X_{24}$ (see Tables 3.1 and 3.2).

The strong value of the coefficient l_{11} , 1.875, highlights that a higher temperature of 1070°C ($+X_{11}$) eliminates impurities and increases the size of Cu grains, which favor graphene growth [177, 230]. A longer annealing time, 60 min ($+X_{21}$), also favors the creation of a smoother Cu surface. [227].

DoE1 indicates that a lower pyrolysis rate ($-X_{12}$ at 1.5°C/min) is more favorable, and this value corresponds to $+X_{22}$. However, in DoE2, $-X_{22}$ (1.2°C/min) is more favorable from Table 3.4. This means that pyrolysis rate even lower than 1.2°C could be favorable for the growth of large graphene crystals. The coefficients l_{12} and l_{22} are among the highest in these two designs of experiments, showing the importance of pyrolysis rate in the synthesis of large graphene crystals [105, 120].

The values of the levels for the mass of carbon source changed from 5 mg and 8 mg for DoE1, to 3.5 mg and 5 mg for DoE2. In both DoE, the mass of 5 mg is the most favorable ($-X_{13}$ and $+X_{24}$). The optimal quantity is then found, to control the amount of hydrocarbon and adatoms adsorbed to the substrate and attached to graphene crystals in a given time. An excess of adatoms leads to many nucleations and then to smaller crystals while a lack of adatoms does not allow for continued graphene growth [115, 248].

$-X_{23}$ suggests that a shorter growth time of 90 min enhances the size of crystals but the weak value of $+X_{14}$ (0.625) shows the small effect of 87 min, which is better than the 67 min of $-X_{14}$. An equilibrium can then be found around 90 min for the growth time, as the strong l_{23} (-3.75) indicates. This can also be explained chemically, in which crystals need time to grow while the exposure to H_2 , once the crystals have grown, paves the way for the etching of crystals [197, 250], reducing their size.

The coefficients, l_{15} and l_{25} have low values, 0.625 and 0, respectively, meaning that the distance between the carbon source and the carbon source furnace D does not have a strong effect on the size of crystals ($+X_{15}$ and $X_{25} = 0$).

3.5 Interactions

The study of the interactions gives an insight of the dependence between two parameters as well as indication about the relative importance of these parameters on the response. The interactions X_{124} , X_{134} , X_{223} and X_{235} are studied. Interactions are made of an average of the two corresponding experiments. For example, in the interaction X_{124} , in the corner of level -1 of X_{14} and level +1 of X_{12} , the average is made of two values of X_{12} and X_{14} . These two values are taken from the two experiments with the levels -1 for X_{14} and +1 for X_{12} inside the matrix of effects (Table 2.1), which correspond to the experiments 4 and 7 in DoE1 and thus to the responses Y_{14} and Y_{17} , with their values 20 and 15, respectively (Table 3.3).

In the interaction X_{124} (Figure 3.2), it is clear to see the values for level -1 of X_{12} (30 and 30) are higher than for the level +1 of X_{12} (17.5 and 20), then the level -1 of X_{12} favors bigger graphene domains. But, for the level -1 of X_{12} , the levels +1 and -1 of X_{14} show the same value (30), showing the small effect influence of X_{14} ; for the level +1 of X_{12} , the value of the level +1 of X_{14} (20) is slightly higher than the value of the level -1 of X_{14} (17.5), which indicates that the level +1 of X_{14} slightly favors the increase of the size of graphene domains.

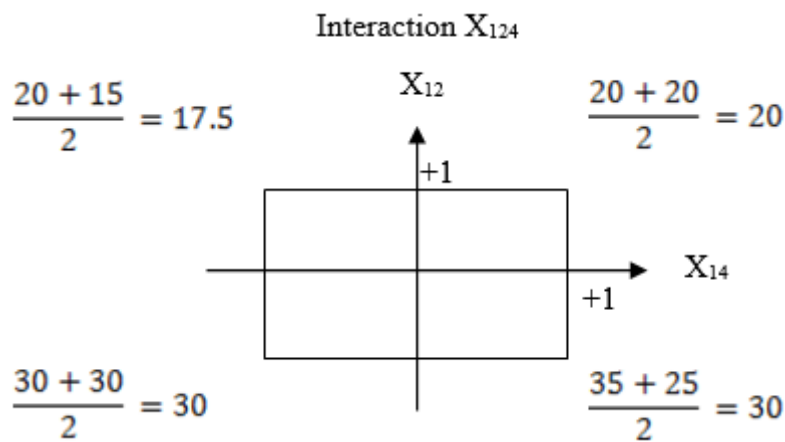


Figure 3.2: Interaction X_{124} , where the most favorable parameters are $-X_{12}$ and $+X_{14}$.

In the interaction X_{134} (Figure 3.3) the level -1 of X_{13} is clearly more favorable, along with a small advantage for the level +1 of X_{14} , confirming the previous analysis of growth parameters with the study of the l_{ki} ($-X_{12}$, $-X_{13}$, $+X_{14}$).

In the interaction X_{223} (Figure 3.4), the level -1 of X_{22} and level -1 of X_{23} are clearly more favorable. In the interaction X_{235} (Figure 3.5), the level -1 of X_{23} is favorable while X_{25} has no influence on the system, confirmed by the low co-efficient $l_{25} = 0$. Thus, the previous analysis of growth parameters with the l_{ki} ($-X_{22}$, $-X_{23}$, $X_{25} = 0$) are confirmed.

The coefficients l_{124} , l_{134} , l_{223} and l_{235} have low values (0.625, -0.625, 0 and 0, respectively). This can be understood as the selection of truly independent parameters, where one parameter

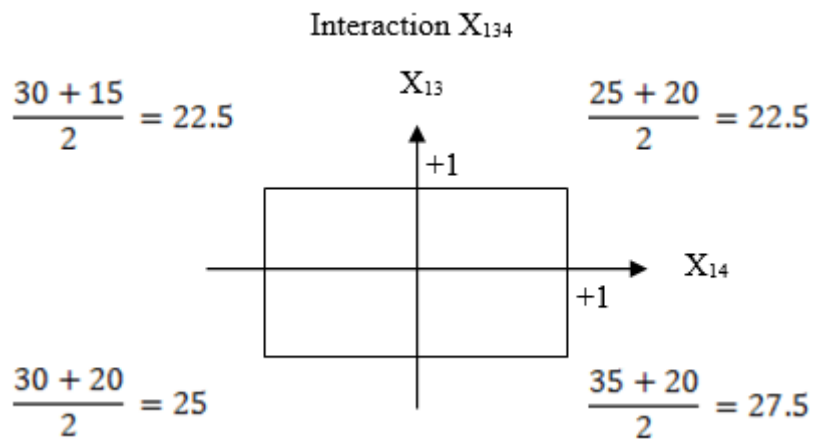


Figure 3.3: Interaction X_{134} , where the most favorable parameters are $-X_{13}$ and $+X_{14}$.

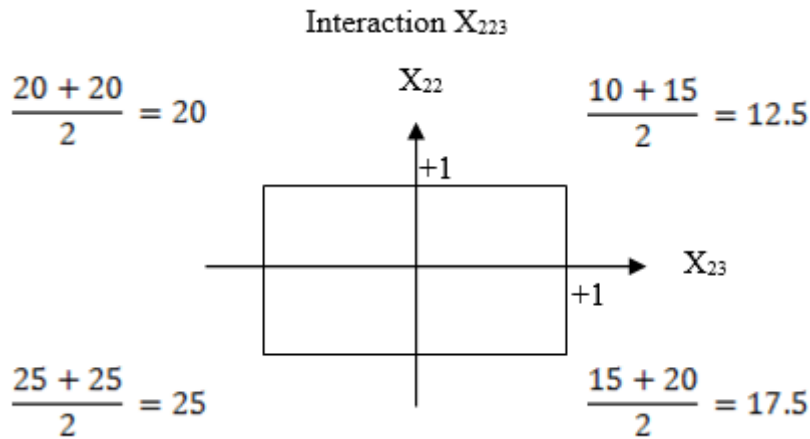


Figure 3.4: Interaction X_{223} , where the most favorable parameters are $-X_{22}$ and $-X_{23}$.

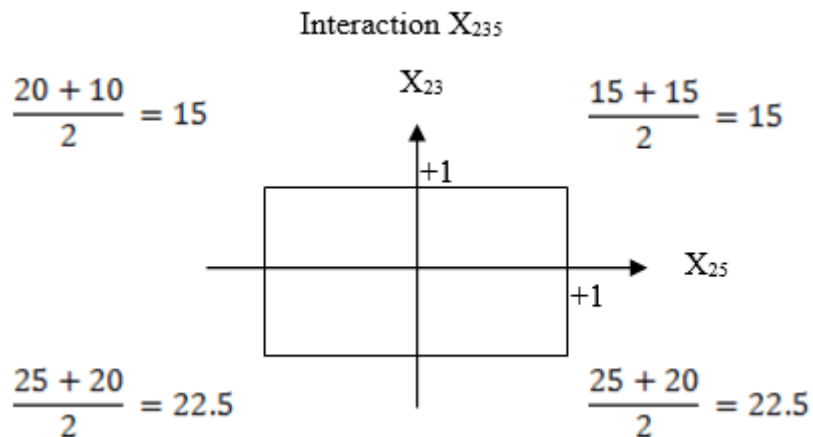


Figure 3.5: Interaction X_{235} , where the most favorable parameters are $-X_{23}$ and $X_{25} = 0$.

does not have an effect on the other; this is further supported by the studied parameters inside the interactions which have strong l_{ki} such as l_{12} . The case of the interaction X_{223} is particularly interesting because l_{22} and l_{23} are very strong but $l_{223} = 0$, which highlights the independence of

Growth time	Increasing rate	Y_{1m} and Y_{2m}
67 min	1.2°C/min	31.25 μm
67 min	1.5°C/min	32.50 μm
67 min	2.0°C/min	20.00 μm
87 min	1.2°C/min	32.75 μm
87 min	1.5°C/min	33.75 μm
87 min	2.0°C/min	23.75 μm
90 min	1.2°C/min	27.50 μm
90 min	1.5°C/min	22.50 μm
90 min	2.0°C/min	21.67 μm
110 min	1.2°C/min	20.00 μm
110 min	1.5°C/min	15.00 μm
110 min	2.0°C/min	14.17 μm

Table 3.5: Optimized answers calculated from Equations (2.6) and (2.7), as presented in Section 2.4.7, for each growth time and increasing rate.

these two parameters (growth time and pyrolysis rate) and their non-conjugated action on the size of graphene crystals.

3.6 Optimization and confirmation

In order to draw optimized contour curves, parameters and interactions of the two designs of experiments are optimized and calculated responses for the optimization of the mathematical model are found. The details of the process is explained in Section 2.4.7. The results are available in Table 2.5.

For a better understanding of the use of these values as coordinates for the representation with contour curves, the calculated values showed in Table 2.5 are associated with the values calculated previously in Table 3.5, arranged by growth times and pyrolysis rate. Through a simulation, the contour curves are calculated and they are shown in Figure 3.6.

In Figure 3.6, the size of domains, with the variations of growth time and pyrolysis rate, are indicated with the blue curve; the value indicates the size in μm . The size of graphene crystals regularly decreases with an increase of growth time above 70 min; it can be linked to the creation of more adatoms with time, which increases the number of nucleations and then make the growth of large crystals impossible. However, with a short growth time, there is not enough adatoms for the growth of the existing graphene crystals.

In the case of at high pyrolysis rate, the size of crystals decreases due to the created hydrocarbons and adatoms on the substrate which form new nucleations or multilayer crystals. For a low pyrolysis rate, the growth rate is too low compared to the etching by the gas mixture, which hinders the growth of large crystals [197, 250, 251].

Thus, optimum points can be observed for both the pyrolysis rate and the growth time in the case of graphene crystals growth, around 1.4°C/min and 72 minutes, respectively. In order to confirm the model, an experiment was made with the optimized parameters found previously and the two

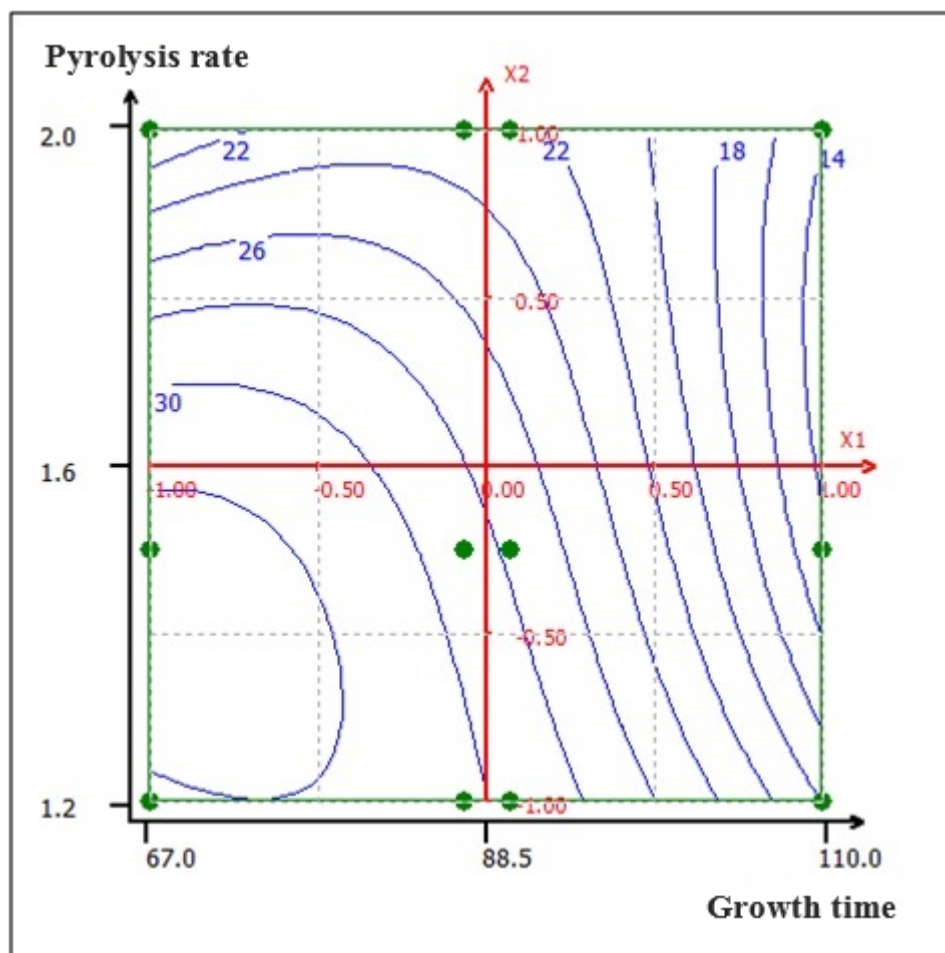


Figure 3.6: Optimization through contour curves from the mathematical model.

optimums. The obtained graphene crystals were around $60\ \mu\text{m}$, as shown in Figure 3.7, which are much larger than the previously synthesized crystals with disarranged parameters.

The improvement of the CVD parameters has a clear effect on the size of graphene crystals. However, other parameters can also affect the size and quality of graphene domains, such as electropolishing and treatment of the Cu surface [252–255]. The Cu foil was electropolished, with the method described in [256], and the optimum parameters determined previously (notably $1.4^\circ\text{C}/\text{min}$ of pyrolysis rate and 72 minutes of growth time) were used. Figure 3.8 (a) shows the obtained crystals, with a maximum size of $130\ \mu\text{m}$. The Raman spectra Figure 3.8 (b) were taken at eight different points of the crystal. The graphitic G band and second order 2D band are observed at $1570\ \text{cm}^{-1}$ and $2690\ \text{cm}^{-1}$, respectively. The higher intensity of the 2D band than that of G band indicates the presence of single layer graphene; the FWHM are $20.2\ \text{cm}^{-1}$ and $38.7\ \text{cm}^{-1}$, values which are consistent with the presence of monolayer graphene. A very small defect induced D band confirms the high quality of the graphene. This indicates that the morphology of the Cu foil induces some effects on the nucleation and growth of graphene [78, 111, 177, 229, 233, 257].

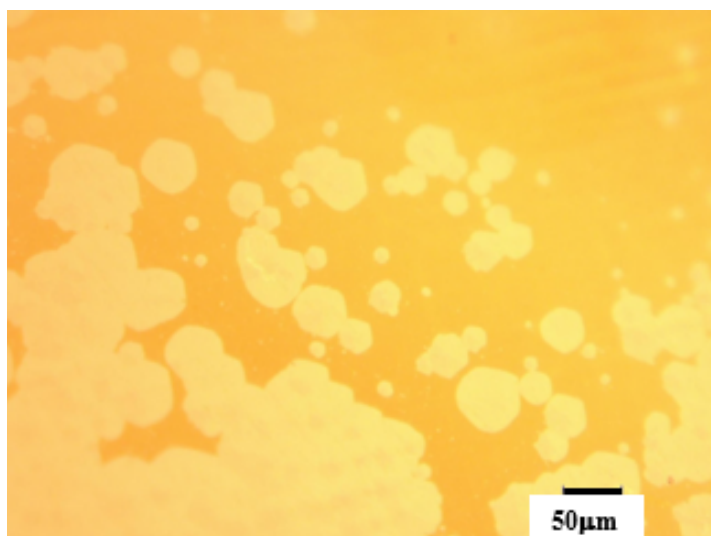


Figure 3.7: Graphene domains obtained with the best parameters in the two designs of experiments on unelectropolished Cu foil.

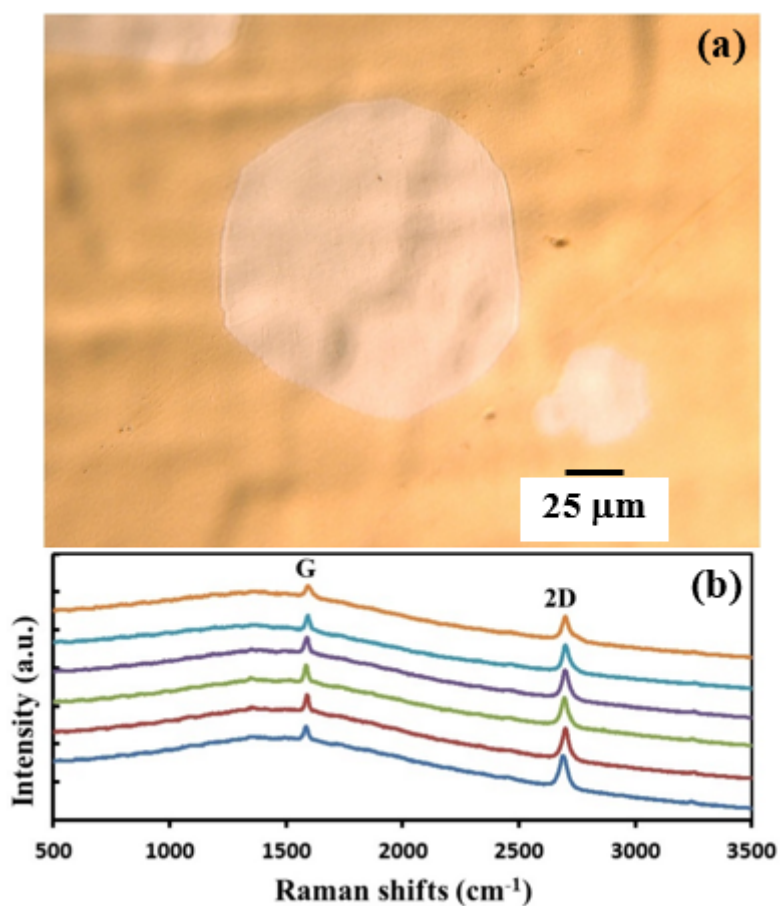


Figure 3.8: Synthesis on an electropolished Cu foil with optimized parameters determined by designs of experiments (a) microscope image of 130 μm crystal (b) Raman spectra of the graphene crystals to study the crystalline nature, layer and defects. Raman spectra at eight randomly selected points show high crystalline structure.

3.7 Conclusion

The use of the two designs of experiments allowed for verification of the independence of the parameters and their specific effects on the synthesis of large graphene crystals. The growth temperature has a major effect on the size of crystals, despite its own limitation due to the closeness of the melting point of Cu. Indications were found about the growth time and the mass of carbon source to improve the size. The observation of the breakthrough in the domain size through the optimization of all parameters implies a possible improvement in the CVD conditions for the synthesis of large high quality graphene crystals. Most notably, the growth time and the pyrolysis rate appear as the main factors for the growth of graphene domains, where the manipulation of only these two parameters could dramatically change the size. Using a smoother surface, to decrease the number of nucleation sites, by the electropolishing of the Cu surface shows another way of improvement.

Chapter 4

Controlling single and few-layer graphene crystal growth in a solid carbon source based chemical vapor deposition

4.1 Introduction

As seen in Chapter 3, CVD technique can be tuned to increase the size, the quality and the structure of graphene crystals. These characteristics of graphene influence its electronic properties [107, 116], especially in bilayer graphene [134, 136]. The synthesis of AB-stacked, twisted bilayer single crystal graphene and large crystals on Cu foil have been realized in CVD systems [91, 107–109, 120, 126, 258]. Instead of a gas precursor, the use of a solid precursor has been explored previously for the synthesis of high quality graphene, where the low energy of C-H bonds allowed for synthesis at lower temperatures and separation between precursor and substrate's furnaces [105, 127, 128, 193]. However, the pyrolysis rate of the carbon source compounds considerably influence the graphene growth, not only in size but also in shape and layers [120, 259]. Notably, the exploration in this chapter of a high pyrolysis rate, which could enhance the carbon supply, leads to a better understanding of the mechanism of graphene growth and the structural properties of the synthesized graphene layers. Thus, the control of this pyrolysis rate of the solid source could then be a major tool in the growth of single and few-layer graphene.

4.2 Experimental part

The APCVD process is explained in Section 1.3.4 with a waste polymer precursor, as described in Section 2.2.2. 3 mg of waste polymer are used for each experiment, as the sole carbon source. Cu foil with a thickness of 20 μm and a purity of 99.98%, from Nilaco Corp., was used as a substrate for graphene synthesis. After the pre-annealing process from room temperature to 1020°C, the Cu

substrate was annealed for 30 min in 100 sccm of H_2 at $1020^\circ C$. Then, the gases were changed to a mixture of 98 sccm of Ar and 2.5 sccm of H_2 . While the waste polymer was slowly pyrolyzed, at the chosen rates of $1^\circ C/min$ and $3^\circ C/min$ up to $480^\circ C$, as explained in Section 2.3.3.2. The synthesized graphene flakes were then observed and analyzed.

4.3 Results and discussion

4.3.1 Low pyrolysis rate

The synthesis with a pyrolysis rate of $1.5^\circ C/min$ is represented in Figure 4.1 (a). The defined edges of the crystals show a uniform growth, without structural or morphological defects on the microscope. Figure 4.1 (b) shows Raman spectra at four different points of the sample. With the intensity of 2D band being higher than the intensity of the D band, Raman spectra confirms the obtainment of monolayer graphene at many points in the sample. Furthermore, the small D band highlights the high quality of the synthesized graphene flakes.

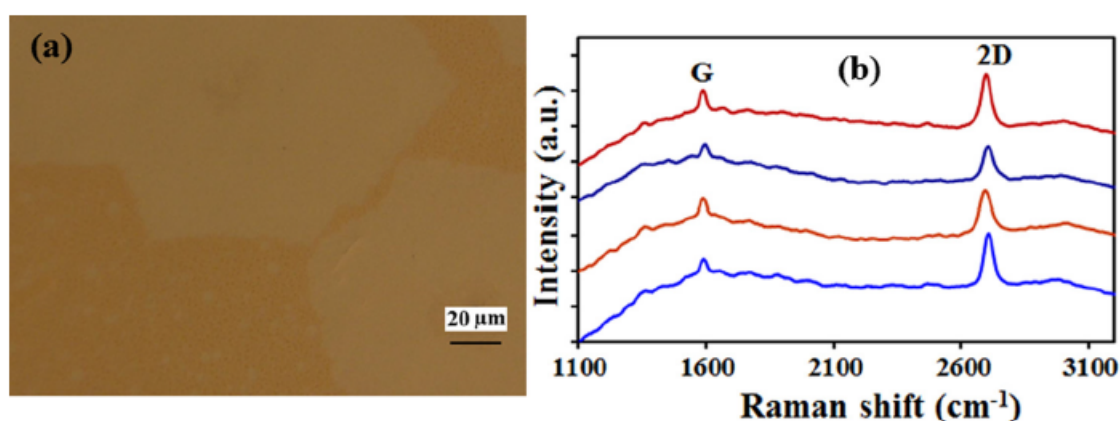


Figure 4.1: Optical microscope image of single layer graphene crystals on Cu foil (a) Raman spectra taken at four different points of the graphene.

The structure of the crystal can be affected by the growth conditions of the CVD process or by the conditions of deposition of the precursor. Figure 4.2 (a) and Figure 4.2 (b) show unsaturated growth edges when the supply of carbon adatoms from the waste polymer precursor is stopped abruptly. Micrometer length ribbons at the edges of crystals are observed, showing the growth front of the crystals. By comparison, if the precursor injection in the growth zone continues, graphene domains show a saturated growth edge, without any ribbons, as shown Figure 4.2 (c).

With a low pyrolysis rate of $1.5^\circ C/min$ and a continuous supply of carbon adatoms, it is possible to grow graphene domains until $100\ \mu m$ (Figure 4.3 (a)). If the growth duration is increased, the crystals grow and merge (Figure 4.3 (b) and (c)) and the merging of graphene crystals in a continuous film is observed, as shown in Figure 4.3 (d) [110]. The pyrolysis rate and the duration of this pyrolysis can then be significant for the synthesis of uniform continuous films with the hexagonal crystals as ideal building blocks.

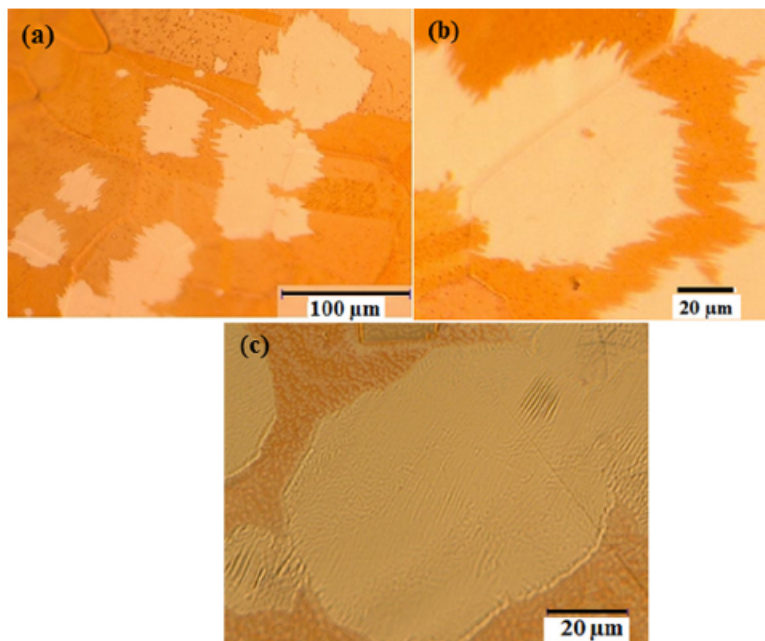


Figure 4.2: Optical microscope images of graphene crystals with (a) and (b) micrometer length ribbons at the crystals edges (c) saturated growth edge of a graphene crystal.

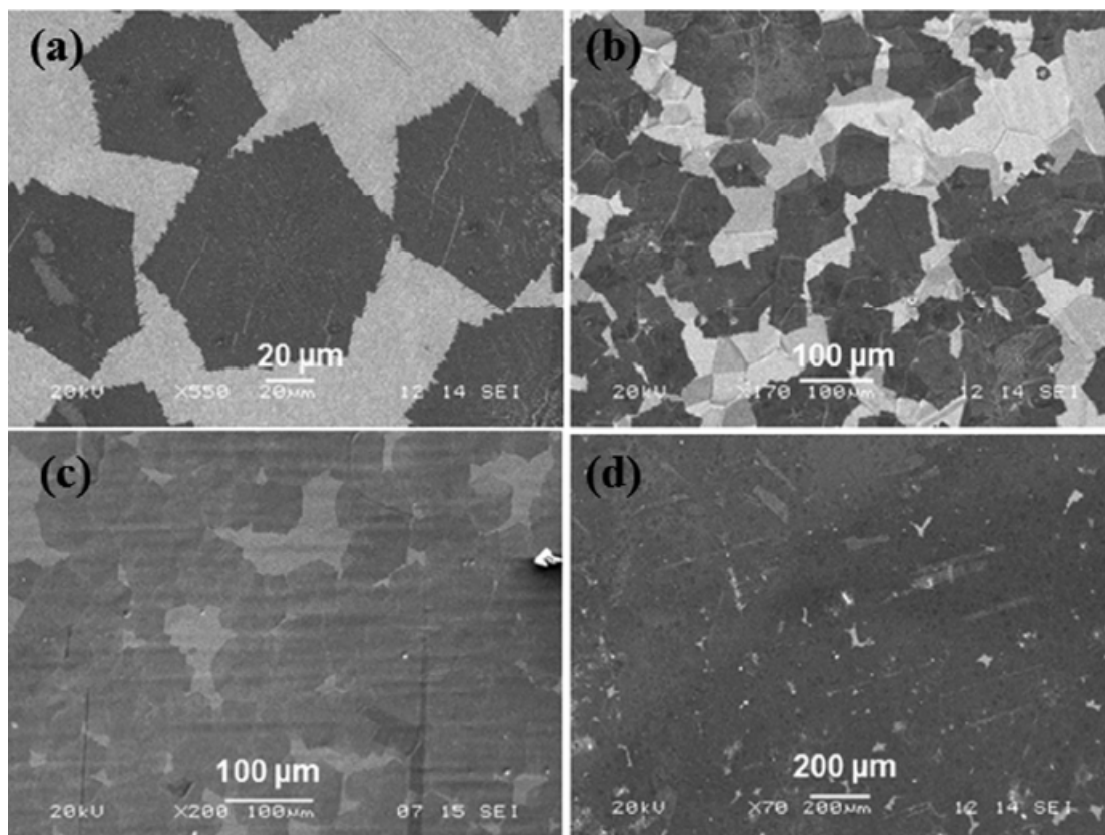


Figure 4.3: SEM images of (a) individual hexagonal graphene crystals (b) and (c) growing and merging graphene crystals (c) a merged structure to form a continuous film with a pyrolysis temperature increase rate of $1.5^{\circ}\text{C}/\text{min}$ of the waste plastic and continuous supply of carbon adatoms.

4.3.2 High pyrolysis rate

Figure 4.4 (a) shows synthesized graphene crystals with a pyrolysis rate of $1.5^{\circ}\text{C}/\text{min}$. In comparison, Figure 4.4 (b) shows crystals grown with a pyrolysis rate of $3^{\circ}\text{C}/\text{min}$. A second layer, grown on the top of the first one, can be observed. It is also confirmed with SEM in Figure 4.5 (a) where Raman spectra are taken at two different positions (Figure 4.5 (b)). G and 2D bands are observed at 1570 cm^{-1} and 2705 cm^{-1} , respectively. In position 1, the ratio $I_{2\text{D}}/I_{\text{G}}$, above 1, indicates a monolayer graphene while the ratio $I_{2\text{D}}/I_{\text{G}}$ in position 2, below 1, indicates a multilayer graphene flake. The presence of monolayer and multilayer graphene is confirmed by the FWHM of G and 2D bands which are 17.9 cm^{-1} and 45.1 cm^{-1} in position 1, respectively, and of 16.6 cm^{-1} and 37.9 cm^{-1} in position 2.

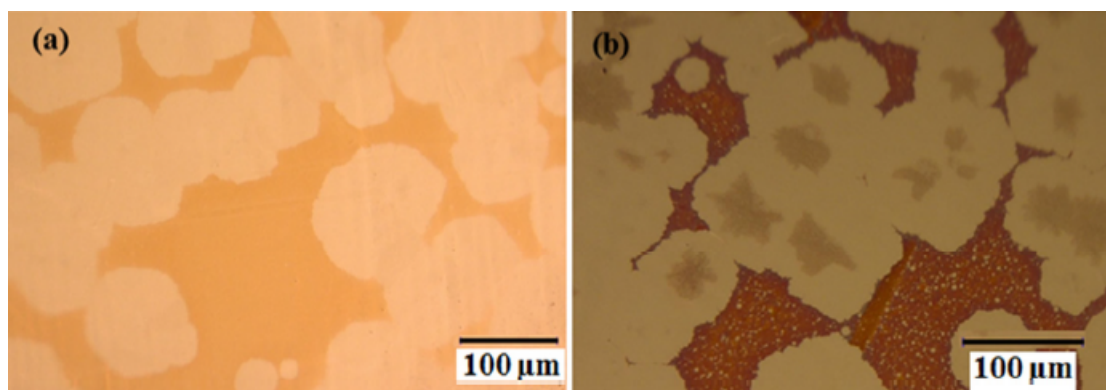


Figure 4.4: Optical microscope images of round-shaped graphene crystals synthesized on Cu foil with (a) lower ($1.5^{\circ}\text{C}/\text{min}$.) and (b) higher ($3^{\circ}\text{C}/\text{min}$) pyrolysis rates of waste plastic.

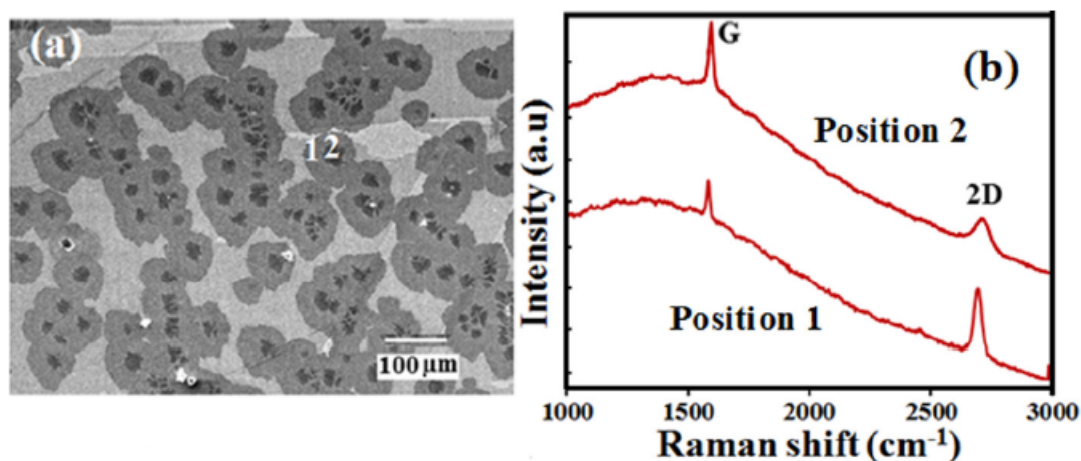


Figure 4.5: (a) SEM image of individual graphene crystals with few-layer morphology (b) Raman spectra of a graphene crystal at two different points (position 1 and 2).

A pyrolysis rate of $1.5^{\circ}\text{C}/\text{min}$, with continuous supply, is enough to produce crystals with well-defined edges. When the pyrolysis rate is increased, a larger amount of hydrocarbons is generated from the precursor and injected in the growth zone, onto the substrate. This higher amount of hydrocarbons is transformed into adatoms by catalysis on the substrate and influences graphene growth. Figure 4.6 (a) shows SEM images of individual graphene crystals grown at a pyrolysis rate

of $3^{\circ}\text{C}/\text{min}$. The second layer grown in the center of each crystals indicates a different morphology at this higher pyrolysis rate. While the graphene crystals have a size of $10\ \mu\text{m} - 100\ \mu\text{m}$, the upper layers are only $10\ \mu\text{m} - 30\ \mu\text{m}$, which are significantly smaller. Similar to the pyrolysis rate of $1.5^{\circ}\text{C}/\text{min}$, individual graphene crystals continue to grow with a longer duration until they merge, as shown in Figure 4.6 (b) and (c) [110]. Notably, Figure 4.6 (c) shows a high density of crystals with a second layer, where the black/grey contrast is clearly visible. The continuous film, Figure 4.6 (d), is observed with single and few-layer graphene merging, showing incomplete uniform growth at the high pyrolysis rate of $3^{\circ}\text{C}/\text{min}$

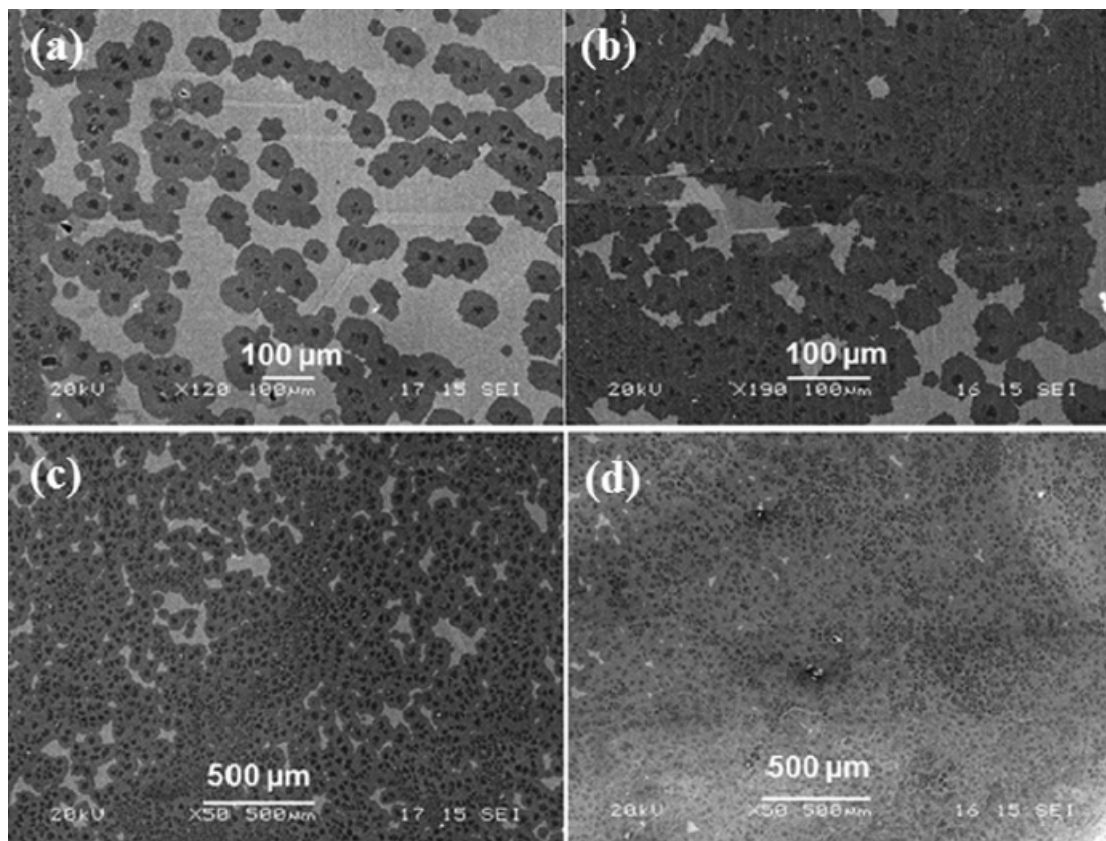


Figure 4.6: SEM image of (a) individual graphene crystals (b) and (c) growing and merging graphene crystals (d) merged graphene crystal structures in a continuous film with a higher pyrolysis temperature increase rate of $3^{\circ}\text{C}/\text{min}$ for the solid carbon source.

4.3.3 Model

In the cases of low and high pyrolysis rates, with a long duration, graphene crystals grow and merge into continuous graphene films. However, depending on the pyrolysis rate, these graphene crystals do not show the same morphology or number of layers. In the case of a low pyrolysis rate of $1.5^{\circ}\text{C}/\text{min}$, simple monolayer graphene crystal were formed, while an adlayer was grown on the top of the first layer at a high pyrolysis rate of $3^{\circ}\text{C}/\text{min}$; both growth processes are proposed in Figure 4.7. The high pyrolysis rate then produces a few-layer continuous film on the Cu substrate, which is not the most common structure on graphene [125].

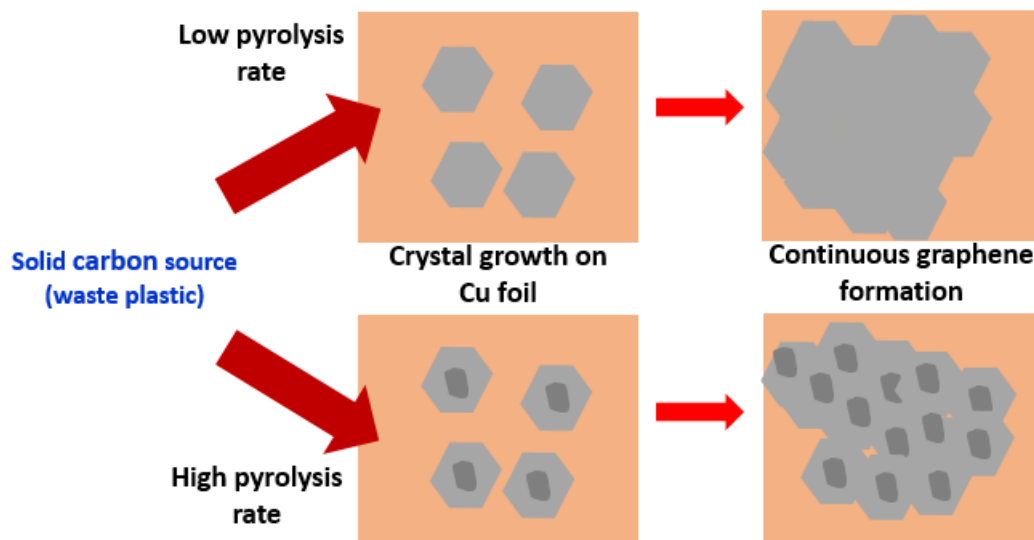


Figure 4.7: Schematic diagram of the graphene growth process on Cu foil in the developed CVD process.

The growth of few-layer graphene crystals has been observed with a high methane flow rate in a CVD process [84]. H_2 pressure also plays a role in the synthesis, where a high pressure of H_2 favors obtaining regular bilayer and few-layer hexagonal crystals while dendrite shaped graphene crystals were grown at a low H_2 pressure [104]. Graphene edge termination with H atoms and detaching from the Cu surface is observed at a high H_2 pressure, which enables diffusion of C species underneath the individual crystal for adlayer growth [180]. The combination of the H_2 pressure and the pyrolysis rate could be highlighted for the effect on the growth of crystals and their morphologies.

4.4 Conclusion

The carbon supply plays a major role in the growth of graphene, the termination of graphene crystals and for the morphology of the synthesized crystals. An abrupt end of the supply of carbon adatoms leads to unsaturated edges on the crystals, where nanoribbons are clearly visible. However, control of the pyrolysis rate can drastically change the synthesis of the different number of layers. A constant rate of $1.5^\circ\text{C}/\text{min}$ allows for the synthesis of well-defined graphene crystals, which can merge in a continuous film with a longer duration. In the case of a high pyrolysis rate of $3^\circ\text{C}/\text{min}$, a smaller grown second layer was observed on the top of the first layer. This high pyrolysis rate highlights the dramatic effects of a different carbon supply on graphene crystals therefore the need of its control and understanding. The critical role of the pyrolysis rate can be aligned with the effect of H_2 where the processes of growth at the level of the primary built layer needs better understanding, especially for the diffusion of C species underneath or on the top of the crystals.

Chapter 5

CuNi binary alloy catalyst for growth of nitrogen-substituted graphene by low pressure chemical vapor deposition

5.1 Introduction

Bilayer graphene shows a band gap [11, 135, 137], and it is wider for N-doped bilayer graphene (Figure 5.1 (b)), depending highly on the content of N atoms [167, 260]. The synthesis remains difficult due to low solubilities of C and N atoms in Cu substrate, commonly used for monolayer graphene (see Section 2.3.3.1), while Ni substrates have higher solubilities of these elements [205]. In spite of these higher solubilities, Ni substrates does not allow for a predictable segregation at the surface and the controllability for the number of layers is low (see Section 2.3.2). The CuNi binary alloy (Figure 5.1 (a)) would then possess the suitable controllability of both the number of layers [106, 261–263] and the N-doping concentration [165, 235]. This, in this chapter, the synthesis of N-doped bilayer graphene growth is explored on CuNi substrates with melamine as the sole precursor of both C and N atoms.

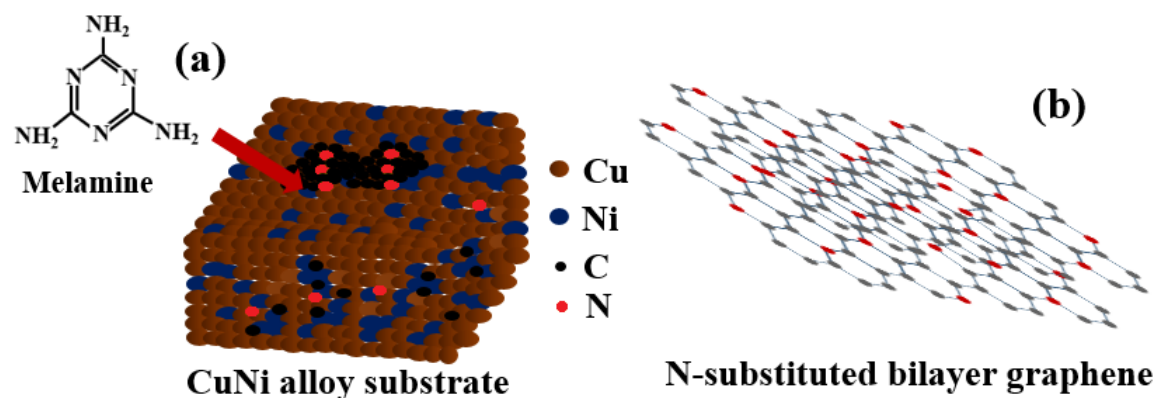


Figure 5.1: (a) CuNi alloy for growth of substituted N-doped graphene from melamine (b) Representation of N-doped bilayer graphene (N atoms in red).

5.2 Experimental part

A single furnace LPCVD was used for the experiments (Section 1.3.5), with a 70 cm long quartz tube with an inner diameter of 45 mm. After a base pressure of 2 Pa, a flow of 100 sccm of H₂ is introduced for the pre-annealing process and the 30 min of annealing. Then, the H₂ flow is cut off and a flow of 100 sccm of Ar was used for the deposition and the cooling. The precursor, melamine (≈ 120 mg) was approached on a moving support. The substrate is an untreated CuNi alloy from Nilaco Corp., with a composition of 70 wt% of Cu and 30 wt% of Ni, and a thickness of 0.10 mm. The sample was then transferred on a SiO₂/Si substrate by an electrochemical bubbling process and on a mesh, as described in Sections 1.4.2 and 1.4.3.

5.3 Results and discussion

5.3.1 Scanning Electron Microscopy and Raman spectroscopy

SEM and Raman analysis have been carried out on the graphene samples. Figure 5.2 (a) and Figure 5.2 (b) show SEM images of the N-doped graphene as synthesized on CuNi substrate and of the transferred sample on a SiO₂/Si substrate, respectively. Both images show non-uniform number of layers, indicated by the different levels of darkness. Darker areas indicate an increased number of layers.

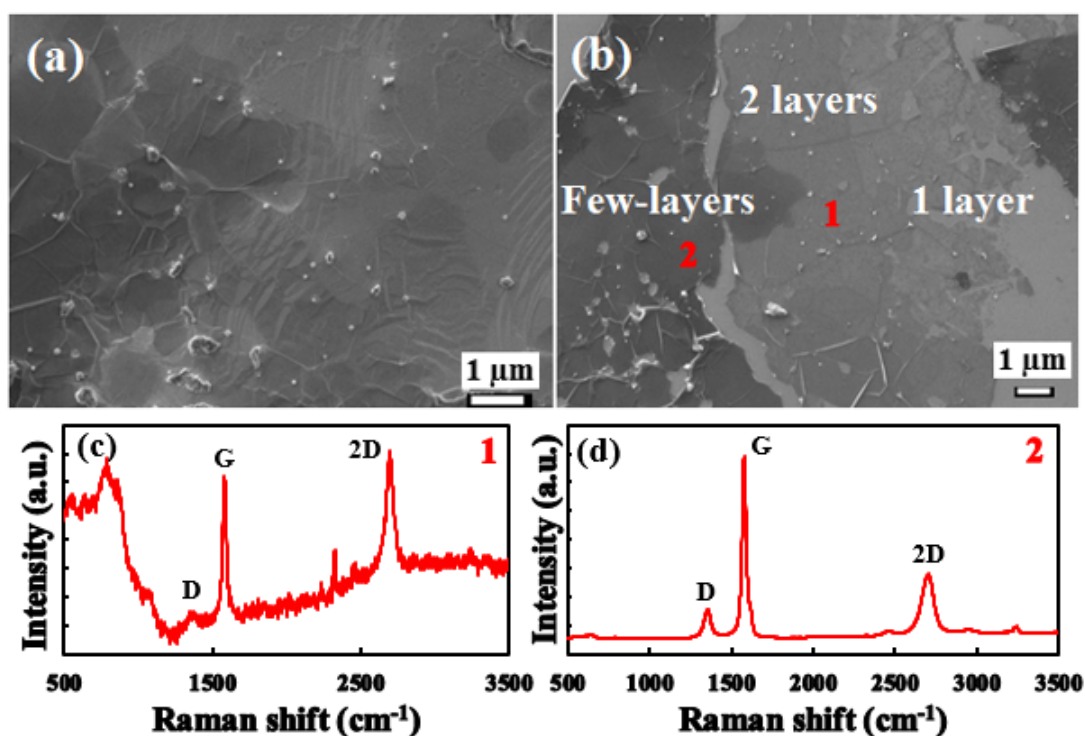


Figure 5.2: SEM images of (a) synthesized graphene on a CuNi substrate and (b) transferred graphene on a SiO₂/Si substrate (c) and (d) Raman spectrum at positions 1 and 2, respectively.

Raman spectra were performed to confirm the structure of graphene domains on the samples. Position 1 (Figure 5.2 (c)) shows G, D and 2D bands at 1570 cm⁻¹, 1340 cm⁻¹ and around 2690

cm^{-1} , respectively. The FWHM of the 2D band is 53.6 cm^{-1} , indicating bilayer graphene. The equivalent intensities of G and 2D bands at position 1 corresponds to bilayer graphene.

Figure 5.2 (d) represents position 2, where G and 2D bands are at 1570 cm^{-1} and 2692 cm^{-1} , respectively. The very high intensity of G band, in comparison to its 2D band, indicates the presence of multilayer graphene. The FWHM of the 2D peak is 81.6 cm^{-1} , confirming the obtaining of multilayer graphene.

5.3.2 Optical microscope and Raman mapping

Figure 5.3 (a) shows an optical image of transferred graphene domains on a SiO_2/Si substrate, where darker and lighter areas are observed, corresponding to multilayer, bi or monolayer. The Raman spectrum on Figure 5.3 (b), taken in the indicated bilayer area on Figure 5.3 (a), confirms the obtention of bilayer graphene with a ratio of 1 between the intensities of the 2D and G bands. This results is confirmed by the FWHM of the 2D band which is 51.3 cm^{-1} .

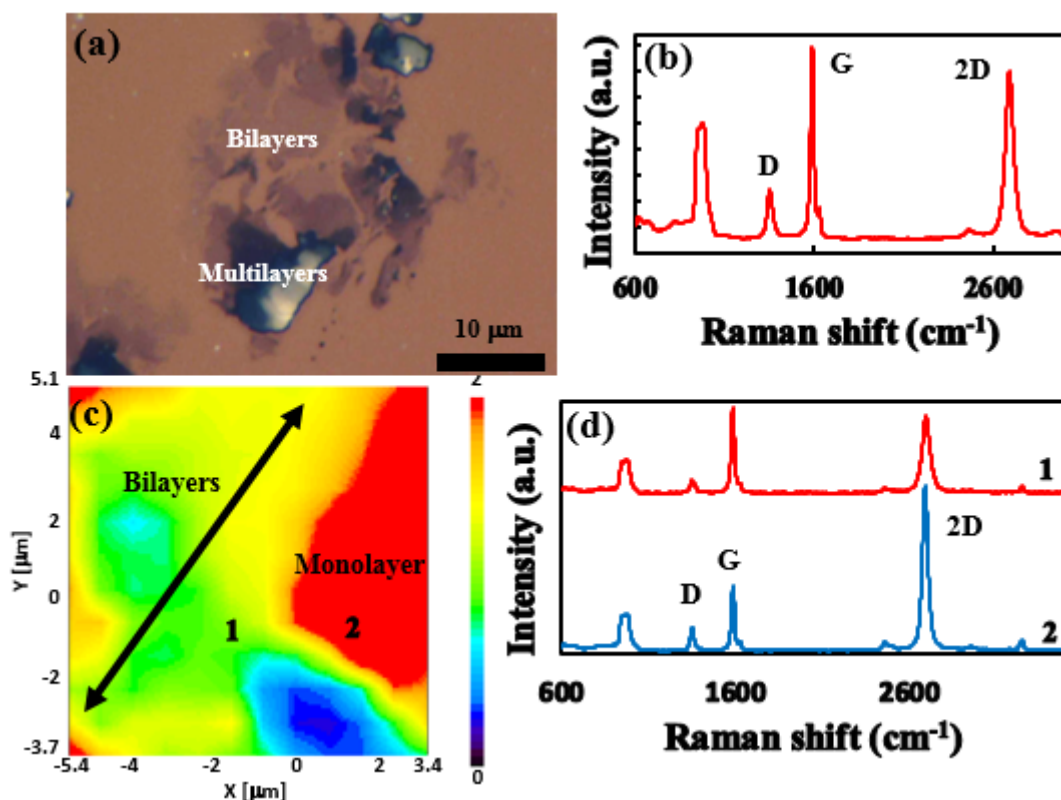


Figure 5.3: (a) Optical microscope image of transferred graphene on a SiO_2/Si substrate (b) Raman spectrum of the bilayer graphene in (a) image (c) Raman mapping of the transferred sample (d) Raman spectra bilayer and monolayer graphene at locations 1 and 2, respectively, of the mapping image.

Figure 5.3 (c) shows a Raman mapping on the same area as Figure 5.3 (a). The extracted Raman spectra from the Raman mapping are showed Figure 5.3 (d). Due to the intensities of the G and 2D bands, it is possible to conclude that a few-layer area is observed, along with a $10 \mu\text{m}$ area of monolayer graphene, at locations 1 and 2, respectively. The observations of the mapping and of the individual spectra are confirmed by the FWHM of the 2D bands: 51.8 cm^{-1} at location 1

and 37.0 cm^{-1} at location 2. The ratio of Ni in the binary alloy and growth conditions need to be optimized for growth of N-doped graphene with uniform number of layers in a large-area.

5.3.3 XPS, TEM and AFM analysis

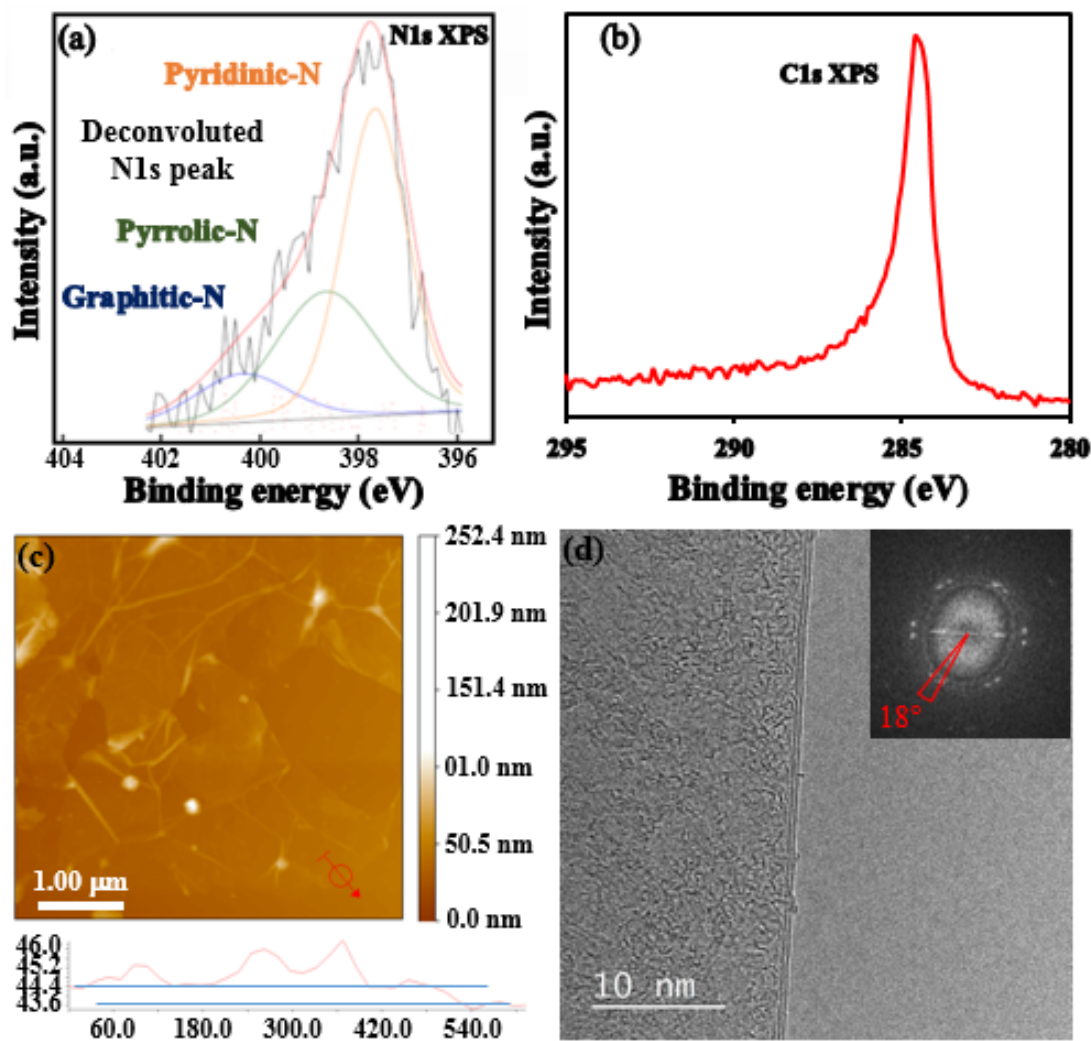


Figure 5.4: XPS analysis (a) Deconvoluted N1s peak and (b) C1s peak (c) AFM analysis and thickness profile (X and Y axis in nm) (d) TEM image of a bilayer graphene (inset shows the Fast Fourier Transform pattern).

The atomic content of the sample was analyzed by XPS analysis. Figure 5.4 (a) shows the deconvoluted N1s peak with peaks at 397.5 eV, 399 eV and 400.5 eV for pyridinic, pyrrolic and graphitic-N. Pyridinic-N bonds with two carbon atoms at the edges or the defects of graphene and with its sp^2 hybridization contributes with one electron to the π system. Pyrrolic N refers to N atoms that are sp^3 hybridized and contribute with two electrons to the π system [162]. Graphitic-N atoms substitute carbon atoms in the hexagonal ring, and so are sp^2 hybridized, and disturb the less the graphitic network [198, 264]. The overall atomic percentage for N is found to be around 5.8 at% from the N1s peak area and intensity. Figure 5.4 (b) shows the C1s peak for the N-doped graphene. A broad peak at a higher binding energy ($\approx 406 \text{ eV}$) was not observed for the N1s peak,

confirming the absence of formation of NO_x .

Figure 5.4 (c) shows an AFM image at a selected area of the transferred graphene sample on the SiO_2/Si substrate. A folded and wrinkled graphene sheet are clearly shown in the AFM image. The thickness of the graphene was measured at an unfolded edge and without any wrinkle as shown by the red arrow in Figure 5.4 (c). The thickness of the graphene layer is around 0.8 nm, corresponding to bilayer graphene. Figure 5.4 (d) shows a TEM image of bilayer graphene transferred onto a mesh.

The inset of Figure 5.4 (d) shows the Fast Fourier Transform (FFT) pattern for the bilayer graphene. The FFT pattern clearly shows the formation of a twisted bilayer graphene, with a twist angle of around 18° [265]. Twisted bilayer graphene shows interesting properties [266], such as a Dirac spectrum with θ -dependent Fermi velocity [267–269], low-energy Van Hove singularities [270–272] and other θ -dependent physical and chemical phenomena [273, 274]. However, this twist angle of 18° doesn't give any indication about the stacking of the two layers of graphene. The current synthesis methods for twisted bilayer graphene are limited to small domain size and uncontrollable twist angles, even if the growth of $100\ \mu\text{m}$ crystals has been reported [275].


5.4 Conclusion

The difference in solubilities of C and N elements in Cu and Ni metals, could be have been used in the CuNi binary alloy catalyst to synthesize N-doped graphene films, by the LPCVD technique. CuNi alloy is a suitable substrate for the growth of graphene with high percentages of N doping, especially with a melamine precursor where N atoms are already included in the main ring. The as-synthesized film contains a total of 5.8 at% of nitrogen, including pyridine, pyrrolic and graphitic nitrogen, which opens perspectives for the use in transistors and other electronic devices. Small domains of $100\ \mu\text{m}$ have been obtained, both bilayer and multilayer. The obtained N-doped bilayer are twisted by 18° , which could have implications in the electronic properties.

Chapter 6

Formation of graphene nanoribbons and Y-shaped structures by hydrogen induced anisotropic etching

6.1 Introduction

raphene nanoribbons have sparked a huge interest, unlike in monolayer graphene, due to the existence of a band gap [11, 139–142]. Its synthesis was made by various approaches, both top-down and bottom-up [147–159]. Due to the significant differences in chemical reactivity of the zigzag and armchair edges, anisotropic etching of graphene can be achieved [251, 276, 277]. This anisotropic etching shows a way to control the structure of large-area CVD synthesized graphene with metal catalytic nanoparticles [156, 278–280] selective oxidation [276], and water vapor at an elevated temperature [281] and other graphene patterns [282]. Thus, H₂ anisotropic etching allowed for the formation of pentagonal graphene domains [283]. In this chapter, H₂ anisotropic etching was explored in order to investigate the formation of specific structure on the previously formed graphene, from hexagonal holes to nanoribbons. The created holes with a defined edge structure also provide a platform to fabricate in-plane heterostructure with other 2D materials [284, 285]. The formation of Y-shaped zigzag graphene nanoribbons is of prime importance due to the predicted electronic properties [286–290] and the possibility of fabrication of multiterminal graphene-based nanoelectronic and spintronic devices [291, 292].

6.2 Experimental part

As explained in Section 1.3.4, a two furnaces APCVD system was used for the experiments. Camphor was used as the solid precursor, along with a Cu substrate from Nilaco Corp. with a thickness of 20 μm and a purity of 99.98%, for the synthesis of graphene crystals. The Cu foil was cleaned in acetone by sonication prior to synthesis. The growth furnace, with the Cu foil, was heated until 1000°C with 100 sccm of H₂ gas and then annealed for 15 min. A mixture of Ar and H₂ (98 : 2 sccm) was introduced for the growth, etching and the cooling process.

6.3 Synthesis of graphene flakes

Prior to the etching process, graphene flakes and films were synthesized. Figure 6.1 (a) and (b) show optical microscope images of graphene flakes produced inside the APCVD system with camphor as a precursor. The Cu foil substrate on which the graphene crystals are grown was slightly oxidized in order to create a contrast between graphene flakes, in white, and the slightly orange colors of Cu oxides. As seen in Chapter 3, a longer duration of the growth led to the synthesis of continuous films.

The synthesized graphene is characterized by a Raman spectrum, shown in Figure 6.1 (c). The graphitic G and second-order 2D Raman bands were observed around 1589 cm^{-1} and 2690 cm^{-1} , respectively. The intensity ratio I_{2D}/I_G of the 2D and G bands, respectively, is clearly above 1, indicating the synthesis of monolayer graphene.

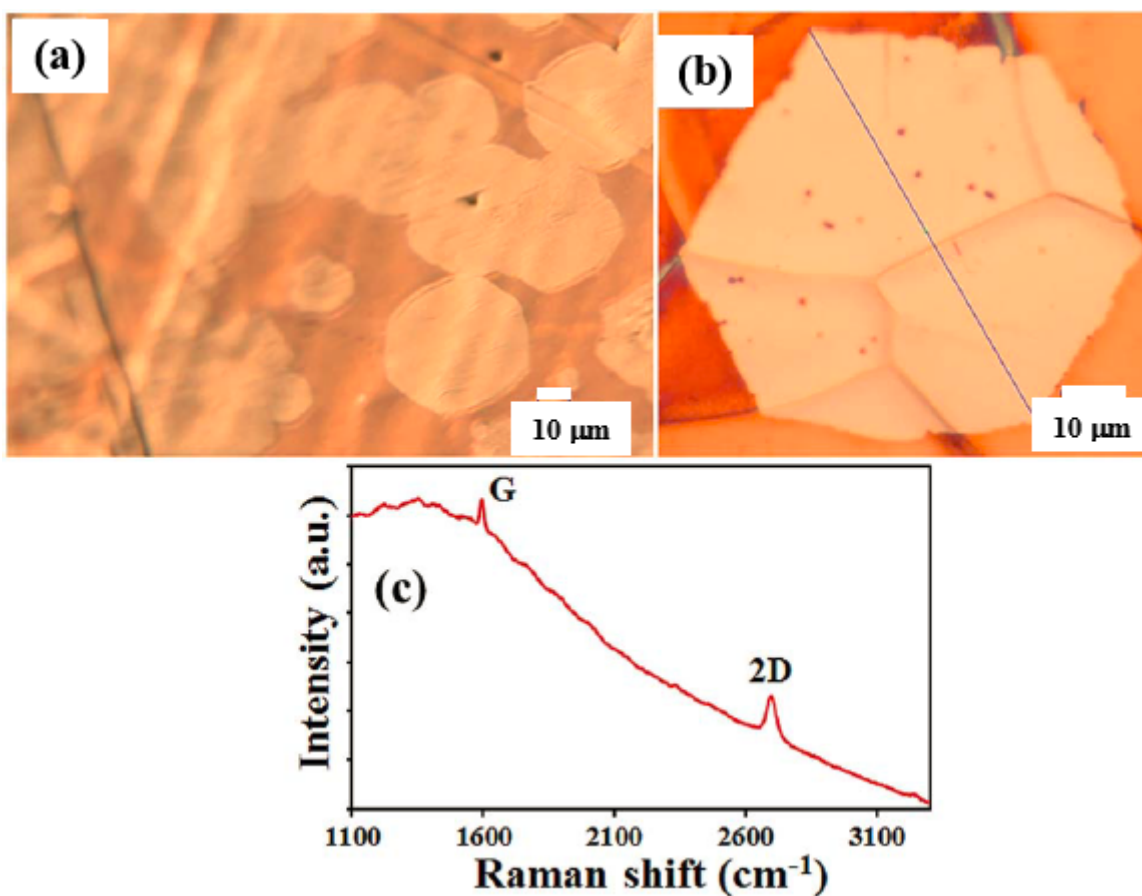


Figure 6.1: (a and b) Optical microscope images of graphene crystals grown from solid camphor precursor by APCVD process (c) Raman spectrum of the synthesized graphene on Cu foil.

6.4 Etching process

After the synthesis, the carbon supply was shut off and the (98 : 2 sccm) Ar : H₂ gas mixture continued to flow, slowly etching the graphene crystals at 1000°C. Etching had been investigated in Ar but these particular etching effects were not observed in these conditions; Ar : H₂ gas mixtures

seem to be the most effective process to achieve controllable graphene etching. Figure 6.2 (a) and (b) show optical images of etched graphene crystals, where the formation of ribbons and holes inside the graphene crystals is clearly observable with well-defined edges. The etching process led to the formation of hexagonal holes such as the one shown in Figure 6.2 (c). The etching reaction can be understood as the effective reverse reaction of the graphene growth process where H_2 can react with the carbon atoms of graphene catalyzed by Cu to produce methane [156, 251, 282, 293]. Raman spectra of the graphitic structure (red curve) and of the etched part (blue curve) are shown in Figure 6.2 (d): G and 2D bands were observed for the graphitic structure but only the copper oxide band was observable in the etched part, indicating the absence of graphene.

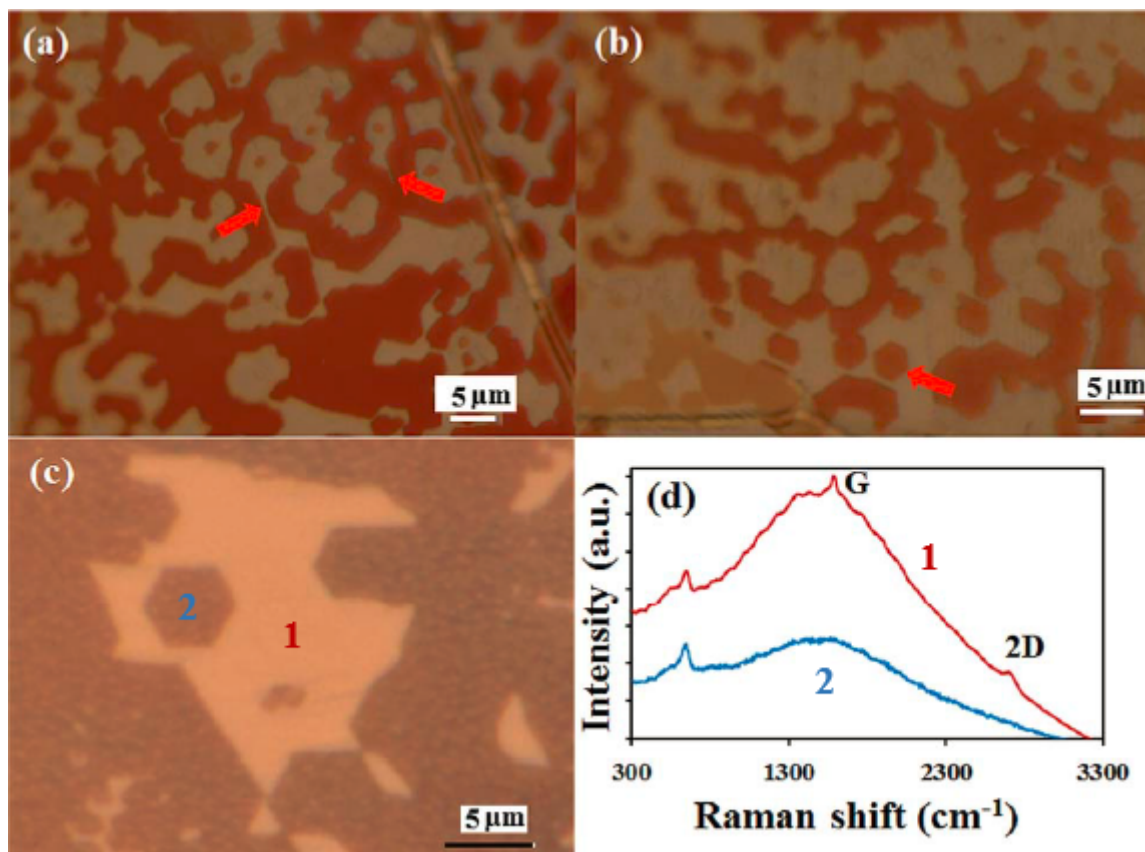


Figure 6.2: Optical microscope images (a and b) of the etched graphene sample by annealing at 1000°C in an Ar : H_2 gas mixture (c) etched graphene crystal with formation of a well-defined hexagonal hole (d) Raman spectra of the etched graphene and partially oxidized Cu surface.

The FE-SEM analysis has been performed on the sample with an Upper Electron Detector (UED) at an accelerating voltage of 2 kV (Figure 6.3 (a)). The studied back-scattered electrons (BSE) reflect the composition of the sample, as the back-scattered electron are dependent on the atomic number Z (see Section 1.5.3). The bright spots correspond to SiO_2 nanoparticles inside etched zones as well as graphene crystals, which can act as defect sites on the Cu foil. Thus, the etching process can start at a defect site and continue with the copper substrate as a catalyst for the H_2 reaction with sp^2 hybridized carbon atoms. Figure 6.3 (b) shows an FE-SEM image with morphological variations. The elementary mapping analyses after partial oxidation of the etched graphene for carbon and oxygen are shown in Figure 6.3 (c) and in Figure 6.3 (d), respectively. The significant difference in concentrations of carbon and oxygen shows where the etched graphene structures lie coupled with the base of the Cu surface, oxygen is at minimum concentrations. The

AES analysis (Figure 6.3 (e)) of an etched graphene structure on Cu foil confirms the remaining graphene structures on the Cu foil.

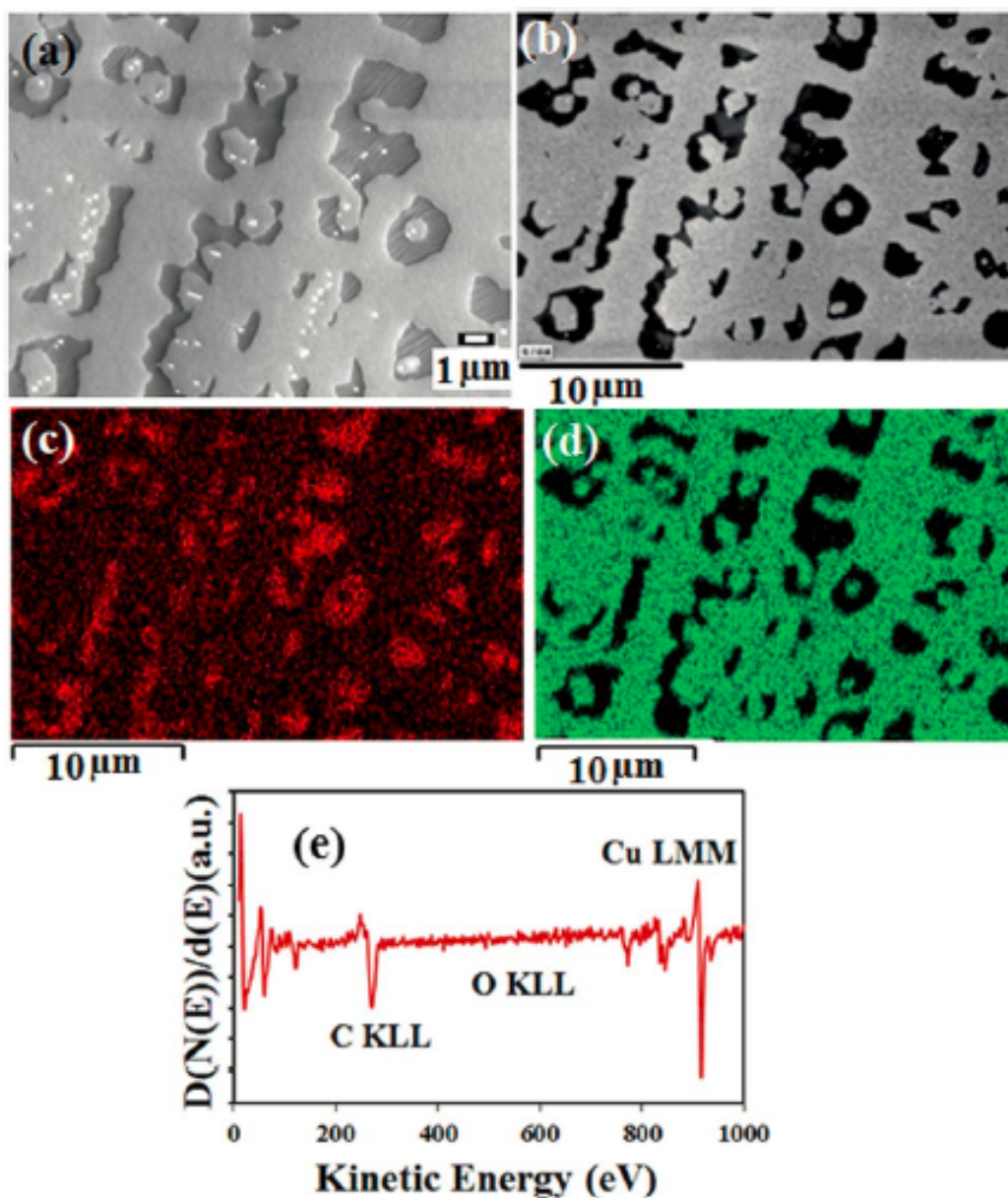


Figure 6.3: (a) FE-SEM image corresponding to back scattered electrons (BSE) providing compositional contrast. SiO_2 nanoparticles were observed as bright contrasts inside the holes of graphene crystals and etched areas (b) FE-SEM analysis (c) and (d) elementary mapping for carbon and oxygen (e) selective AES analysis of the etched graphene structure on Cu foil.

6.5 Formation of particular structures

The etched graphene crystals of the sample have been investigated by SEM analysis and different structures with well-defined edges were observed in a SEM image of Figure 6.4 (a). FE-SEM analysis was also used with a Low Electron Detector (LED) at an accelerating voltage of 5 kV.

Figure 6.4 (b) and Figure 6.4 (c) show etching along symmetric directions of the graphene lattice where the formation of edges takes place at 60° and 120° along straight lines. Ci et al [278] obtained similar results with nickel nanoparticles assisting the etching process. The etching process does not affect the quality of the synthesized graphene, which shows the importance of the H_2 etching process for obtaining triangular-shaped graphene and graphene nanoribbons with the control of edge structures.

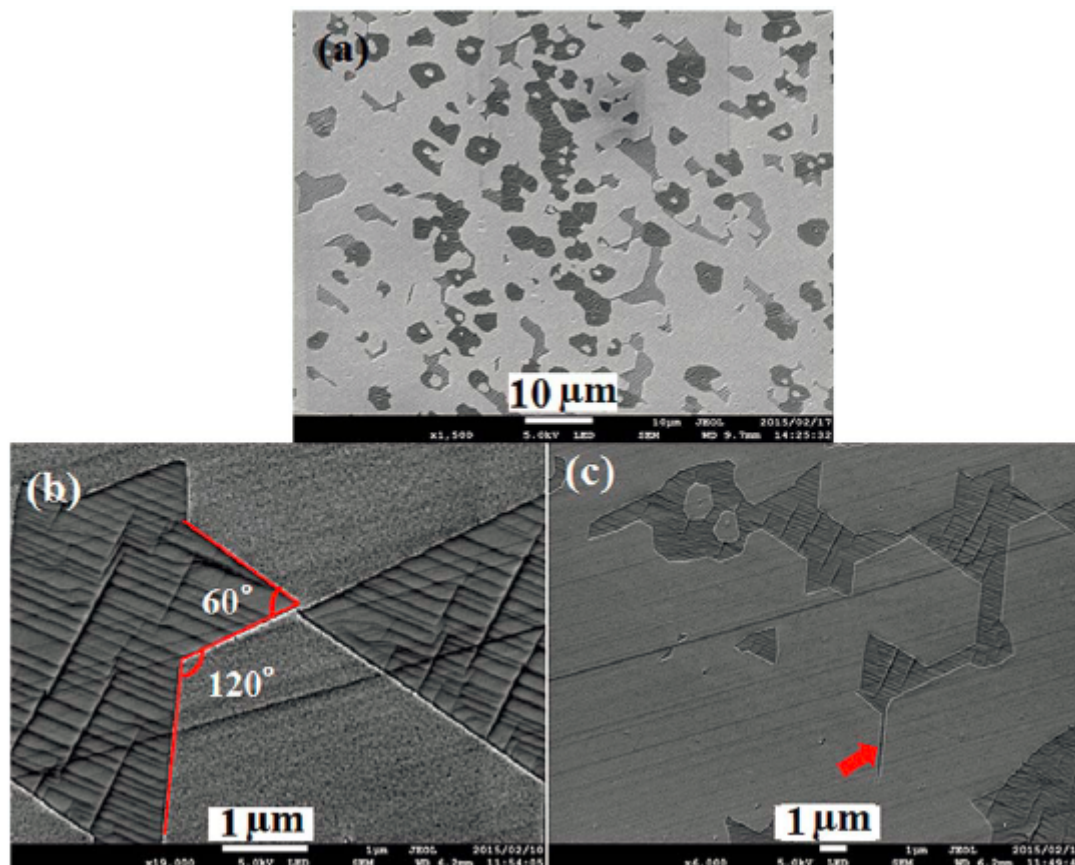


Figure 6.4: FE-SEM images of (a) etched graphene sample, showing various structures with pronounced edges. FE-SEM images of (b and c) graphene edges with 60° and 120° , indicating etching along symmetric directions of the graphene lattice.

Other structures were also studied by FE-SEM, as shown in Figure 6.5. In Figure 6.5 (a), hexagonal holes and ribbon structures are observed. Similar to the previous observation of angles at 60° and 120° , the sharp etched edges indicate an ordered etching which can lead to the creation of hexagonal and triangular holes inside the graphene lattice. The increase in annealing duration defines the range of etching which is of significant importance for the control of the size and structure of graphene etching. These holes could be used as platforms for in-plane heterostructures with other 2D materials, such as hexagonal boron nitride [284, 285].

Gothard et al [294] presented a three-terminal Y-shaped nanotubes which exhibits a gating behavior, characteristic of transistors. In Figure 6.5 (b), a Y-shaped graphene structure is shown with perfect ribbons at 120° which form the structure. Similar to the Y-shaped nanotubes, Y-shaped graphene ribbons with zigzag ordered edge structures can be applied in multiterminal graphene-based nanoelectronics devices [291, 292]. Nevertheless, the spatial control of the formation of Y-shaped graphene nanoribbons by H_2 anisotropic etching can be challenging. A study of the

edges, its width and its properties of the fabricated nanoribbons could be performed by a TEM analysis.

Figure 6.5 (c) and Figure 6.5 (d) show the formation of a graphene nanoribbon structure between two larger graphene domains through the etching process. The width of the nanoribbon is not constant, with 67.7 nm on one end and 17.0 nm on the other, which affects its properties [143]. However the fabrication of nanoribbons with a width below 10 nm can be made possible by the controlled etching process as well as the synthesis of nanoribbons by organic chemistry (bottom-up approach) [149, 150].

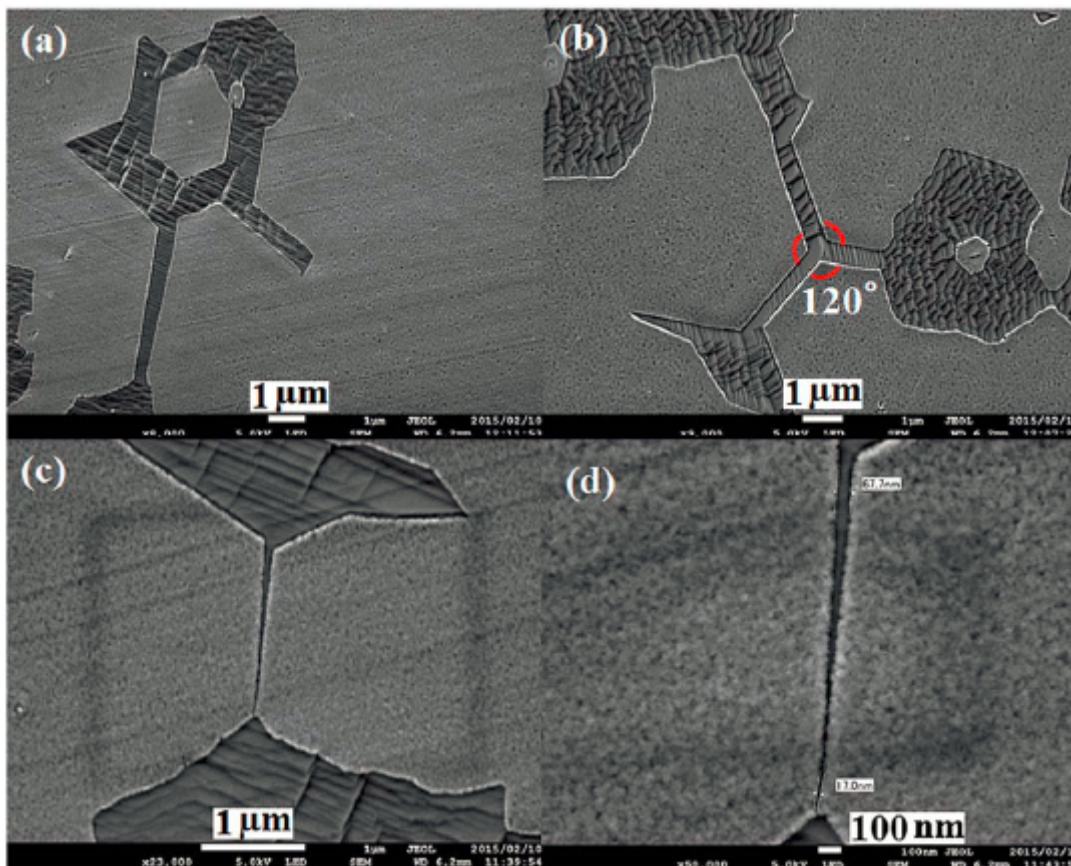


Figure 6.5: FE-SEM images of (a) an ordered etched hexagonal hole as well as ribbon like graphene structure (b) formation of Y-shaped graphene ribbons structure with edge etching (three ribbons form 120° to each other) (c and d) nanoribbon structure with the etching process on Cu foil. The nanoribbon is formed with interconnection of two larger graphene domains.

6.6 Conclusion


After the synthesis of graphene crystals and films, anisotropic etching by an Ar : H₂ mixture was observed and enhanced with an increase in annealing duration, until etching large part if not all of the previously formed graphene. The formation of etched, ordered hexagonal holes in the films was noticed with a short etching time. When a more significant part of the graphene was etched, nanoribbons, Y-shaped and other graphene structures were formed. Nanoribbons were particularly observed as an interconnection between two larger graphene domains, despite its non-uniform

width. Individual ribbons with angles of 120° form a Y-shaped structure with well-defined edges, which could be used in multi-terminal graphene-based nanoelectronics devices, such as transistor and spintronic applications. Anisotropic etching shows its controllability with H_2 to fabricate particular graphene structures with preferential edges for electronic device applications.

Chapter 7

Conclusion

7.1 Summary

VD systems have emerged as a potential large-scale method for the synthesis of graphene. The control of this synthesis of graphene on transition metals substrates with solid precursors in a process of optimization of numerous parameters, has been achieved in order to obtain high quality graphene and large crystals. The functionalization of graphene has also been pursued to generate a band gap which is non-existent in pure monolayer graphene.

The designs of experiments show the existence of an optimum for the studied parameters, such as the quantity of a carbon source precursor, inside the CVD system. The growth temperature is seen as having an important effect on the substrate as well as on the formation of adatoms, especially through the decomposition and the catalysis, but the proximity with the melting point of the used substrate, Cu, limits the increase of this growth temperature and its use. Nevertheless, the size of graphene crystals is dramatically affected by the manipulation of only two parameters, the growth time and the pyrolysis rate of the carbon source precursor. Another improvement for the size of graphene crystals had been made possible through a smoother surface, resulting in less nucleation sites, with the modification of copper surfaces by electropolishing.

The growth of graphene on Cu substrates, through nucleation process and enlarging size with newly created adatoms, is highly dependent on the supply of carbon. An abrupt cut of the carbon supply leads to the formation of unsaturated edges on graphene crystals, while a smooth termination of the growth paves the way to well-defined edges of graphene crystals. On the other hand, a change in the pyrolysis rate from 1.5°C/min to 3°C/min shapes the formation of a second layer on the top of graphene crystals with well-defined edges.

On the contrary to Ni and Cu substrates, where solubilities of C and N are determined, these could be controlled in a CuNi binary alloy. The surface and bulk reactions could then be tunable and lead to the desired number of layers of graphene at the surface of the alloy. Bilayer and multilayer graphene were observed with a small size of 10 μm. Melamine is an organic chemical compound with an aromatic ring containing both C and N atoms, which makes it an ideal sole precursor for the synthesis of N-doped graphene crystals. The formation of bilayer N-doped graphene, with an incorporation of 5.8 at% of nitrogen, is then relevant to open a band gap as shown by

theoretical studies. TEM also confirms the twisting of the N-doped bilayer graphene by 18° which has interesting electronic properties.

The opening of a band gap can also be obtained by the creation of nanoribbons. If studies have been conducted for the bottom-up synthesis from chemical species, the anisotropic etching of CVD synthesized graphene crystals with significant annealing time and H_2 quantity, controlled in a mixture with Ar and H_2 (98 sccm : 2 sccm) at an annealing temperature of 1000°C , has shown the possible fabrication of well-defined nanoribbons and specific structures with clear edges. The creation of hexagonal holes in graphene films clearly demonstrates that etching is the reverse process of the graphene growth. Two interconnected large graphene domains by a uniform width nanoribbon was observed along with individual nanoribbons with angles of 120° forming a Y-shaped structure. The Y-shaped graphene nanoribbon could be used to fabricate multi-terminal graphene-base transistors, nanoelectronic devices and spintronic applications.

7.2 Future prospects

The use of graphene in various fields of electronics requires the synthesis of high quality graphene with minimal defects on large scale. The use of CVD systems could fulfil these needs. However the control of all its aspects, such as gas pressures and temperatures, as well as the gas composition and the morphology of the substrates are of major importance for the controlled synthesis of graphene crystals and films. Furthermore, the oxidation of the substrate to limit the number of nucleations or a tuned supply of adatoms could lead to bigger size of graphene crystals with a better quality.

The use of different organic chemicals such as camphor and melamine, or mixture of several compounds such as the waste polymer precursor, lead to diverse results. Notably, the waste polymer precursor is composed of polystyrene and polyethylene and the study of their ratio could give further indications on the growth mechanism. The study of other chemical compounds, especially with ring structures such as naphthalene, phenanthrene, pentacene, chrysene or triphenylene, could lead to the interesting formation of graphene at various temperatures and conditions.

The functionalization of graphene could be improved by a higher incorporation of N atoms in the graphene network. The graphitic nitrogen is especially interesting because it does not disturb the carbon network. An intimate knowledge of the alloy substrates is necessary for the synthesis of the number of graphene layers with the adequate quantities of C and N, to tune the resulting band gap. In the case of anisotropic etching, improvements are required in the formation of spatially designed structures, especially for the control of the etching and the understanding of its process.

These advances will bring graphene a step closer to a widespread use in industry, especially in materials and electronics. The target is now possible applications and manufacturing processes. The flexibility of graphene could enhance its use in rolled-up screens and wearable devices. Finally, this wonder material, as it has been called more than once, may fulfil its promises in a near future. The integration of other 2D materials and hybrid systems could bring a new dimension to future technologies, creating thinner, more flexible, faster and stronger devices.

Bibliography

- [1] U.S. Geological Survey, *Mineral Commodity Summaries, Indium*. 2007. URL: <http://minerals.usgs.gov/minerals/pubs/commodity/indium/indiumcs07.pdf>.
- [2] U.S. Department of energy, *Critical Materials Strategy Summary*. 2010. URL: http://energy.gov/sites/prod/files/edg/news/documents/Critical_Materials_Summary.pdf.
- [3] *Chemistry World Magazine, Endangered elements*. 2011. URL: www.rsc.org/images/Endangered%20Elements%20-%20Critical%20Thinking_tcm18-196054.pdf.
- [4] Renouf C. A touch of indium. *Nature Chemistry*, 4 (2012), 862.
- [5] Peng C., Jia Z., Bianculli D., Li T., and Lou J. In situ electro-mechanical experiments and mechanics modeling of tensile cracking in indium tin oxide thin films on polyimide substrates. *Journal of Applied Physics*, 109 (10) (2011), 103530.
- [6] Peng C., Jia Z., Neilson H., Li T., and Lou J. In Situ Electro-Mechanical Experiments and Mechanics Modeling of Fracture in Indium Tin Oxide-Based Multilayer Electrodes. *Advanced Energy Materials*, 15 (4) (2013), 250–256.
- [7] Yang S., Ng E., and Lu N. Indium Tin Oxide (ITO) serpentine ribbons on soft substrates stretched beyond 100%. *Extreme Mechanics Letters*, 2 (2015), 37–45.
- [8] Bae S., Kim H., Lee Y., Xu X., Park J. S., Zheng Y., Balakrishnan J., Lei T., Kim H. R., Song Y. I., Kim Y.-J., Kim K. S., Ozyilmaz B., Ahn J. H., Hong B. H., and Iijima S. Roll-to-roll production of 30-inch graphene films for transparent electrodes. *Nature Nanotechnology*, 5 (2010), 574–578.
- [9] Lin Y. M., Dimitrakopoulos C., Jenkins K. A., Farmer D. B., Chiu H.-Y., Grill A., and Avouris P. 100-GHz Transistors from Wafer-Scale Epitaxial Graphene. *Science*, 327 (5966) (2010), 662.
- [10] Schwierz F. Graphene transistors. *Nature Nanotechnology*, 5 (2010), 487–496.
- [11] Reddy D., Register L. F., Carpenter G. D., and Banerjee S. K. Graphene field-effect transistors. *Journal of Physics D: Applied Physics*, 44 (31) (2011), 019501.
- [12] Zeng M., Shen L., Zhou M., Zhang C., and Feng Y. Graphene-based bipolar spin diode and spin transistor: Rectification and amplification of spin-polarized current. *Physical Review B*, 83 (2011), 115427.
- [13] Zhu Y., Sun Z., Yan Z., Jin Z., and Tour J. M. Rational Design of Hybrid Graphene Films for High-Performance Transparent Electrodes. *ACS Nano*, 5 (8) (2011), 6472–6479.
- [14] Moddel G., Zhu Z., Grover S., and Joshi S. Ultrahigh speed graphene diode with reversible polarity. *Solid State Communications*, 152 (19) (2012), 1842–1845.

- [15] Liu J., Yin Z., Cao X., Zhao F., Wang L., Huang W., and Zhang H. Fabrication of Flexible, All-Reduced Graphene Oxide Non-Volatile Memory Devices. *Advanced Materials*, 25 (2012), 233–238.
- [16] Boardman J., Edwards I. E. S., Hammond N. G. L., and Sollberger E. *The Prehistory of the Balkans; and the Middle East and the Aegean world, tenth to eighth centuries B.C.* Second edition. Vol. 3.1. The Press syndicate of the University of Cambridge, 1982. URL: <https://web.archive.org/web/20130225042733/http://home.lu.lv/~harijs/Macibu%20materiali%20,teksti/Cambrige%20Ancient%20History/Cambridge%20Ancient%20History%203.1.%20Balkans,%20Middle%20East%20&%20Aegean%20World%2010-8th%20c.pdf>.
- [17] Martineau H. *Complete guide to the English lakes.* p. 156. Windermere - John Garnett ; London : Whittaker and Co., 1855. URL: <https://archive.org/details/completeguideto1855mart>.
- [18] Basket M. *Statutes at large: from the Twentieth year of the reign of King George the Second to the thirtieth year of rein of King George the Second.* Vol. 7. p. 415. Basket, Robert, Woodfall, Henry, and Strahan, William, 1764. URL: https://books.google.co.jp/books?id=eaRFAAAAcAAJ&pg=PA415&redir_esc=y#v=onepage&q&f=false.
- [19] Werner A. G. Mineralsystem des Herrn Inspektor Werners mit dessen Erlaubnis herausgegeben von C. A. S. Hoffman. *Bergmännisches Journal*, 1 (1789), 369–398. URL: http://rruff.info/uploads/Bergmannisches_Journal_1_1789_369.pdf#page=13.
- [20] Widenmann J. F. W. *Handbuch des oryktognostischen Theils der Mineralogie.* Vol. 206, p 651. Sigfried Lebrecht Crusius, Liepzig, 1794. URL: https://books.google.co.jp/books?id=9QxQAAAAcAAJ&pg=PA651&redir_esc=y#v=onepage&q&f=false.
- [21] Brodie B. C. XXIII.—Researches on the atomic weight of graphite. *Quarterly Journal of the Chemical Society of London*, 12 (1860), 261–268.
- [22] Chua C. K. and Pumera M. Chemical reduction of graphene oxide: a synthetic chemistry viewpoint. *Chemical Society Reviews*, 43 (1) (2014), 291–312.
- [23] Boehm H.-P., Setton R., and Stumpp E. Nomenclature and terminology of graphite intercalation compounds. *Pure and Applied Chemistry*, 66 (9) (1994), 1893–1901.
- [24] Saito R., Dresselhaus G., and Dresselhaus M. S. *Physical Properties of Carbon Nanotubes.* Imperial College Press, 1998. URL: <http://www.worldscientific.com/worldscibooks/10.1142/p080#t=aboutBook>.
- [25] Peierls R. Quelques propriétés typiques des corps solides. *Annales de l'institut Henri Poincaré*, 5 (3) (1935), 177–222.
- [26] Landau L. D. Zur Theorie der phasenumwandlungen I. *Physikalische Zeitschrift der Sowjetunion*, 11 (1937), 26–35.
- [27] Landau L. D. Zur Theorie der phasenumwandlungen II. *Physikalische Zeitschrift der Sowjetunion*, 11 (1937), 545.
- [28] Wallace P. The Band Theory of Graphite. *Physical Review*, 71 (1947), 622–634.
- [29] Geim A. K. Graphene: Status and Prospects. *Science*, 324 (5934) (2009), 1530–1534.
- [30] Barth A. and Marx W. Graphene - A rising star in view of scientometrics. *Physics and Society*, 0808 (2008), 3320. URL: <https://arxiv.org/abs/0808.3320>.
- [31] Mohsin A. Graphene synthesis and characterization on copper. MA thesis. University of Iowa, 2012. URL: <http://ir.uiowa.edu/etd/3354/>.

- [32] Cheng D., Barcaro G., Charlier J.-C., Hou M., and Fortunelli A. Homogeneous Nucleation of Graphitic Nanostructures from Carbon Chains on Ni (111). *The Journal of Physical Chemistry C*, 115 (2011), 10537–10543.
- [33] Peschel G. *Carbon-Carbon bonds: Hybridization*. 2011. URL: http://www.physik.fu-berlin.de/einrichtungen/ag/ag-reich/lehre/Archiv/ss2011/docs/Gina_Peschel-Handout.pdf.
- [34] Castro-Neto A. H., Guinea F., Peres N. M. R., Novoselov K. S., and Geim A. K. The electronic properties of graphene. *Review of Modern Physics*, 81 (1) (2009), 109–162.
- [35] Goerbig M. O. Electronic properties of graphene in a strong magnetic field. *Reviews of Modern Physics*, 83 (4) (2011), 1193–1243.
- [36] Morozov S. V., Novoselov K. S., Katsnelson M. I., Schedin F., Elias D. C., Jaszczak J. A., and Geim A. K. Giant Intrinsic Carrier Mobilities in Graphene and Its Bilayer. *Physical Review Letters*, 100 (2008), 016602.
- [37] Mayorov A. S., Gorbachev R. V., Morozov S. V., Britnell L., Jalil R., Ponomarenko L. A., Blake P., Novoselov K. S., Watanabe K., Taniguchi T., and Geim A. K. Micrometer-Scale Ballistic Transport in Encapsulated Graphene at Room Temperature. *Nano Letters*, 11 (6) (2011), 2396–2399.
- [38] Chen J.-H., Jang C., Xiao S., Ishigami M., and Fuhrer M. S. Intrinsic and extrinsic performance limits of graphene devices on SiO₂. *Nature Nanotechnology*, 3 (2008), 206–209.
- [39] Du X., Skachko I., Barker A., and Andrei E. Y. Approaching ballistic transport in suspended graphene. *Nature Nanotechnology*, 3 (2008), 491–495.
- [40] Lee C., Wei X., Kysar J. W., and Hone J. Measurement of the Elastic Properties and Intrinsic Strength of Monolayer Graphene. *Science*, 321 (5887) (2008), 395–388.
- [41] Pavithra C. L. P., Sarada B. V., Rajulapati Koteswararao V. ABD Rao T. N., and Sundararajan G. A New Electrochemical Approach for the Synthesis of Copper-Graphene Nanocomposite Foils with High Hardness. *Scientific Reports*, 4 (2014), 4049.
- [42] Wang Q., Wang C., Zhang M., Jian M., and Zhang Y. Feeding Single-Walled Carbon Nanotubes or Graphene to Silkworms for Reinforced Silk Fibers. *Nano Letters*, 16 (10) (2016), 6695–6700.
- [43] Ho C. Y., Powell R. W., and Liley P. E. Thermal Conductivity of the Elements. *Journal of Physical and Chemical Reference Data*, 1 (2) (1972), 279–421.
- [44] Nika D. L., Ghosh S., Pokatilov E. P., and Balandin A. A. Lattice thermal conductivity of graphene flakes: Comparison with bulk graphite. *Applied Physics Letters*, 94 (20) (2009), 203103.
- [45] Balandin A. A., Ghosh S., Bao W., Calizo I., Teweldebrhan D., Miao F., and Lau C. N. Superior Thermal Conductivity of Single-Layer Graphene. *Nano Letters*, 8 (3) (2008), 902–907.
- [46] Jiang J.-W., Wang J.-S., and Li B. Thermal conductance of graphene and dimerite. *Physical Review B*, 79 (2009), 205418.
- [47] Elias D. C., Nair R. R., Mohiuddin T. M. G., Morozov S. V., Blake P., Halsall M. P., Ferrari A. C., Boukhvalov D. W., Katsnelson M. I., Geim A. K., and Novoselov K. S. Control of Graphene’s Properties by Reversible Hydrogenation: Evidence for Graphane. *Science*, 323 (5914) (2009), 610–613.

- [48] Bunch J. S., Verbridge S. S., Alden J. S., Van der Zande A. M., Parpia J. M., Craighead H. G., and McEuen P. L. Impermeable Atomic Membranes from Graphene Sheets. *Nano Letters*, 8 (8) (2008), 2458–2462.
- [49] Prasai D., Tuberquia J. C., Harl R. R., Jennings G. K., and Bolotin K. I. Graphene: Corrosion-Inhibiting Coating. *ACS Nano*, 6 (2) (2012), 1102–1108.
- [50] Wang X., Li X., Zhang L., Yoon Y., Weber P. K., Wang H., Guo J., and Dai H. N-Doping of Graphene Through Electrothermal Reactions with Ammonia. *Science*, 324 (5928) (2009), 768–771.
- [51] Nair R. R., Blake P., Grigorenko A. N., Novoselov K. S., Booth T. J., Stauber T., Peres N. M. R., and Geim A. K. Fine Structure Constant Defines Visual Transparency of Graphene. *Science*, 320 (5881) (2008), 1308.
- [52] Kim K. S., Zhao Y., Jang H., Lee S. Y., Kim J. M., Kim K. S., Ahn J.-H., Kim P., Choi J.-Y., and Hong B. H. Large-scale pattern growth of graphene films for stretchable transparent electrodes. *Nature*, 457 (2009), 706–710.
- [53] Wang X., Zhi L., and Müllen K. Transparent, Conductive Graphene Electrodes for Dye-Sensitized Solar Cells. *Nano Letters*, 8 (1) (2008), 323–327.
- [54] Xia F., Mueller T., Lin Y.-m., Valdes-Garcia A., and Avouris P. Ultrafast graphene photodetector. *Nature Nanotechnology*, 4 (2009), 839–843.
- [55] Novoselov K. S., Geim A. K., Morozov S. V., Jiang D., Zhang Y., Dubonos S. V., Grigorieva I. V., and Firsov A. A. Electric Field Effect in Atomically Thin Carbon Films. *Science*, 306 (5696) (2004), 666–669.
- [56] Novoselov K. S., Jiang J., Schedin F., Booth T. J., Khotkevich V. V., Morozov S. V., and Geim A. K. Two-dimensional atomic crystals. *Proceedings of the National Academy of Sciences of the United States of America*, 102 (30) (2005), 10451–10453.
- [57] Geim A. K. and Novoselov K. S. The rise of graphene. *Nature Materials*, 6 (2007), 183–191.
- [58] Inagaki M., Kim Y. A., and Endo M. Graphene: preparation and structural perfection. *Journal of Materials Chemistry*, 21 (2011), 3280–3294.
- [59] Emtsev K. V., Bostwick A., Horn K., Jobst J., Kellogg G. L., Ley L., McChesney J. L., Ohta T., Reshanov S. A., Röhrl J., Rotenberg E., Schmid A. K., Waldmann D., Weber H. B., and Seyller T. Towards wafer-size graphene layers by atmospheric pressure graphitization of silicon carbide. *Nature Materials*, 8 (2009), 203–207.
- [60] Berger C., Song Z., Li T., Li X., Ogbazghi A. Y., Feng R., Dai Z., Marchenkov A. N., Conrad E. H., First P. N., and De Heer W. A. Ultrathin Epitaxial Graphite: 2D Electron Gas Properties and a Route toward Graphene-based Nanoelectronics. *The Journal of Physical Chemistry B*, 108 (52) (2004), 19912–19916.
- [61] Avouris P. and Dimitrakopoulos C. Graphene: synthesis and applications. *materialstoday*, 15 (3) (2012), 86–97.
- [62] Rolling E., Gweon G.-H., Zhou S., Mun B., McChesney J., Hussain B., Fedorov A., First P., De Heer W., and Lanzara A. Synthesis and characterization of atomically thin graphite films on a silicon carbide substrate. *Journal of Physics and Chemistry of Solids*, 67 (9-10) (2006), 2172–2177.

- [63] Berger C., Song Z., Li X., Wu X., Brown N., Naud C., Mayou D., Li T., Hass J., Marchenkov A. N., Conrad E. H., First P. N., and De Heer W. A. Electronic Confinement and Coherence in Patterned Epitaxial Graphene. *Science*, 312 (5777) (2006), 1191–1196.
- [64] Van Bommel A., Crombeen J., and Van Tooren A. LEED and Auger electron observations of the SiC(0001) surface. *Surface Science*, 48 (2) (1975), 463–472.
- [65] Forbeaux I., Themlin J.-M., Charrier A., Thibaudau F., and Debever J.-M. Solid-state graphitization mechanisms of silicon carbide 6H-SiC polar faces. *Applied Surface Science*, 162-163 (2000), 406–412.
- [66] Sutter P. How silicon leaves the scene. *Nature Materials*, 8 (2009), 171–172.
- [67] Cambaz Z. G., Yushin G., Osswald S., Mochalin V., and Gogotsi Y. Noncatalytic synthesis of carbon nanotubes, graphene and graphite on SiC. *Carbon*, 46 (6) (2008), 841–849.
- [68] Staudenmaier L. Verfahren zur Darstellung der Graphitsäure. *European Journal of Inorganic Chemistry*, 31 (2) (1898), 1481–1487.
- [69] Hummers W. S. and Offeman R. E. Preparation of Graphitic Oxide. *Journal of the American Society*, 80 (6) (1958), 1339.
- [70] Pei S. and Cheng H.-M. The reduction of graphene oxide. *Carbon*, 50 (9) (2012), 3210–3228.
- [71] Abdolhosseinzadeh S., Asgharzadeh H., and Kim H. S. Fast and fully-scalable synthesis of reduced graphene oxide. *Scientific Reports*, 5 (2015), 10160.
- [72] Stankovich S., Dikin D. A., Dommett G. H. B., Kohlhaas K. M., Zimney E. J., Stach E. A., Piner R. D., Nguyen S. T., and Ruoff R. S. Graphene-based composite materials. *Nature*, 442 (2006), 282–286.
- [73] Xiao K., Wu H., Lv H., Wu X., and Qian H. The study of the effects of cooling conditions on high quality graphene growth by the APCVD method. *Nanoscale*, 5 (2013), 5524–5529.
- [74] Muñoz R. and Gómez-Aleixandre C. Review of CVD Synthesis of Graphene. *Chemical Vapor Deposition*, 19 (2013), 297–322.
- [75] Choubak S., Biron M., Levesque P. L., Martel R., and Desjardins P. No Graphene Etching in Purified Hydrogen. *The Journal of Physical Chemistry Letters*, 4 (7) (2013), 1100–1103.
- [76] Gan L. and Luo Z. Turning off Hydrogen To Realize Seeded Growth of Subcentimeter Single-Crystal Graphene Grains on Copper. *ACS Nano*, 7 (10) (2013), 9480–9488.
- [77] Hao Y., Bharathi M. S., Wang L., Liu Y., Chen H., Nie S., Wang X., Chou H., Tan C., Fallahzad B., Ramanarayan H., Magnuson C. W., Tutuc E., Yakobson B. I., McCarty K. F., Zhang Y.-W., Kim P., Hone J., Colombo L., and Ruoff R. S. The Role of Surface Oxygen in the Growth of Large Single-Crystal Graphene on Copper. *Science*, 342 (6159) (2013), 720–723.
- [78] Robinson Z. R., Ong E. W., Mowll T. R., Tyagi P., Gaskill D. K., Geisler H., and Ventrice C. A. Influence of Chemisorbed Oxygen on the Growth of Graphene on Cu(100) by Chemical Vapor Deposition. *The Journal of Physical Chemistry C*, 117 (45) (2013), 23919–23927.
- [79] Shin Y. C. and Kong J. Hydrogen-excluded graphene synthesis via atmospheric pressure chemical vapor deposition. *Carbon*, 59 (2013), 439–447.

- [80] Vlassioux I., Smirnov S., Regmi M., Surwade S. P., Srivastava N., Feenstra R., Eres G., Parish C., Lavrik N., Datskos P., Dai S., and Fulvio P. Graphene Nucleation Density on Copper: Fundamental Role of Background Pressure. *The Journal of Physical Chemistry C*, 117 (37) (2013), 18919–18926.
- [81] Zhang X., Ning J., Li X., Wang B., Hao L., Liang M., Jin M., and Zhi L. Hydrogen-induced effects on the CVD growth of high-quality graphene structures. *Nanoscale*, 5 (2013), 8363–8366.
- [82] Jin Y., Hu B., Wei Z., Luo Z., Wei D., Xi Y., Zhang Y., and Liu Y. Roles of H₂ in annealing and growth times of graphene CVD synthesis over copper foil. *Journal of Materials Chemistry A*, 2 (2014), 16208–162016.
- [83] Guermoune A., Charia T., Popescua F., Sabrid S. S., Guillemette J., Skulasond H. S., Szkopek T., and Siaja M. Chemical vapor deposition synthesis of graphene on copper with methanol, ethanol, and propanol precursors. *Carbon*, 49 (13) (2011), 4204–4210.
- [84] Robertson A. W. and Warner J. H. Hexagonal Single Crystal Domains of Few-Layer Graphene on Copper Foils. *Nano Letters*, 11 (3) (2011), 1182–1189.
- [85] Li X., Magnuson C. W., Venugopal A., Tromp R. M., Hannon J. B., Vogel E. M., Colombo L., and Ruoff R. S. Large-Area Graphene Single Crystals Grown by Low-Pressure Chemical Vapor Deposition of Methane on Copper. *Journal of the American Chemical Society*, 133 (2011), 2816–2819.
- [86] Levendorf M. P., Ruiz-Vargas C. S., Garg S., and Park J. Transfer-Free Batch Fabrication of Single Layer Graphene Transistors. *Nano Letters*, 9 (12) (2009), 4479–4483.
- [87] Ismach A., Druzglaski C., Penwell S., Schwartzberg A., Zheng M., Javey A., Bokor J., and Zhang Y. Direct Chemical Vapor Deposition of Graphene on Dielectric Surfaces. *Nano Letters*, 10 (5) (2010), 1542–1548.
- [88] Lee B.-J., Yu H.-Y., and Jeong G.-H. Controlled Synthesis of Monolayer Graphene Toward Transparent Flexible Conductive Film Application. *Nanoscale Research Letters*, 5 (2010), 1768–1773.
- [89] De Castro R., Araujo J., Valaski R., Costa L., Archanjo B., Fragneaud B., Cremona M., and Achete C. New transfer method of CVD-grown graphene using a flexible, transparent and conductive polyaniline-rubber thin film for organic electronic applications. *Chemical Engineering Journal*, 273 (2015), 509–518.
- [90] Na S. R., Suk J. W., Tao L., Akinwande D., Ruoff R. S., Huang R., and Liechti K. M. Selective Mechanical Transfer of Graphene from Seed Copper Foil Using Rate Effects. *ACS Nano*, 9 (2) (2015), 1325–1335.
- [91] Gao L., Ren W., Xu H., Jin L., Wang Z., Ma T., Ma L. P., Zhang Z., Fu Q., Peng L. M., Bao X., and Cheng H. M. Repeated growth and bubbling transfer of graphene with millimetre-size single-crystal grains using platinum. *Nature Communications*, 3 (2012), 699.
- [92] Kalita G., Papon R., Sharma S., Shinde S. M. S., Vishwakarma R., and Tanemura M. Transformation of chemical vapor deposited individual graphene crystal with oxidation of copper substrate. *Carbon*, 80 (2014), 504–512.
- [93] Pimenta M. A., Dresselhaus G., Dresselhaus M. S., Cançado L. G., Jorio A., and Saito R. Studying disorder in graphite-based systems by Raman spectroscopy. *Physical Chemistry Chemical Physics*, 9 (11) (2007), 1276–1290.
- [94] Klar P., Lidorikis E., Eckmann A., Verzhbitskiy I. A., Ferrari A. C., and Casiraghi C. Raman scattering efficiency of graphene. *Physical Review B*, 87 (2013), 205435.

- [95] Wang Y. Y., Ni Z., Yu T., Shen Z., Wang H., Wu Y., Chen W., and Wee A. T. S. W. Raman Studies of Monolayer Graphene: The Substrate Effect. *The Journal of Physical Chemistry C*, 112 (29) (2008), 10637–10640.
- [96] Graf D., Molitor F., Ensslin K., Stampfer C., Jungen A., Hierold C., and Wirtz L. Spatially Resolved Raman Spectroscopy of Single- and Few-Layer Graphene. *Nano Letters*, 7 (2) (2007), 238–242.
- [97] Ferrari A. C., Meyer J. C., Scardaci V., Casiraghi C., Lazzeri M., Mauri F., Piscanec S., Jiang D., Novoselov K. S., Roth S., and Geim A. K. Raman Spectrum of Graphene and Graphene Layers. *Physical Review Letters*, 97 (18) (2006), 187401.
- [98] Eckmann A., Felten A., Mishchenko A., Britnell L., Krupke R., Novoselov K. S., and Casiraghi C. Probing the Nature of Defects in Graphene by Raman Spectroscopy. *Nano Letters*, 12 (8) (2012), 3925–3930.
- [99] Tuinstra F. and Koenig J. L. Raman Spectrum of Graphite. *The Journal of Chemical Physics*, 53 (3) (1970), 1126–1130.
- [100] Zhu Y., Murali S., Cai W., Li X., Suk J. W., Potts J. R., and Ruoff R. S. Graphene and Graphene Oxide: Synthesis, Properties, and Applications. *Advanced Materials*, 22 (2010), 3906–3924.
- [101] Hao Y., Wang Y., Wang L., Ni Z., Wang Z., Wang R., Koo C. K., Shen Z., and Thong J. T. L. T. Probing Layer Number and Stacking Order of Few-Layer Graphene by Raman Spectroscopy. *Small*, 6 (2) (2010), 195–200.
- [102] Luo Z., Lu Y., Singer D. W., Berck M. E., Somers L. A., Goldsmith B. R., and Johnson A. T. C. Effect of Substrate Roughness and Feedstock Concentration on Growth of Wafer-Scale Graphene at Atmospheric Pressure. *Chemistry of Materials*, 23 (2011), 1441–1447.
- [103] Chung T. F., Shen T., Cao H., Jauregui L. A., Wu W., Yu Q., Newell D., and Chen Y. P. Synthetic Graphene Grown by Chemical Vapor Deposition on Copper Foils. *International Journal of Modern Physics B*, 27 (10) (2013), 1341002.
- [104] Vlasiouk I., Fulvio P., Meyer H., Lavrik N., Dai S., Datskos P., and Smirnov S. Large scale atmospheric pressure chemical vapor deposition of graphene. *Carbon*, 54 (2013), 58–67.
- [105] Sharma S., Kalita G., Hirano R., Maruti S. S., Papon R., Ohtani H., and Tanemura M. Synthesis of graphene crystals from solid waste plastic by chemical vapor deposition. *Carbon*, 72 (2014), 66–73.
- [106] Wu T., Zhang X., Yuan Q., Xue J., Lu G., Liu Z., Wang H., Wang H., Ding F., Yu Q., Xie X., and Jiang M. Fast growth of inch-sized single-crystalline graphene from a controlled single nucleus on Cu–Ni alloys. *Nature Materials*, 15 (2015), 43–47.
- [107] Wang H., Wang G., Bao P., Yang S., Zhu W., Xie X., and Zhang W. J. Controllable synthesis of submillimeter single-crystal monolayer graphene domains on copper foils by suppressing nucleation. *Journal of the American Chemical Society*, 134 (8) (2012), 3627–3630.
- [108] Yan Z., Lin J., Peng Z., Sun Z., Zhu Y., Li L., Xiang C., Samuel E. L., Kittrell C., and Tour J. M. Toward the Synthesis of Wafer-Scale Single-Crystal Graphene on Copper Foils. *ACS Nano*, 6 (10) (2012), 9110–9117.
- [109] Wu W., Jauregui L. A., Su Z., Liu Z., Bao J., Chen Y. P., and Yu Q. Growth of single crystal graphene arrays by locally controlling nucleation on polycrystalline Cu using chemical vapor deposition. *Advanced Materials*, 23 (2011), 4898–4903.

- [110] Hwang C., Yoo K., Kim S. J., Seo E. K., Yu H., and Biro L. P. Initial Stage of Graphene Growth on a Cu Substrate. *Journal of Physical Chemistry C*, 115 (2011), 22369–22374.
- [111] Wood J. D., Schmucker S. W., Lyons A. S., Pop E., and Lyding J. W. Effects of Polycrystalline Cu Substrate on Graphene Growth by Chemical Vapor Deposition. *Nano Letters*, 11 (11) (2011), 4547–4554.
- [112] Ago H., Ogawa Y., Tsuji M., Mizuno S., and Hibino H. Catalytic Growth of Graphene: Toward Large-Area Single-Crystalline Graphene. *The Journal of Physical Chemistry Letters*, 3 (16) (2012), 2228–2236.
- [113] Geng D., Wu B., Guo Y., Huang L., Xue Y., Chen J., Yu G., Jiang L., Hu W., and Liu Y. Uniform hexagonal graphene flakes and films grown on liquid copper surface. *Proceedings of the National Academy of Sciences of the United States of America*, 109 (21) (2012), 7992–7996.
- [114] Kidambi P. R., Ducati C., Dlubak B., Gardiner D., Weatherup R. S., Martin M.-B., Seneor P., Coles H., and Hofmann S. The Parameter Space of Graphene Chemical Vapor Deposition on Polycrystalline Cu. *The Journal of Physical Chemistry C*, 116 (42) (2012), 22492–22501.
- [115] Wang C., Chen W., Han C., Wang G., Tang B., Tang C., Wang Y., Zou W., Chen W., Zhang X.-A., Qin S., Chang S., and Wang L. Growth of Millimeter-Size Single Crystal Graphene on Cu Foils by Circumfluence Chemical Vapor Deposition. *Scientific Reports*, 4 (2014), 4537.
- [116] Abanin D. A. and Levitov L. S. Conformal invariance and shape-dependent conductance of graphene samples. *Physical Review B*, 78 (3) (2008), 035416.
- [117] Yazyev O. V. and Louie S. G. Electronic transport in polycrystalline graphene. *Nature Materials*, 9 (2010), 806–809.
- [118] Yazyev O. V. and Louie S. G. Topological defects in graphene: Dislocations and grain boundaries. *Physical Review B*, 81 (2010), 195420.
- [119] Wu B., Geng D., Guo Y., Huang L., Xue Y., Zheng J., Chen J., Yu G., Liu Y., Jiang L., and Hu W. Equiangular hexagon-shape-controlled synthesis of graphene on copper surface. *Advanced Material*, 23 (31) (2011), 3522–3525.
- [120] Wu T., Ding G., Shen H., Wang H., Sun L., Jiang D., Xie X., and Jiang M. Triggering the Continuous Growth of Graphene Toward Millimeter-Sized Grains. *Advanced Functional Materials*, 23 (2012), 198–203.
- [121] Mohsin A., Liu L., Liu P., Deng W., Ivanov I. N., Li G., Dyck O. E., Duscher G., Dunlap J. R., Xiao K., and Gu G. Synthesis of Millimeter-Size Hexagon-Shaped Graphene Single Crystals on Resolidified Copper. *ACS Nano*, 7 (10) (2013), 8924–8931.
- [122] Zhang Y. H., Chen Z. Y., Wang B., Wu Y. W., Jin Z., Liu X. Y., and Yu G. H. Controllable growth of millimeter-size graphene domains on Cu foil. *Materials Letters*, 96 (2013), 149–151.
- [123] Ma T., Ren W., Liu Z., Huang L., Ma L.-P., Ma X., Zhang Z., Peng L.-M., and Cheng H.-M. Repeated Growth–Etching–Regrowth for Large-Area Defect-Free Single-Crystal Graphene by Chemical Vapor Deposition. *ACS Nano*, 8 (12) (2014), 12806–12813.
- [124] Lin L., Li J., Ren H., Koh A. L., Kang N., Peng H., Xu H. Q., and Liu Z. Surface Engineering of Copper Foils for Growing Centimeter-Sized Single-Crystalline Graphene. *ACS Nano*, 10 (2) (2016), 2922–2929.

- [125] Li X., Cai W., An J., Kim S., Nah J., Yang D., Piner R., Velamakanni A., Jung I., Tutuc E., Banerjee S. K., Colombo L., and Ruoff R. S. Large-Area Synthesis of High-Quality and Uniform Graphene Films on Copper Foils. *Science*, 324 (5932) (2009), 1312–1314.
- [126] Zhou H., Yu W. J., Liu L., Cheng R., Chen Y., Huang X., Liu Y., Wang Y., Huang Y., and Duan X. Chemical vapour deposition growth of large single crystals of monolayer and bilayer graphene. *Nature Communications*, 4 (2013), 2096.
- [127] Kalita G., Matsushima M., Uchida H., Wakita K., and Umeno M. Few layers of graphene as transparent electrode from botanical derivative camphor. *Materials Letters*, 64 (20) (2010), 2180–2183.
- [128] Sun Z., Yan Z., Yao J., Beitler E., Zhu Y., and Tour J. M. Growth of graphene from solid carbon sources. *Nature*, 468 (7323) (2010), 549–552.
- [129] Ruan G., Sun Z., Peng Z., and Tour J. M. Growth of Graphene from Food, Insects, and Waste. *ACS Nano*, 5 (9) (2011), 7601–7607.
- [130] Perez C. C., Pena J. M., and Duarte-Correia C. R. Improved synthesis of bioactive stilbene derivatives applying design of experiments to the Heck–Matsuda reaction. *New Journal of Chemistry*, 38 (2014), 3933–3938.
- [131] Schedin F., Geim A. K., Morozov S. V., Hill E. W., Blake P., Katsnelson M. I., and Novoselov K. S. Detection of individual gas molecules adsorbed on graphene. *Nature Materials*, 6 (2007), 652–657.
- [132] Britnell L., Gorbachev R., Jalil R., Belle B., Schedin F., Mishchenko A., Georgiou T., Katsnelson M., Eaves L., Morozov S., Peres N., Leist J., Geim A., Novoselov K., and Ponomarenko L. Field-effect tunneling transistor based on vertical graphene heterostructures. *Science*, 335 (6071) (2012), 947–950.
- [133] Novoselov K. S., Fal'ko V. I., Colombo L., Gellert P. R., Schwab M. G., and Kim K. A roadmap for graphene. *Nature*, 490 (2012), 192–200.
- [134] Lee S., Lee K., and Zhong Z. Wafer Scale Homogeneous Bilayer Graphene Films by Chemical Vapor Deposition. *Nano Letters*, 10 (11) (2010), 4702–4707.
- [135] Zhang Y., Tang T. T., Girit C., Hao Z., Martin M. C., Zettl A., Crommie M. F., Shen Y. R., and Wang F. Direct observation of a widely tunable bandgap in bilayer graphene. *Nature*, 459 (2009), 820–823.
- [136] Ohta T., Bostwick A., Seyller T., Horn K., and Rotenberg E. Controlling the Electronic Structure of Bilayer Graphene. *Science*, 313 (5789) (2006), 951–954.
- [137] Mak K. F., Lui C. H., Shan J., and Heinz T. F. Observation of an Electric-Field-Induced Band Gap in Bilayer Graphene by Infrared Spectroscopy. *Physical Review Letters*, 102 (2009), 256405.
- [138] Tapasztó L., Dobrik G., Lambin P., and Biró L. P. Tailoring the atomic structure of graphene nanoribbons by scanning tunnelling microscope lithography. *Nature Nanotechnology*, 3 (2008), 397–401.
- [139] Nakada K., Fujita M., Dresselhaus G., and Dresselhaus M. S. Edge state in graphene ribbons: Nanometer size effect and edge shape dependence. *Physical Review Letters*, 54 (24) (1996), 17954.
- [140] Han M. Y., Özyilmaz B., Zhang Y., and Kim P. Energy Band-Gap Engineering of Graphene Nanoribbons. *Physical Review Letters*, 98 (20) (2007), 206805.
- [141] Lin Y.-M., Perebeinos V., Chen Z., and Avouris P. Electrical observation of subband formation in graphene nanoribbons. *Physical Review B*, 78 (2008), 161409(R).

- [142] Ma L., Wang J., and Ding F. Recent Progress and Challenges in Graphene Nanoribbon Synthesis. *Chemical Physics and Physical Chemistry*, 14 (2012), 47–54.
- [143] Son Y.-W., Cohen M. L., and Louie S. G. Energy Gaps in Graphene Nanoribbons. *Physical Review Letters*, 97 (21) (2006), 216803.
- [144] Son Y.-W., Cohen M. L., and Louie S. G. Half-metallic graphene nanoribbons. *Nature*, 444 (2006), 347–349.
- [145] Chen Z., Lin Y.-M., Rooks M. J., and Avouris P. Graphene Nano-Ribbon Electronics. *Physica E: Low-dimensional Systems and Nanostructures*, 40 (2) (2007), 228–232.
- [146] Ritter K. A. and Lyding J. W. The influence of edge structure on the electronic properties of graphene quantum dots and nanoribbons. *Nature Materials*, 8 (2009), 235–242.
- [147] Tour J. M. Top-Down versus Bottom-Up Fabrication of Graphene-Based Electronics. *Chemistry of Materials*, 26 (1) (2014), 163–171.
- [148] Cai J., Ruffieux P., Jaafar R., Bieri M., Braun T., Blankenburg S., Muoth M., Seitsonen A. P., Saleh M., Feng X., Müllen K., and Fasel R. Atomically precise bottom-up fabrication of graphene nanoribbons. *Nature*, 466 (2010), 470–473.
- [149] Nguyen G. D., Toma F. M., Cao T., Pedramrazi Z., Chen C., Rizzo D. J., Joshi T., Bronner C., Chen Y.-C., Favaro M., Louie S. G., Fischer F. R., and Crommie M. F. Bottom-Up Synthesis of N = 13 Sulfur-Doped Graphene Nanoribbons. *Journal of Physical Chemistry C*, 120 (5) (2016), 2684–2687.
- [150] Cloke R. R., Marangoni T., Nguyen G. D., Joshi T., Rizzo D. J., Bronner C., Cao T., Louie S. G., Crommie M. F., and Fischer F. R. Site-Specific Substitutional Boron Doping of Semiconducting Armchair Graphene Nanoribbons. *Journal of the American Chemical Society*, 137 (28) (2015), 8872–8875.
- [151] Li X., Wang X., Zhang L., Lee S., and Dai H. Chemically derived, ultrasmooth graphene nanoribbon semiconductors. *Science*, 319 (5867) (2008), 1229–1232.
- [152] Jiao L., Zhang L., Wang X., Diankov G., and Dai H. Narrow graphene nanoribbons from carbon nanotubes. *Nature*, 458 (2009), 877–880.
- [153] Jiao L., Wang X., Diankov G., Wang H., and Dai H. Facile synthesis of high-quality graphene nanoribbons. *Nature Nanotechnology*, 5 (2010), 321–325.
- [154] Kosynkin D. V., Higginbotham A. L., Sinitskii A., Lomeda J. R., Dimiev A., Price B. K., and Tour J. M. Longitudinal unzipping of carbon nanotubes to form graphene nanoribbons. *Nature*, 458 (2009), 872–876.
- [155] Wang X. and Dai H. Etching and narrowing of graphene from the edges. *Nature Chemistry*, 2 (2010), 661–665.
- [156] Campos L. C., Manfrinato V. R., Sanchez-Yamagishi J. D., Kong J., and Jarillo-Herrero P. Anisotropic Etching and Nanoribbon Formation in Single-Layer Graphene. *Nano Letters*, 9 (7) (2009), 2600–2604.
- [157] Solís-Fernández P., Yoshida K., Ogawa Y., Tsuji M., and Ago H. Dense Arrays of Highly Aligned Graphene Nanoribbons Produced by Substrate-Controlled Metal-Assisted Etching of Graphene. *Advanced Materials*, 25 (2013), 6562–6268.
- [158] Elías A. L., Botello-Méndez A. R., Meneses-Rodríguez D., González V. J., Ramírez-González D., Ci L., Muñoz-Sandoval E., Ajayan P. M., Terrones H., and Terrones M. Longitudinal Cutting of Pure and Doped Carbon Nanotubes to Form Graphitic Nanoribbons Using Metal Clusters as Nanoscalpels. *Nano Letters*, 10 (2) (2010), 366–372.

- [159] Ni G.-X., Zheng Y., Bae S., Kim H. R., Pachoud A., Kim Y. S., Tan C.-L., Im D., Ahn J.-H., Hong B. H., and Özyilmaz B. Quasi-Periodic Nanoripples in Graphene Grown by Chemical Vapor Deposition and Its Impact on Charge Transport. *ACS Nano*, 6 (2) (2012), 1158–1164.
- [160] Gao H., Song L., Guo W., Huang L., Yang D., Wang F., Zuo Y., Fan X., Liu Z., Gao W., Vajtai R., Hackenberg K., and Ajayan P. M. A simple method to synthesize continuous large area nitrogen-doped graphene. *Carbon*, 50 (12) (2012), 4476–4482.
- [161] Terasawa T.-o. and Saiki K. Synthesis of Nitrogen-Doped Graphene by Plasma-Enhanced Chemical Vapor Deposition. *Japanese Journal of Applied Physics*, 51 (2012), 055101.
- [162] Wang H., Maiyalagan T., and Wang X. Review on Recent Progress in Nitrogen-Doped Graphene: Synthesis, Characterization, and Its Potential Applications. *ACS Catalysis*, 2 (5) (2012), 781–794.
- [163] Xue Y., Wu B., Jiang L., Guo Y., Huang L., Chen J., Tan J., Geng D., Luo B., Hu W., Yu G., and Liu Y. Low Temperature Growth of Highly Nitrogen-Doped Single Crystal Graphene Arrays by Chemical Vapor Deposition. *Journal of the American Chemical Society*, 134 (27) (2012), 11060–11063.
- [164] Rani P. and Jindal V. K. Designing band gap of graphene by B and N dopant atoms. *RSC Advances*, 3 (2013), 802–812.
- [165] Wang X., Sun G., Routh P., Kim D.-H., Huang W., and Chen P. Heteroatom-doped graphene materials: syntheses, properties and applications. *Chemical Society Reviews*, 43 (2014), 7067–7098.
- [166] Kondo T., Guo D., Shikano T., Suzuki T., Sakurai M., Okada S., and Nakamura J. Observation of Landau levels on nitrogen-doped flat graphite surfaces without external magnetic fields. *Scientific Reports*, 5 (2015), 16412.
- [167] Tian Y. H., Huang J., Sheng X., Sumpter B. G., Yoon M., and Kertesz M. Nitrogen Doping Enables Covalent-Like - Bonding between Graphenes. *Nano Letters*, 15 (8) (2015), 5482–5491.
- [168] Regmi M., Chisholm M. F., and Eres G. The effect of growth parameters on the intrinsic properties of large-area single layer graphene grown by chemical vapor deposition on Cu. *Carbon*, 50 (2012), 134–141.
- [169] Humphreys F. and Hatherly M. *Recrystallization and Related Annealing Phenomena*. Second Edition. Elsevier, 1995. URL: <http://www.sciencedirect.com/science/book/9780080441641>.
- [170] Cho J., Gao L., Tian J., Cao H., Wu W., Yu Q., Yitamben E. N., Fisher B., Guest J. R., Chen Y. P., and Guisinger N. P. Atomic-Scale Investigation of Graphene Grown on Cu Foil and the Effects of Thermal Annealing. *ACS Nano*, 5 (5) (2011), 3607–3613.
- [171] Choubak S., Levesque P. L., Gaufres E., Biron M., Desjardins P., and Martel R. Graphene CVD: Interplay Between Growth and Etching on Morphology and Stacking by Hydrogen and Oxidizing Impurities. *The Journal of Physical Chemistry C*, 118 (37) (2014), 21532–21540.
- [172] Strudwick A. J., Weber N. E., Schwab M. G., Kettner M., Weitz R. T., Wünsch J. R., Müllen K., and Sachdev H. Chemical Vapor Deposition of High Quality Graphene Films from Carbon Dioxide Atmospheres. *ACS Nano*, 9 (1) (2014), 31–42.

- [173] Zhang H., Zhang Y., Zhang Y., Chen Z., Sui Y., Ge X., Deng R., Yu G., Jin Z., and Liu X. Realizing controllable graphene nucleation by regulating the competition of hydrogen and oxygen during chemical vapor deposition heating. *Physical Chemistry Chemical Physics*, 18 (2013), 23638–23642.
- [174] Kraus J., Böbel M., and Günther S. Suppressing graphene nucleation during CVD on polycrystalline Cu by controlling the carbon content of the support foils. *Carbon*, 96 (2016), 153–165.
- [175] Vlasiouk I., Regmi M., Fulvio P., Dai S., Datskos P., Eres G., and Smirnov S. Role of Hydrogen in Chemical Vapor Deposition Growth of Large Single-Crystal Graphene. *ACS Nano*, 5 (7) (2011), 6069–6076.
- [176] Losurdo M. L., Giangregorio M. M., Capezzuto P., and Bruno G. Graphene CVD growth on copper and nickel: role of hydrogen in kinetics and structure. *Physical Chemistry Chemical Physics*, 13 (2011), 20836–20843.
- [177] Liu W., Li H., Xu C., Khatami Y., and Banerjee K. Synthesis of high-quality monolayer and bilayer graphene on copper using chemical vapor deposition. *Carbon*, 49 (13) (2011), 4122–4130.
- [178] Jung D. H., Kang C., Kim M., Cheong H., Lee H., and Lee J. S. Effects of Hydrogen Partial Pressure in the Annealing Process on Graphene Growth. *The Journal of Physical Chemistry C*, 118 (7) (2014), 3574–3580.
- [179] Luo B., Chen B., Meng L., Geng D., Liu H., Xu J., Zhang Z., Zhang H., Peng L., He L., Liu Y., and Yu G. Layer-stacking growth and electrical transport of hierarchical graphene architectures. *Advanced Materials*, 26 (20) (2014), 3218–3224.
- [180] Zhang X., Wang L., Xin J., Yakobson B. I., and Ding F. Role of Hydrogen in Graphene Chemical Vapor Deposition Growth on a Copper Surface. *Journal of the American Chemical Society*, 136 (8) (2014), 3040–3047.
- [181] Ji H., Hao Y., Ren Y., Charlton M., Lee W. H., Wu Q., Li H., Zhu Y., Wu Y., Piner R., and Ruoff R. S. Graphene Growth Using a Solid Carbon Feedstock and Hydrogen. *ACS Nano*, 5 (9) (2011), 7656–7661.
- [182] John R., Ashokreddy A., Vijayan C., and Pradeep T. Single- and few-layer graphene growth on stainless steel substrates by direct thermal chemical vapor deposition. *Nanotechnology*, 22 (16) (2011), 165701.
- [183] Cho H., Lee C., Oh I. S., Park S., Kim H. C., and Kim M. J. Parametric Study of Methanol Chemical Vapor Deposition Growth for Graphene. *Carbon Letters*, 13 (4) (2012), 205–211.
- [184] Zhang B., Lee W. H., Piner R., Kholmanov I., Wu Y., Li H., Ji H., and Ruoff R. S. Low-Temperature Chemical Vapor Deposition Growth of Graphene from Toluene on Electropolished Copper Foils. *ACS Nano*, 6 (3) (2012), 2471–2476.
- [185] Wu T., Ding G., Shen H., Wang H., Sun L., Zhu Y., Jiang D., and Xie X. Continuous graphene films synthesized at low temperatures by introducing coronene as nucleation seeds. *Nanoscale*, 5 (2013), 5456–5461.
- [186] Somekh M., Shawat E., and Nessim G. D. Fully reproducible, low-temperature synthesis of high-quality, few-layer graphene on nickel via preheating of gas precursors using atmospheric pressure chemical vapor deposition. *Journal of Materials Chemistry A*, 2 (2014), 19750–19758.

- [187] Santangelo S., Messina G., Malara A., Lisi N., Dikonimos T., Capasso A., Ortolani L., Morandi V., and Faggio G. Taguchi optimized synthesis of graphene films by copper catalyzed ethanol decomposition. *Diamond and Related Materials*, 41 (2014), 73–78.
- [188] Jang J., Son M., Chung S., Kim K., Cho C., Lee B. H., and Ham M.-H. Low-temperature-grown continuous graphene films from benzene by chemical vapor deposition at ambient pressure. *Scientific Reports*, 5 (2015), 17955.
- [189] Luo Y.-R. *Comprehensive Handbook of chemical bond energies*. CRC Press, Taylor and Francis group, 2007. URL: <http://www.crcnetbase.com/isbn/978-0-8493-7366-4>.
- [190] Srinivasan C. and Saraswathi R. Growing high-quality graphene from incredible solid materials. *Current Science*, 102 (1) (2012).
- [191] Andrews R. J., Smith C. F., and Alexander A. J. Mechanism of carbon nanotube growth from camphor and camphor analogs by chemical vapor deposition. *Carbon*, 44 (2) (2006), 341–347.
- [192] Kumar M. and Ando Y. Chemical Vapor Deposition of Carbon Nanotubes: A Review on Growth Mechanism and Mass Production. *Journal of Nanoscience and Nanotechnology*, 10 (2010), 3739–3758.
- [193] Sharma S., Kalita G., Ayhan M. E., Wakita K., Umeno M., and Tanemura M. Synthesis of hexagonal graphene on polycrystalline Cu foil from solid camphor by atmospheric pressure chemical vapor deposition. *Journal of Materials Science*, 48 (2013), 7036–7041.
- [194] Ravani F., Papagelis K., Dracopoulos V., Parthenios J., Dassios K. G., Siokou A., and Galiotis C. Graphene production by dissociation of camphor molecules on nickel substrate. *Thin Solid Films*, 527 (2013), 31–37.
- [195] Organization I. L. *International Chemical Safety Cards*. International Labor Organization. 2016. URL: http://www.ilo.org/safework/info/publications/WCMS_113134/lang-en/index.htm.
- [196] Papon R., Kalita G., Sharma S., Shinde S. M., Vishwakarma R., and Tanemura M. Controlling single and few-layer graphene crystals growth in a solid carbon source based chemical vapor deposition. *Applied Physics Letters*, 105 (13) (2014), 133103.
- [197] Papon R., Sharma S., Shinde S. M., Thangaraja A., Kalita G., and Tanemura M. Formation of graphene nanoribbons and Y-junctions by hydrogen induced anisotropic etching. *RSC Advances*, 5 (2015), 35297–35301.
- [198] Wang Z., Li P., Chen Y., Liu J., Tian H., Zhou J., Zhanga W., and Lia Y. Synthesis of nitrogen-doped graphene by chemical vapour deposition using melamine as the sole solid source of carbon and nitrogen. *Journal of Materials Chemistry C*, 2 (2014), 7396–7401.
- [199] Shinde S. M., Kano E., Kalita G., Takeguchi M., Hashimoto A., and Tanemura M. Grain structures of nitrogen-doped graphene synthesized by solid source-based chemical vapor deposition. *Carbon*, 96 (2016), 448–453.
- [200] W. M. Haynes, ed. *CRC Handbook of Chemistry and Physics*. 96th Edition. CRC Press, 2015-2016. URL: <https://www.crcpress.com/CRC-Handbook-of-Chemistry-and-Physics-96th-Edition/Haynes/p/book/9781482260977>.
- [201] Seah C.-M., Chai S.-P., and Mohamed A. R. Mechanisms of graphene growth by chemical vapour deposition on transition metals. *Carbon*, 70 (2014), 1–21.
- [202] Coraux J., N'Diaye A. T., Engler M., Busse C., Wall D., Buckanie N., Heringdorf F.-J. meyer zu, Van Gastel R., Poelsema B., and Michely T. Growth of graphene on Ir(111). *New Journal of Physics*, 11 (2009), 023006.

- [203] Saadi S., Abild-Pedersen F., Helveg S., Sehested J., Hinnermann B., Appel C. C., and Nørskov J. K. On the Role of Metal Step-Edges in Graphene Growth. *The Journal of Physical Chemistry C*, 114 (25) (2010), 11221–11227.
- [204] Tan L., Zeng M., Zhang T., and Fu L. Design of catalytic substrates for uniform graphene films: from solid-metal to liquid-metal. *Nanoscale*, 7 (2015), 9105–9121.
- [205] Robinson Z. R., Tyagi P., Murray T. M., Ventrice C. A. J., Chen S., Munson A., Magnuson C. W., and Ruoff R. S. Substrate grain size and orientation of Cu and Cu–Ni foils used for the growth of graphene films. *Journal of Vacuum Science & Technology A*, 30 (1) (2012), 011401.
- [206] Chen H., Zhu W., and Zhang Z. Contrasting Behavior of Carbon Nucleation in the Initial Stages of Graphene Epitaxial Growth on Stepped Metal Surfaces. *Physical Review Letters*, 104 (18) (2009), 186101.
- [207] Gao L., Guest J. R., and Guisinger N. P. Epitaxial Graphene on Cu(111). *Nano Letters*, 10 (2010), 3512–3516.
- [208] Gao J., Yip J., Zhao J., Yakobson B. I., and Ding F. Graphene Nucleation on Transition Metal Surface: Structure Transformation and Role of the Metal Step Edge. *Journal of the American Chemical Society*, 133 (13) (2011), 5009–5015.
- [209] Ma L. P., Ren W. C., Dong Z. L., Liu L. Q., and Cheng H. M. Progress of graphene growth on copper by chemical vapor deposition: Growth behavior and controlled synthesis. *Chinese Science Bulletin*, 57 (23) (2012), 2995–2999.
- [210] Frank O., Vejpravova J., Holy V., Kavan L., and Kalbac M. Interaction between graphene and copper substrate: The role of lattice orientation. *Carbon*, 68 (2014), 440–451.
- [211] Thompson C. V. and Carel R. Stress and grain growth in thin films. *Journal of the Mechanics and Physics of Solids*, 44 (5) (1996), 657–673.
- [212] Mattevi C., Kim H., and Chhowalla M. A review of chemical vapour deposition of graphene on copper. *Journal of Materials Chemistry*, 21 (2011), 3324–3334.
- [213] Kittel C. *Introduction to Solid State Physics*. 8th Edition. John Wiley & Sons, Inc, 2005. URL: <https://archive.org/stream/IntroductionToSolidStatePhysics/81060415-Introduction-to-Solid-State-Physics-8th-Edition-by-Charles-Kittel#page/n0/mode/2up>.
- [214] Li X., Cai W., Colombo L., and Ruoff R. S. Evolution of Graphene Growth on Ni and Cu by Carbon Isotope Labeling. *Nano Letters*, 9 (12) (2009), 4268–4272.
- [215] Lahiri J., Miller T. S., Ross A. J., Adamska L., Oleynik I. I., and Batzill M. Graphene growth and stability at nickel surfaces. *New Journal of Physics*, 13 (2011), 025001.
- [216] Baraton L., He Z. B., Lee C. S., Cojocaru C. S., Chatelet M., Maurice J.-L., Lee Y. H., and Pribat D. On the mechanisms of precipitation of graphene on nickel thin films. *Materials Science*, 96 (4) (2011), 46003.
- [217] Zakar E., Nichols B. M., Kilpatrick S., Meissner G., Fu R., and Hauri K. Nucleation Sites for Multilayer Graphene on Nickel Catalyst. *2011 11th IEEE International Conference on Nanotechnology*. 2011, 1516–1520.
- [218] Bao J. F., Kishi N., and Soga T. Synthesis of nitrogen-doped graphene by the thermal chemical vapor deposition method from a single liquid precursor. *Materials Letters*, 177 (2014), 199–203.
- [219] Reina A., Jia X., Ho J., Nezich D., Son H., Bulovic V., Dresselhaus M. S., and Kong J. Large Area, Few-Layer Graphene Films on Arbitrary Substrates by Chemical Vapor Deposition. *Nano Letters*, 9 (1) (2009), 30–35.

- [220] Yu Q., Lian J., Siriponglert S., Li H., Chen Y. P., and Pei S.-S. Graphene segregated on Ni surfaces and transferred to insulators. *Applied Physics Letters*, 93 (11) (2008), 113103.
- [221] López G. and Mittemeijer E. The solubility of C in solid Cu. *Scripta Materialia*, 51 (1) (2004), 1–5.
- [222] Bhaviripudi S., Jia X., Dresselhaus M. S., and Kong J. Role of Kinetic Factors in Chemical Vapor Deposition Synthesis of Uniform Large Area Graphene Using Copper Catalyst. *Nano Letters*, 10 (2010), 4128–4133.
- [223] Nie S., Wofford J. M., Bartelt N. C., Dubon O. D., and McCarty K. F. Origin of the mosaicity in graphene grown on Cu(111). *Physical Review B*, 84 (15) (2011), 155425.
- [224] Wang Z.-J., Weinberg G., Zhang Q., Lunkenbein T., Klein-Hoffmann A., Kurnatowska M., Plodinec M., Li Q., Chi L., Schloegl R., and Willinger M.-G. Direct Observation of Graphene Growth and Associated Copper Substrate Dynamics by in Situ Scanning Electron Microscopy. *ACS Nano*, 9 (2) (2015), 1506–1519.
- [225] Loginova E., Bartelt N. C., Feibelman P. J., and McCarty K. F. Evidence for graphene growth by C cluster attachment. *New Journal of Physics*, 10 (2008), 093026.
- [226] Kim H. K., Mattevi C., Calvo M. R., Oberg J. C., Artiglia L., Agnoli S., Hirjibehedin C. F., Chhowalla M., and Saiz E. Activation Energy Paths for Graphene Nucleation and Growth on Cu. *ACS Nano*, 6 (4) (2012), 3614–3623.
- [227] Han G. H., Güneş F., Bae J. J., Kim E. S., Chae S. J., Shin H.-J., Choi J.-Y., Pribat D., and Lee Y. H. Influence of Copper Morphology in Forming Nucleation Seeds for Graphene Growth. *Nano Letters*, 11 (10) (2011), 4144–4148.
- [228] Zhang H., Zhang Y., Wang B., Chen Z., Sui Y., Zhang Y., Tang C., Zhu B., Xie X., Yu G., Jin Z., and Liu X. Effect of Hydrogen in Size-Limited Growth of Graphene by Atmospheric Pressure Chemical Vapor Deposition. *Journal of Electronic Materials*, 44 (1) (2015), 79–86.
- [229] Wofford J. M., Nie S., McCarty K. F., Bartelt N. C., and Dubon O. D. Graphene Islands on Cu Foils: The Interplay between Shape, Orientation, and Defects. *Nano Letters*, 10 (12) (2010), 4890–4896.
- [230] Yu V., Whiteway E., Maassen J., and Hilke M. Straining Graphene by Chemical Vapour Deposition Growth on Copper. *Physical Review B*, 84 (2011), 205407.
- [231] Choi D. S., Kim K. S., Kim H., Kim Y., Kim T., Rhy S.-h., Yang C.-M., Yoon D. H., and Yang W. S. Effect of Cooling Condition on Chemical Vapor Deposition Synthesis of Graphene on Copper Catalyst. *Applied Materials and Interfaces*, 6 (22) (2014), 19574–19578.
- [232] Wu B., Geng D., Xu Z., Guo Y., Huang L., Xue Y., Chen J., Yu G., and Liu Y. Self-organized graphene crystal patterns. *NPG Asia Materials*, 5 (2013), e36.
- [233] Xiao Y., Kim H., Mattevi C., Chhowalla M., Maher R. C., and Cohena L. F. Influence of Cu substrate topography on the growth morphology of chemical vapour deposited graphene. *Carbon*, 65 (2013), 7–12.
- [234] Chen S., Cai W., Piner R. D., Suk J. W., Wu Y., Ren Y., Kang J., and Ruoff R. S. Synthesis and Characterization of Large-Area Graphene and Graphite Films on Commercial Cu–Ni Alloy Foils. *Nano Letters*, 11 (9) (2011), 3519–3525.
- [235] Wu Y., Chou H., Ji H., Wu Q., Chen S., Jiang W., Hao Y., Kang J., Ren Y., Piner R. D., and Ruoff R. S. Growth Mechanism and Controlled Synthesis of AB-Stacked Bilayer Graphene on Cu–Ni Alloy Foils. *ACS Nano*, 6 (9) (2012), 7731–7738.

- [236] An Mey S. Thermodynamic re-evaluation of the Cu-Ni system. *Calphad*, 16 (3) (1992), 255–260.
- [237] Yang R., Goethel P., Schwartz J., and Lund C. Solubility and diffusivity of carbon in metals. *Journal of Catalysis*, 122 (1) (1990), 206–210.
- [238] Grigorenko G. M. and Pomarin Y. M. *Nitrogen and hydrogen in molten metals and alloys*. Vol. 1, part 6. Harwood Academic Publishers GmbH, 1990.
- [239] Goldschmidt H. J. *Interstitial alloys*. Plenum Press, Butterworth & Co, 1967.
- [240] Hu X., Björkman T., Lipsanen H., Sun L., and Krasheninnikov A. V. Solubility of Boron, Carbon, and Nitrogen in Transition Metals: Getting Insight into Trends from First-Principles Calculations. *Journal of Physical Chemistry Letters*, 6 (16) (2015), 3263–3268.
- [241] Abdulrahman R. and Hendry A. Solubility of nitrogen in liquid nickel-based alloys. *Metallurgical and Materials Transactions B*, 32 (6) (2001), 1103–1112.
- [242] Maiti M., Srivastava V. K., Shewale S., Jasra R. V., Chavda A., and Modi S. M. Process parameter optimization through Design of Experiments in synthesis of high cis-polybutadiene rubber. *Chemical Engineering Science*, 107 (2014), 256–265.
- [243] Cichocki A. and Koscielniak P. Experimental designs applied to hydrothermal synthesis of zeolite ERI+OFF(T) in the Na₂O–K₂O–Al₂O₃–SiO₂–H₂O system Part 2. Regular study. *Microporous and Mesoporous Materials*, 29 (3) (1999), 369–382.
- [244] Taniguchi G. *System of experimental design: engineering methods to optimize quality and minimize costs*. UNIPUB/Kraus International Publications, 1987. URL: https://books.google.co.jp/books/about/System_of_experimental_design.html?id=PVQAAAAMAAJ&redir_esc=y.
- [245] Su D., Ren M., Li X. a., and Huang W. Synthesis of graphene by chemical vapor deposition: effect of growth conditions. *Journal of Nanoscience and Nanotechnology*, 13 (10) (2013), 6471–6484.
- [246] Park K. T., Kim T., and Park C. R. Overlook of current chemical vapor deposition-grown large single-crystal graphene domains. *Carbon Letters*, 15 (3) (2014), 151–161.
- [247] Page A. J. P., Mitchell I., Li H.-B., Wang Y., Jiao M.-g., Irle S., and Morokuma K. Spanning the “Parameter Space” of Chemical Vapor Deposition Graphene Growth with Quantum Chemical Simulations. *The Journal of Physical Chemistry C*, 120 (2016), 13851–13864.
- [248] Li X., Magnuson C. W., Venugopal A., An J., Suk J. W., Han B., Borysiak M., Cai W., Velamakanni A., Zhu Y., Fu L., Vogel E. M., Voekl E., Colombo L., and Ruoff R. S. Graphene Films with Large Domain Size by a Two-Step Chemical Vapor Deposition Process. *Nano Letters*, 10 (11) (2010), 4328–4334.
- [249] Zhang J., Hu P., Wang X., and Wang Z. Structural evolution and growth mechanism of graphene domains on copper foil by ambient pressure chemical vapor deposition. *Chemical Physics Letters*, 536 (2012), 123–128.
- [250] Thangaraja A., Shinde S. M., Kalita G., Papon R., Sharma S., Vishwakarma R., Sharma K. P., and Tanemura M. Structure dependent hydrogen induced etching features of graphene crystals. *Applied Physics Letters*, 106 (25) (2015), 253106.
- [251] Zhang Y., Li Z., Kim P., Zhang L., and Zhou C. Anisotropic Hydrogen Etching of Chemical Vapor Deposited Graphene. *ACS Nano*, 6 (1) (2012), 126–132.

- [252] Van Gils S. V., Le Pen C., Hubin A., Terryn H., and Stijns E. Electropolishing of Copper in H₃PO₄, Ex Situ and In Situ Optical Characterization. *Journal of the Electrochemical Society*, 154 (3) (2007), C175–C180.
- [253] Shivareddy S., Bae S. E., and Brankovic S. R. Cu Surface Morphology Evolution during Electropolishing. *Electrochemical and Solid-State Letters*, 11 (1) (2008), D13–D17.
- [254] Awad A., Ghany N. A., and Dahy T. Removal of tarnishing and roughness of copper surface by electropolishing treatment. *Applied Surface Science*, 256 (13) (2010), 4370–4375.
- [255] Kim S. M., Hsu A., Lee Y.-H., Dresselhaus M., Palacios T., Kim K. K., and Kong J. The effect of copper pre-cleaning on graphene synthesis. *Nanotechnology*, 24 (36) (2013), 365602.
- [256] Chen S., Ji H., Chou H., Li Q., Li H., Suk J. W., Piner R., Liao L., Cai W., and Ruoff R. S. Millimeter-Size Single-Crystal Graphene by Suppressing Evaporative Loss of Cu During Low Pressure Chemical Vapor Deposition. *Advanced Materials*, 25 (2013), 2062–2065.
- [257] Reckinger N., Felten A., Santos C. N., Hackens B., and Colomer J.-F. The influence of residual oxidizing impurities on the synthesis of graphene by atmospheric pressure chemical vapor deposition. *Carbon*, 63 (2013), 84–91.
- [258] Lu C.-C., Lin Y.-C., Liu Z., Yeh C.-H., Suenaga K., and Chiu P.-W. Twisting Bilayer Graphene Superlattices. *ACS Nano*, 7 (3) (2013), 2587–2594.
- [259] Papon R., Pierlot C., Sharma S., Shinde S. M., Kalita G., and Tanemura M. Optimization of CVD parameters for graphene synthesis through design of experiments. *Physica Status Solidi B*, in press (2016).
- [260] Pancharkarla L. S., Subrahmanyam K. S., Saha S. K., Govindaraj A., Krishnamurthy H. R., Waghmare U. V., and Rao C. N. R. Synthesis, Structure, and Properties of Boron- and Nitrogen-Doped Graphene. *Advanced Materials*, 21 (2009), 4726–4730.
- [261] Iacopi F., Mishra N., Cunnig B. V., Goding D., Dimitrijević S., Brock R., Dauskardt Reinhold H. AND Wood B., and Boeckl J. Catalytic alloy approach for graphene on epitaxial SiC on silicon wafers. *Journal of Materials Research*, 30 (5) (2015), 609–616.
- [262] Papon R., Sharma K. P., Mahyavanshi R. D., Sharma S., Vishwakarma R., Rosmi M. S., Kawahara T., Cline J., Kalita G., and Tanemura M. CuNi binary alloy catalyst for growth of nitrogen-doped graphene by low pressure chemical vapor deposition. *Physica Status Solidi Rapid Research Letters*, 10 (10) (2016), 749–752.
- [263] Takesaki Y., Kawahara K., Hibino H., Okada S., Tsuji M., and Ago H. Highly Uniform Bilayer Graphene on Epitaxial Cu–Ni(111) Alloy. *Chemistry of Materials*, 28 (13) (2016), 4583–4592.
- [264] Liu H., Liu Y., and Zhou D. Chemical doping of graphene. *Journal of Materials Chemistry*, 21 (2011), 3335–3345.
- [265] Hassoun J., Bonaccorso F., Agostini M., Angelucci M., Betti M. G., Cingolani R., Gemmi M., Mariani C., Panero S., Pellegrini V., and Scrosati B. An Advanced Lithium-Ion Battery Based on a Graphene Anode and a Lithium Iron Phosphate Cathode. *Nano Letters*, 14 (8) (2014), 4901–4906.
- [266] Sboychakov A. O., Rakhmanov A. L., Rozhkov A. V., and Nori F. Electronic spectrum of twisted bilayer graphene. *Physical Review B*, 92 (7) (2015), 075402.
- [267] Lopes dos Santos J. M. B., Peres N. M. R., and Castro-Neto A. H. Graphene Bilayer with a Twist: Electronic Structure. *Physical Review Letters*, 99 (25) (2007), 256802.

- [268] Ni Z., Wang Y., Yu T., You Y., and Shen Z. Reduction of Fermi velocity in folded graphene observed by resonance Raman spectroscopy. *Physical Review B*, 77 (23) (2008), 235403.
- [269] Shallcross S., Sharma S., Kandelaki E., and Pankratov O. A. Electronic structure of turbostratic graphene. *Physical Review B*, 81 (16) (2010), 165105.
- [270] Brihuega I., Mallet P., González-Herrero H., Trambly de Laissardière G., Ugeda M. M., Magaud L., Gómez-Rodríguez J. M., Ynduráin F., and Veullen J.-Y. Unraveling the Intrinsic and Robust Nature of van Hove Singularities in Twisted Bilayer Graphene by Scanning Tunneling Microscopy and Theoretical Analysis. *Physical Review Letters*, 109 (19) (2012), 196802.
- [271] Yan W., Liu M., Dou R.-F., Meng L., Feng L., Chu Z.-D., Zhang Y., Liu Z., Nie J.-C., and He L. Angle-Dependent van Hove Singularities in a Slightly Twisted Graphene Bilayer. *Physical Review Letters*, 109 (12) (2012), 126801.
- [272] Havener R. W., Liang Y., Brown L., Yang L., and Park J. Van Hove Singularities and Excitonic Effects in the Optical Conductivity of Twisted Bilayer Graphene. *Nano Letters*, 14 (6) (2014), 3353–3357.
- [273] Jorio A., Kasperczyk M., Clark N., Neu E., Maletinsky P., Vijayaraghavan A., and Novotny L. Optical-Phonon Resonances with Saddle-Point Excitons in Twisted-Bilayer Graphene. *Nano Letters*, 14 (10) (2014), 5687–5692.
- [274] Patel H., Havener R. W., Brown L., Liang Y., Yang L., Park J., and Graham M. W. Tunable Optical Excitations in Twisted Bilayer Graphene Form Strongly Bound Excitons. *Nano Letters*, 15 (9) (2015), 5932–5937.
- [275] Tan Z., Yin J., Chen C., Wang H., Lin L., Sun L., Wu J., Sun X., Yang H., Chen Y., Peng H., and Liu Z. Building Large-Domain Twisted Bilayer Graphene with van Hove Singularity. *ACS Nano*, 10 (7) (2016), 6725–6730.
- [276] Nemes-Incze P., Magda G., Kamarás K., and Biró L. P. Crystallographically selective nanopatterning of graphene on SiO₂. *Nano Research*, 3 (2) (2010), 110–116.
- [277] Yang R., Zhang L., Wang Y., Shi Z., Shi D., Gao H., Wang E., and Zhang G. An Anisotropic Etching Effect in the Graphene Basal Plane. *Advanced Materials*, 22 (2010), 4014–4019.
- [278] Ci L., Xu Z., Wang L., Gao W., Ding F., Kelly K. F., Yakobson B. I., and Ajayan P. M. Controlled nanocutting of graphene. *Nano Research*, 1 (2) (2008), 116–122.
- [279] Datta S. S., Strachan D. R., Khamis S. M., and Johnson A. T. C. Crystallographic Etching of Few-Layer Graphene. *Nano Letters*, 8 (7) (2008), 1912–1915.
- [280] Ago H., Kayo Y., Solís-Fernández P., Yoshida K., and Tsuji M. Synthesis of high-density arrays of graphene nanoribbons by anisotropic metal-assisted etching. *Carbon*, 78 (2014), 339–346.
- [281] Luo D., Yang F., Wang X., Sun H., Gao D., Li R., Yang J., and Li Y. Anisotropic Etching of Graphite Flakes with Water Vapor to Produce Armchair-Edged Graphene. *Small*, 10 (14) (2014), 2809–2814.
- [282] Geng D., Wu B., Guo Y., Luo B., Xue Y., Chen J., Yu G., and Liu Y. Fractal Etching of Graphene. *Journal of the American Chemical Society*, 135 (17) (2013), 6431–6434.
- [283] Jung D. H., Kang C., Yoon D., Cheong H., and Lee J. S. Anisotropic behavior of hydrogen in the formation of pentagonal graphene domains. *Carbon*, 89 (2015), 242–248.

- [284] Liu L., Park J., Siegel D. A., McCarty K. F., Clark K. W., Deng W., Basile L., Idrobo J. C., Li A.-P., and Gu G. Heteroepitaxial growth of two-dimensional hexagonal boron nitride templated by graphene edges. *Science*, 343 (6167) (2014), 163–167.
- [285] Liu Z., Tizei L. H. G., Sato Y., Lin Y.-C., Yeh C.-H., Chiu P.-W., Terauchi M., Iijima S., and Suenaga K. Postsynthesis of h-BN/Graphene Heterostructures Inside a STEM. *Small*, 12 (2) (2016), 252–259.
- [286] Andriotis A. N. and Menon M. Transport properties of branched graphene nanoribbons. *Applied Physics Letters*, 92 (4) (2008), 042115.
- [287] Zhu L., Wang J., Zhang T., Ma L., Lim C. W., Ding F., and Zeng X. C. Mechanically Robust Tri-Wing Graphene Nanoribbons with Tunable Electronic and Magnetic Properties. *Nano Letters*, 10 (2) (2010), 494–498.
- [288] Ma L., Hu H., Zhu L., and Wang J. Boron and Nitrogen Doping Induced Half-Metallicity in Zigzag Triwing Graphene Nanoribbons. *Journal of Physical Chemistry*, 115 (14) (2011), 66195–6199.
- [289] Zhang G. and Zhang H. Thermal conduction and rectification in few-layer graphene Y Junctions. *Nanoscale*, 3 (2011), 4604–4607.
- [290] Lin Z. and Jun W. Valley selection rule in a Y-shaped zigzag graphene nanoribbon junction. *Chinese Physics B*, 23 (8) (2014), 087202.
- [291] Tsai W.-F., Huang C.-Y., Chang T.-R., Lin H., Jeng H.-T., and Bansil A. Gated silicene as a tunable source of nearly 100% spin-polarized electrons. *Nature Communications*, 4 (2012), 1500.
- [292] Liu J.-F. and Chan K. S. Y-Shaped Spin Filter in Graphene with Rashba Spin–Orbit Coupling. *Journal of the Physical Society of Japan*, 82 (2013), 074711.
- [293] Sutter P., Lahiri J., Albrecht P., and Sutter E. Chemical Vapor Deposition and Etching of High-Quality Monolayer Hexagonal Boron Nitride Films. *ACS Nano*, 5 (9) (2011), 7303–7309.
- [294] Gothard N., Daraio C., Gaillard J., Zidan R., Jin S., and Rao A. M. Controlled Growth of Y-Junction Nanotubes Using Ti-Doped Vapor Catalyst. *Nano Letters*, 4 (2) (2004), 213–217.

Appendix A

List of achievements

A.1 Publications in international journals

- **Remi Papon**, Christel Pierlot, Subash Sharma, Sachin Maruti Shinde, Golap Kalita and Masaki Tanemura. Optimization of CVD parameters for graphene synthesis through design of experiments. *Physica Status Solidi (b)*, in press.
- **Remi Papon**, Kamal Prasad Sharma, Rakesh D. Mahyavanshi, Subash Sharma, Riteshkumar Vishwakarma, Mohamad Saufi Rosmi, Toshio Kawahara, Joseph Cline and Masaki Tanemura. CuNi binary alloy catalyst for growth of nitrogen-doped graphene by low pressure chemical vapor deposition. *Physica Status Solidi Rapid Research Letters*, 10 (10) (2016), 749-752.
- Riteshkumar Vishwakarma, Sachin Maruti Shinde, Mohamad Saufi Rosmi, Chisato Takahashi, **Remi Papon**, Rakesh D. Mahyavanshi, Yosuke Ishii, Shinji Kawasaki, Golap Kalita and Masaki Tanemura. Influence of oxygen on nitrogen-doped carbon nanofiber growth directly on nichrome foil. *Nanotechnology*, 27 (36) (2016), 365602.
- Amutha Thangaraja, Sachin Maruti Shinde, Golap Kalita, **Remi Papon**, Subash Sharma, Riteshkumar Vishwakarma, Kamal Prasad Sharma and Masaki Tanemura. Structure dependent hydrogen induced etching features of graphene crystals. *Applied Physics Letters*, 106 (25) (2015), 253106.
- Sachin Maruti Shinde, Golap Kalita, Subash Sharma, Zurita Zulkifli, **Remi Papon** and Masaki Tanemura. Polymer-free graphene transfer on moldable cellulose acetate based paper by hot press technique. *Surface and Coatings Technology*, 275 (2015), 369-373.
- **Remi Papon**, Subash Sharma, Sachin Maruti Shinde, Amutha Thangaraja, Golap Kalita and Masaki Tanemura. Formation of graphene nanoribbons and Y-junctions by hydrogen induced anisotropic etching. *RSC Advances*, 5 (2015), 35297-35301.
- **Remi Papon**, Golap Kalita, Subash Sharma, Sachin Maruti Shinde, Riteshkumar Vishwakarma and Masaki Tanemura. Controlling single and few-layer graphene crystals growth in a solid carbon source base chemical vapor deposition. *Applied Physics Letters*, 105 (13) (2014), 133103.

- Golap Kalita, **Remi Papon**, Subash Sharma, Sachin Maruti Shinde, Riteshkumar Vishwakarma and Masaki Tanemura. Transformation of chemical vapor deposited individual graphene crystal with oxidation of copper substrate. *Carbon*, 80 (2014), 504-512.
- Muhammed Emre Ayhan, Golap Kalita, **Remi Papon**, Ryo Hirano and Masaki Tanemura. Synthesis of transfer-free graphene by solid phase reaction process in presence of a carbon diffusion barrier. *Materials Letters*, 129 (2014), 76-79.
- Subash Sharma, Golap Kalita, Ryo Hirano, Sachin Maruti Shinde, **Remi Papon**, Hajime Ohtani and Masaki Tanemura. Synthesis of graphene crystals from solid waste plastic by chemical vapor deposition. *Carbon*, 72 (2014), 66-73.
- Sachin Maruti Shinde, Golap Kalita, Subash Sharma, **Remi Papon**, Mohd Zamri Yusop and Masaki Tanemura. Synthesis of a three dimensional structure of vertically aligned carbon nanotubes and graphene from a single solid carbon source. *RSC Advances*, 4 (2014), 13355-13360.

A.2 Conference presentations

- **Remi Papon**, Golap Kalita and Masaki Tanemura. Synthèse et caractérisation du graphène. Journée Française de la Recherche (JFR), December 2nd, 2016, Tokyo.
- **Remi Papon**, Subash Sharma, Sachin Maruti Shinde, Amutha Thangaraja, Golap Kalita and Masaki Tanemura. Formation of particular graphene structures through H₂ induced anisotropic etching. 11th Annual IEEE International Conference on Nano/Micro Engineered and Molecular Systems (IEEE-NEMS), April 17th-20th, 2016, Matsushima Bay and Sendai MEMS City, Japan.
- **Remi Papon**, Christel Pierlot, Subash Sharma, Sachin Maruti Shinde, Golap Kalita and Masaki Tanemura. Optimization of CVD parameters for graphene synthesis through design of experiments. 63rd Japan Society of Applied Physics Spring Meeting, March 19th-22nd, 2016, Tokyo Institute of Technology, Ookayama Campus, Tokyo, Japan.
- **Remi Papon**, Subash Sharma, Sachin Maruti Shinde, Amutha Thangaraja, Golap Kalita and Masaki Tanemura. Formation of particular graphene structures through H₂ induced anisotropic etching. 28th International Microprocesses and Nanotechnology Conference, November 10th-13th, 2015, Toyama International Conference Center, Toyama, Japan.
- **Remi Papon**, Golap Kalita, Subash Sharma, Sachin Maruti Shinde and Masaki Tanemura. Synthesis of large graphene domains on copper foil using solid waste plastic as a carbon source. 6th IEEE International Nanoelectronics Conference, July 28th-31st, 2014, Hokkaido University, Sapporo, Japan .